Ore Geology Reviews 147 (2022) 104963

Contents lists available at ScienceDirect

Ore Geology Reviews

journal homepage: www.elsevier.com/locate/oregeorev

Vectors to ore in replacive volcanogenic massive sulphide deposits of the northern Iberian Pyrite Belt: Major and trace element mineral chemistry

Guillem Gisbert [a,*], Fernando Tornos [a], Emma Losantos [a], Sean McClenaghan [b], Juan Manuel Pons [c], Juan Carlos Videira [c], Maurice Brodbeck [b]

[a] Instituto de Geociencias (CSIC-UCM), Madrid 28040, Spain
[b] Raw Materials Characterization Laboratory, Trinity College Dublin, Dublin 2, Ireland
[c] MATSA, Almonaster la Real, Huelva 21342, Spain

ARTICLE INFO

Keywords:
Volcanogenic massive sulphide deposits
Ore vectors
Mineral chemistry
laser ablation ICP-MS
Iberian Pyrite Belt

ABSTRACT

As part of a broader characterization and study of vectors to ore in VMS systems of the Iberian Pyrite Belt (IPB, Spain), we have investigated in detail mineral chemistry vectors in a representative replacive deposit hosted in felsic volcanic rocks. At the Aguas Teñidas deposit (northern IPB) the hydrothermal system affected rocks of an originally homogeneous composition extending hundreds of metres beyond its footprint. The major and trace element chemistry of white micas, chlorite and carbonates have been analysed by electron microprobe (EMP) and laser ablation inductively coupled plasma mass spectrometry (LA-ICP-MS) to characterize geochemical vectors across the extent of the hydrothermal system at Aguas Teñidas.

White micas are dominated by muscovite in both regionally altered lithologies and within the hydrothermal system, with coexisting paragonite occurring in a halo beyond the first disseminated pyrite surrounding the stockwork and in the proximal hanging wall. Systematic variations have been observed in FeO/(FeO + MgO) and $Na_2O/(Na_2O + K_2O)$ across the alteration zone.

Chlorite is predominantly clinochlore in composition, with chamosite restricted to the centre of the hydrothermal system. In regionally altered lithologied it is characterized by a constantly low Al and Al^{IV} at variable Fe/(Fe + Mg); in rocks influenced by the hydrothermal system it presents higher Al^{IV} and total Al, and a progressive increase in Al, Al^{IV} and Fe/(Fe + Mg) towards its core.

Regional carbonates consist of calcite, with additional dolomite forming in proximal rocks. Iron content in dolomite increases towards the centre of the hydrothermal system, with ankeritic compositions becoming dominant.

Systematic variations in Ba, Cs, Li, Pb, Rb, Sn, Sr, Tl and Zn have been observed in white micas consistent with a proximal-distal transition (vector). Trends in chlorite have been less well characterized due to analytical limitations, although variations have been observed in the contents of As, Co, Li and Zn.

A schematic model has been proposed which accounts for the observed mineralogical and mineral chemistry trends across the hydrothermal footprint of the Aguas Teñidas VMS deposit. Major element signatures in white micas and chlorite are interpreted as having been controlled by the upwards and outwards flow of hot reducing Fe-rich hydrothermal fluids producing a coupled increase in temperature and fluid Fe/(Fe + Mg), and a decrease in fO_2, with increasing fluid/rock ratios towards the centre of the stockwork.

The data presented herein are not only applicable to VMS exploration in the IPB, but on a broader scale improve our general understanding of vectors to ore in VMS deposits in general.

1. Introduction

Vectors to ore play an increasingly important role in the exploration of mineral resources. In combination with the study of mineral systems and the development of new exploration technologies based on geophysical methods, they are crucial for new mineral discoveries contributing to the supply of raw materials. Ore deposits can occur as small and complex bodies difficult to trace; vectors to ore focus on the

* Corresponding author.
E-mail address: ggisbertp@hotmail.com (G. Gisbert).

https://doi.org/10.1016/j.oregeorev.2022.104963
Received 27 September 2021; Received in revised form 2 April 2022; Accepted 30 May 2022
Available online 1 June 2022

identification and study of their lithogeochemical and mineralogical fingerprints, which typically are much wider, extending well beyond the extent of ore mineralization. Vectors to ore are most commonly based on variations in lithology, geochemistry, mineralogy, and mineral chemistry associated to the hydrothermal system, which may be imparted during deposit formation or subsequently as a result of ore remobilization (e.g. Ballantyne, 1981; Madeisky and Stanley, 1993; Large et al., 2001a,b,c; Ames et al., 2016; Cooke et al., 2017; Mukherjee and Large, 2017; Soltani Dehnavi et al., 2018a).

Mineral chemistry can be a powerful tool for vectors to ore, although for its effective use several aspects must be considered, such as the presence of mineral phases unrelated to ore-forming processing both in regional protoliths and hydrothermally-modified rocks, or the effects of later re-equilibration and recrystallization (Supplementary Material 1.1). The study of major elements in minerals (e.g. Fe-Mg content in chlorite, Large et al., 2001b; K-Na-Fe-Mg in white mica, Gaillard et al., 2018; Uribe-Mogollon and Maher, 2018) was the earliest and still most widespread use of mineral chemistry as a vector to ore. It can be based on direct analysis of mineral chemistry (e.g. Electron Microprobe Analysis, Large et al. 2001b), or on other techniques such as X-Ray Diffraction (XRD; e.g. Toscano et al., 1994a) or spectral methods (e.g. Short Wave Infrared Spectral Analysis, SWIR; Herrmann et al., 2001, Wang et al., 2017) aimed at detecting the mineral structure and variations associated to changes in major element contents. Additionally, advances in the analysis of trace elements by Laser Ablation Inductively Coupled Plasma Mass Spectrometry (LA-ICP-MS) have increased the use of this technique in a wide variety of mineral studies (e.g. chlorite, white micas, epidote, pyrite, rutile) across different deposit types, including sedimentary exhalative (SEDEX) deposits (Mukherjee and Large, 2017), orogenic gold (Gaillard et al., 2018), VMS (Soltani Dehnavi et al., 2018a), and particularly in porphyry systems (e.g. epidote, Cooke et al., 2014; Cooke et al., 2015; Cooke et al., 2020; Baker et al., 2020; Wilkinson et al., 2020; chlorite, Xiao et al., 2018; Cooke et al., 2020; Maydagán et al., 2018; white micas, Maydagán et al., 2018; Alva-Jimenez et al., 2020; pyrite, Cook et al., 2020). Nevertheless, the use of trace element mineral signatures as vectors to ore in VMS systems is still incipient and, thus, further work is needed.

Volcanogenic Massive Sulphide deposits represent a major source of base (Cu, Pb, Zn), precious (Ag, Au) and other metals (e.g. Co, Sn, In, Cd, Tl, Ga, Se, Sb, Bi) of economic and industrial importance (Large et al., 2001a; Franklin et al., 2005; Tornos et al., 2015). The Iberian Pyrite Belt (IPB), located in the SW Iberian Peninsula (Fig. 1), is arguably the largest known accumulation of VMS in the earth's crust, and represents an important mining region of Spain and a key base metal producer for Europe (Tornos, 2006). Vectors to ore have been studied in this district (e.g. Relvas et al., 1990; Relvas et al., 2006; Madeisky and Stanley, 1993; Toscano et al., 1994a, b; Costa, 1996; Luz et al., 2019; Velasco-Acebes et al., 2019), but their characterization is still far from systematic or complete, especially compared to other VMS districts (e.g. Australian districts, Large et al., 2001a and references therein; Bathurst Mining Camp, Canada, Soltani Dehnavi et al., 2018a; Soltani Dehnavi et al., 2018b; Soltani Dehnavi et al., 2019). Moreover, trace element mineral

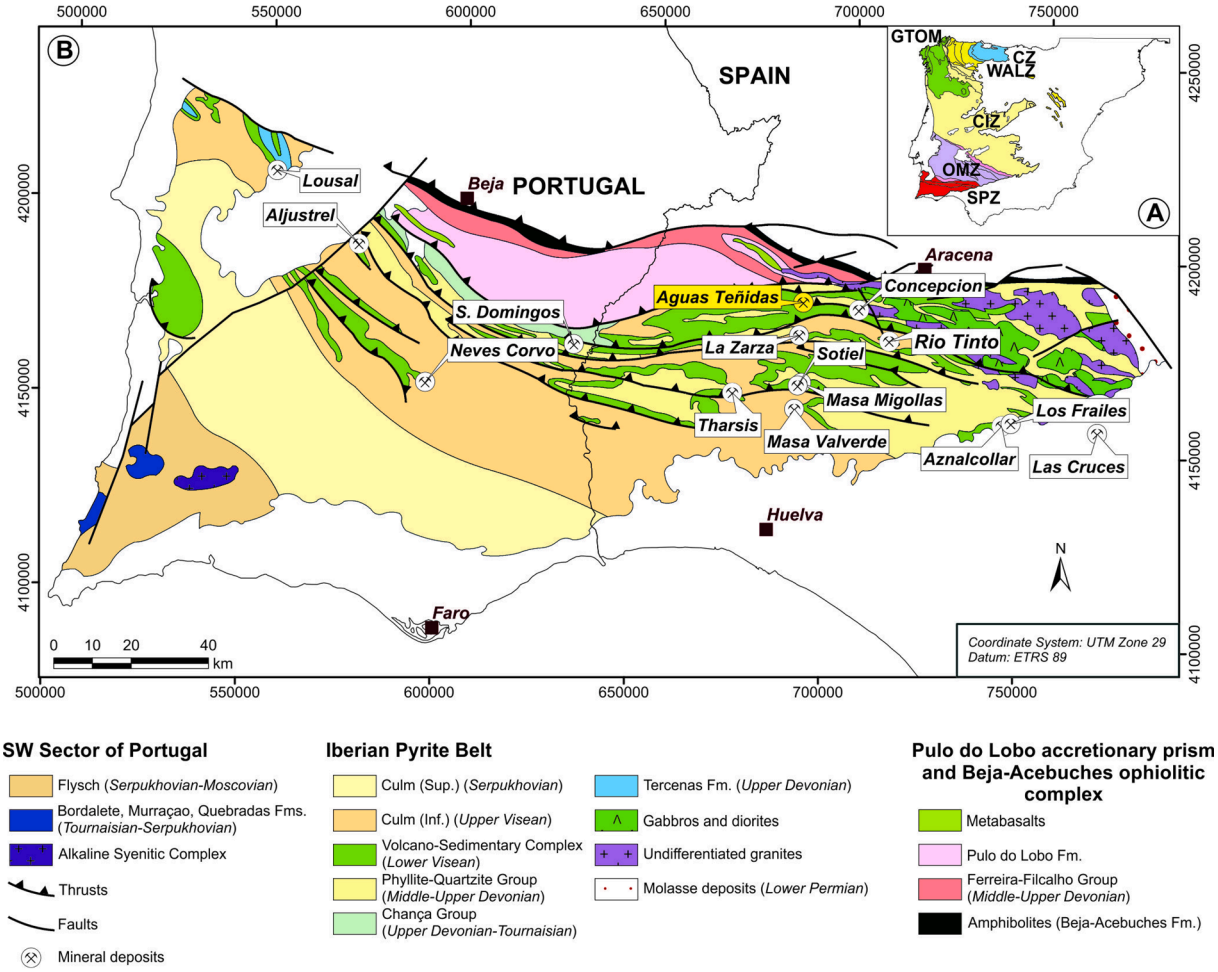

Fig. 1. Geological map of the South Portuguese Zone and location of the Aguas Teñidas deposit. CZ: Cantabrian Zone; WALZ: West Asturian-Leonese Zone; GTOM: Galicia-Trás-os-Montes Zone: CIZ: Central Iberian Zone; OMZ: Ossa-Morena Zone; SPZ: South Portuguese Zone. Adapted from Martin-Izard et al. (2016), based on IGME (1982), Leistel et al. (1998), Simancas (2004), and Mantero et al. (2011).

chemistry has not yet been investigated for its use as pathfinder in the IPB.

This work forms part of a broader study aimed at the investigation and characterization in the IPB of the main vectors to ore currently used in VMS systems (Fig. 1 in Gisbert et al., 2021) in order to improve mineral exploration and the location of new resources in the area. Since previous works have mostly focused on the study of the larger exhalative shale-hosted deposits of the southern IPB (e.g. Toscano et al., 1994a; Toscano et al., 1994b; Tornos et al., 2008; Sáez et al., 2011; Velasco-Acebes et al., 2019) or the giant Rio Tinto deposit (e.g. Madesiky and Stanley, 1993; Costa, 1996), our focus has been on the less studied volcanic rock hosted replacive deposits of the northern IPB (e.g. Relvas et al., 1990; Sánchez-España et al., 2000). Although generally smaller in size compared to southern deposits, those in the northern IPB typically exhibit higher base metal concentrations (Tornos, 2006). Replacive deposits form through sub-seafloor replacement of lithologies favourable to hydrothermal infiltration situated beneath the seafloor (Doyle and Allen, 2003; Tornos et al., 2015); thus, they are expected to produce large anomalies associated to hydrothermal alteration in the hanging wall area, which has major implications for exploration.

We have performed a thorough study of a representative replacive VMS mineralization, the Aguas Teñidas deposit. The massive sulphides and stockwork of this deposit are hosted in a felsic dome complex which extends hundreds of metres beyond the hydrothermal system, and which upon emplacement had a homogeneous chemical composition (Conde and Tornos, 2020; Gisbert et al., 2021); this has allowed a detailed characterization and study of mineralogical and chemical changes produced on the host rocks by the hydrothermal system during the mineralizing event, without the complexities associated to changing lithologies. In Gisbert et al. (2021) vectors to ore related to mineralogical zoning and whole rock geochemistry were described. Here, we present the results related to the characterization of vectors to ore associated to mineral chemistry of both major and trace elements, mainly in white micas and chlorite, analysed by electron microprobe and LA-ICP-MS.

White micas are common and ubiquitous mineral phases related to hydrothermal alteration in VMS systems (Large et al., 2001a; Franklin et al., 2005; Soltani Dehnavi et al., 2018a). Moreover, several substitutions can occur in their crystal lattice in response to varying conditions (e.g. Fe-Mg-Si-Al, Na-K-Ba, Rieder et al., 1998); this can include useful vectoring trace elements (e.g. volatiles such as Tl, Sb, Hg) which are accommodated within their structure and interlayer positions (Soltani Dehnavi et al., 2018a and references therein). Consequently, they are commonly regarded as some of the most useful vectoring phases. Chlorite is most common in the inner part of alteration zones (Large et al., 2001a, Franklin et al., 2005). Similar to white micas, several substitutions can occur in its crystal structure (e.g. Fe-Mg-Si-Al, Wiewióra and Weiss, 1990), and useful vectoring trace elements (e.g. volatiles such as Tl, Sb, Hg) can also be accommodated in it (Soltani Dehnavi et al., 2019).

Data presented in this work will not only be applicable to exploration in the IPB but, on a broader scale, will also contribute to improve our general understanding of vectors to ore in replacive-type VMS deposits in particular and VMS deposits in general.

2. Geological setting

2.1. VMS deposits in the Iberian pyrite Belt

The IPB is located in the southernmost domain of the Variscan Belt in the Iberian Peninsula, the South Portuguese Zone (Fig. 1). VMS deposits formed from Late Famennian to early Late Visean times (ca. 360–335 Ma) within intra-continental third order basins, related to a period of transtensional tectonics triggered by oblique collision during the ongoing accretion of the Variscan belt (Oliveira, 1990, Silva et al., 1990). They are hosted in a stratigraphic sequence dominated by mudstones and interbedded bimodal volcanic, and shallow intrusive rocks (Volcanic Sedimentary Complex, VSC; Schermerhorn, 1971). Subsequent compressive tectonism disrupted the stratigraphic record forming a thin-skinned foreland fold and thrust belt (Silva et al., 1990), and produced prehnite-pumpellyite to low greenschist facies regional metamorphism (Munhá, 1983). A detailed review on the geology and metalogenesis of the IPB can be found in Barriga (1990), Leistel et al. (1998), Carvalho et al. (1999) and Tornos (2006), and is briefly summarized in Supplementary Material 1.2, and in Supplementary Material 1.1 in Gisbert et al. (2021).

The IPB hosts over 90 VMS deposits (including 22% of the VMS world-class deposits; >32 Mt, Laznicka, 1999) featuring in excess of 1600 Mt of massive sulphides originally in place, and about 250 Mt of stockwork ore (Tornos, 2006). Although individual lenses can be up to 170 Mt (La Zarza), most giant deposits (e.g. Neves Corvo, Tharsis, Río Tinto) typically include numerous separate ore bodies (Tornos, 2006).

2.2. The Aguas Teñidas deposit

2.2.1. Host stratigraphic sequence

The Aguas Teñidas deposit is situated in the northern part of the IPB (Fig. 1). VSC rocks dominate the area around the deposit, consisting of volcanic and subvolcanic rocks with minor shale (Bobrowicz, 1995; McKee, 2003; Conde Rivas, 2016; Conde and Tornos, 2020) (Fig. 2). The massive sulphides formed by replacement of the permeable and reactive uppermost autobrecciated and partially devitrified facies of a dacitic dome (Bobrowicz, 1995; Tornos, 2006) belonging to the Footwall Felsic Unit (Conde Rivas, 2016; Conde and Tornos, 2020). This dome constitutes the footwall of the deposit and extends beyond the footprint of the

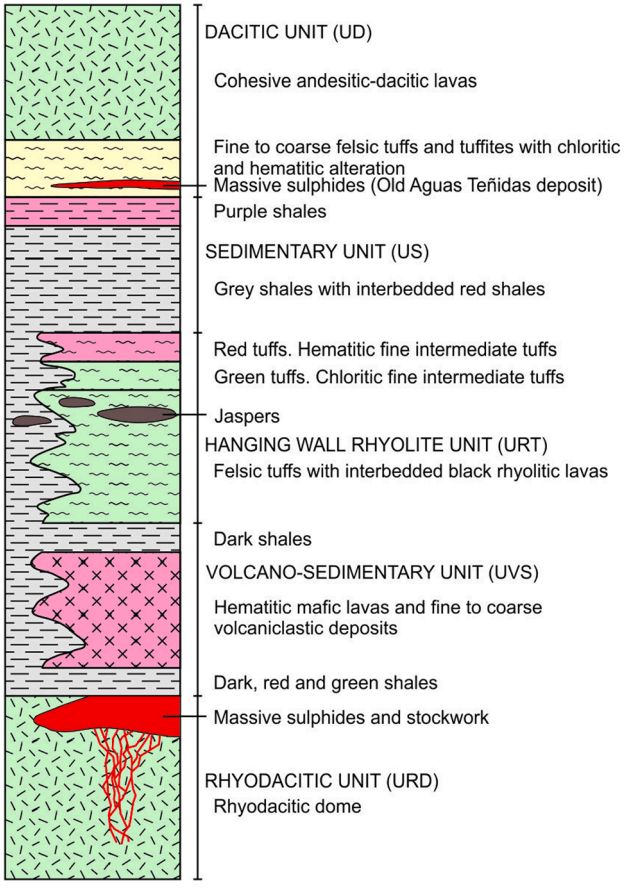

Fig. 2. Local stratigraphy at the Aguas Teñidas deposit, not to scale. Nomenclature follows original description by Mina de Aguas Teñidas S.A. (MATSA). Modified from MATSA.

hydrothermal system (Gisbert et al., 2021). It was referred to as the URD (Unidad Riodacítica; Rhyodacite Unit) in the mining terminology (Mina de Aguas Teñidas S.A., MATSA); to differentiate this specific dome from other volcanic rocks in the broader Footwall Felsic Unit, the mining term will be used in this work. The hanging wall to the host dome and orebody presents strong vertical and lateral lithological and facies changes; it is dominated by red basaltic (s.l.) lavas (predominant in the northern part of the deposit), green to red volcaniclastic rocks, and red and green metapelites (present in the southern part of the deposit) (Hidalgo et al., 2000). Host rocks have endured three consecutive stages

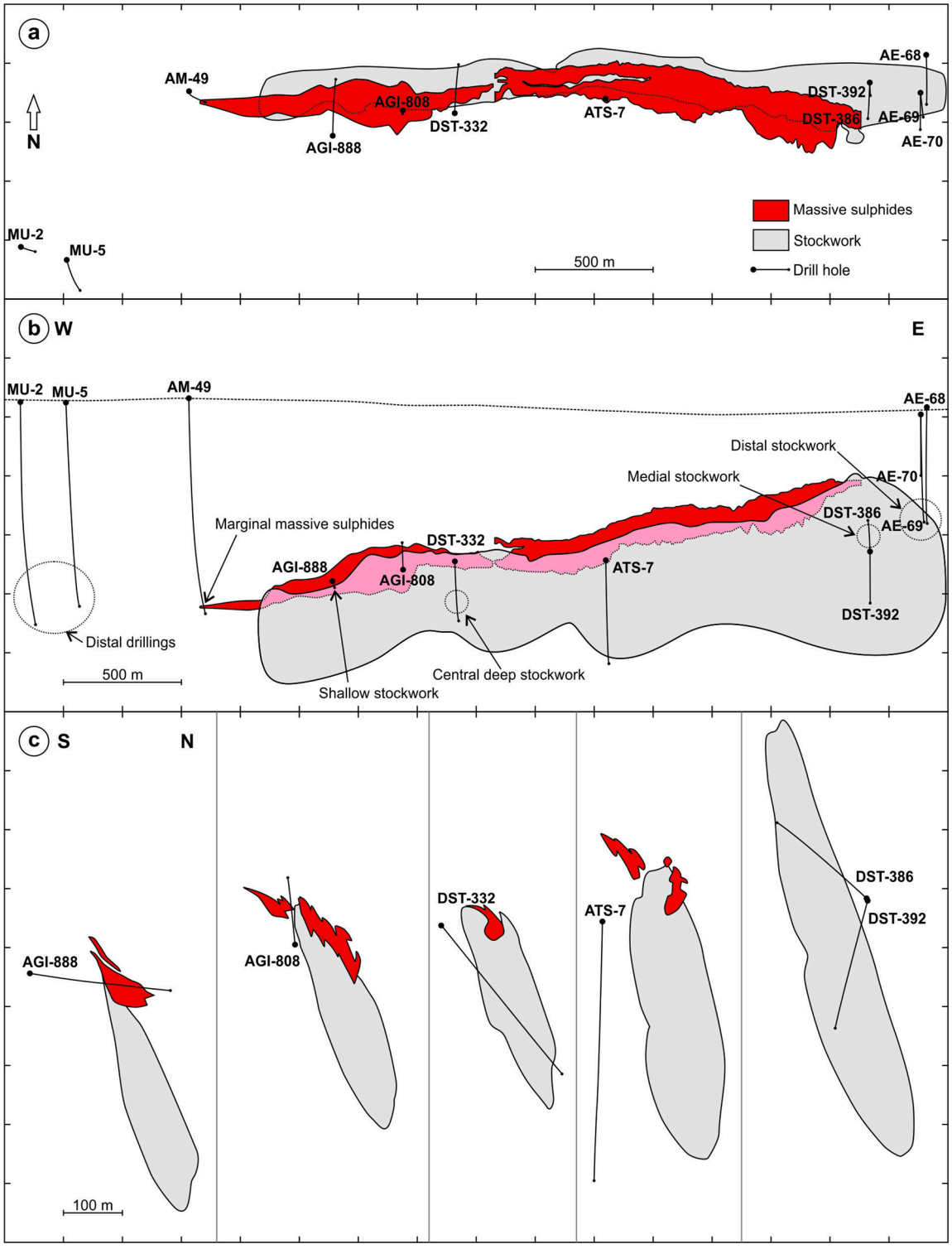

Fig. 3. Plan view (a), front view (b) and cross sections perpendicular to the deposit elongation (c) of the Aguas Teñidas deposit (massive sulphides and stockwork), and location of the studied drill holes. Front view (b) is facing N, with no vertical exaggeration; the dotted line represents the ground level. Cross sections (c) are facing W with no vertical exageration. Cores MU-2, MU-5, AM-49, AE-68, AE-69 and AE-70 were drilled from surface; the rest were performed from an underground gallery; AGI-888 was drilled horizontally and AGI-808 and DST-386 upwards, in the three cases advancing stratigraphically upwards. Modified from Gisbert et al. (2021). Data provided by MATSA.

of alteration/modification: 1) initial seafloor metasomatism produced by interaction of volcanic rocks with seawater during and soon after emplacement in submarine conditions (Munhá and Kerrich, 1980); 2) hydrothermal alteration related to the mineralizing event; and, 3) metamorphism under prehnite-pumpellyite facies conditions (Bobrowicz, 1995; Sánchez-España et al., 2000; McKee, 2003; Gisbert et al., 2021).

2.2.2. Deposit characteristics

Aguas Teñidas is a polymetallic (Cu-Zn-Pb) massive sulphide deposit. It consists of a single roughly E-W-oriented elongated massive sulphide body ca. 1,800 m long and 150 to 300 m wide located at a depth between 280 (eastern side) and 650 m (western side) (Fig. 3). It is wedge-shaped perpendicular to elongation, with a maximum thickness of 90–100 m by its northern margin, which is mostly fault-bounded (Hidalgo et al., 2000; McKee, 2003). This fault (Northern Fault, Fig. 4) has been interpreted as a *syn*-sedimentary growth fault which acted as the main feeder structure for the hydrothermal system (Bobrowicz, 1995; McKee, 2003), and which was inverted during the Variscan compressive deformation (McKee, 2003). A funnel-shaped stockwork zone occurs below the massive sulphide body along most of its extent (Bobrowicz, 1995; Hidalgo et al., 2000; McKee, 2003) (Figs. 3 and 4). Variscan compressional deformation produced abundant thrusts and shear zones which occur along several contacts with the host rock as well as transecting the massive sulphides (McKee, 2003) (Fig. 4). The contact between the massive sulphide body and the hanging wall sequence is a shear zone of unknown, but presumably small displacement (Gisbert et al., 2021). In contrast, there is structural continuity between the massive sulphides and the underlying stockwork in most areas (Bobrowicz, 1995; Hidalgo et al., 2000; McKee, 2003).

At the deposit scale, massive sulphides exhibit zonation with a Cu-rich core at the base and Zn-Pb-rich ore towards the top and periphery (Fig. 4), with minor Pb, Zn and Au ore at the footwall contact which represents a deviation from the classical VMS model (Bobrowicz, 1995; McKee, 2003). Four main phases account for over 95 vol% of the sulphide mineralogy; in order of decreasing abundance: pyrite (generally between 50 and 80 vol%), sphalerite, chalcopyrite and galena. In addition, tetrahedrite-tennantite group minerals, arsenopyrite, stannite, bournonite and native bismuth are also present, as well as trace amounts of fine-grained magnetite (Hidalgo et al., 2000). At the meter to decimetre-scale, massive sulphides are highly complex, with numerous repetitions, displacements and lateral variations (McKee, 2003).

Pervasive hydrothermal alteration envelopes the orebody and stockwork system (Fig. 4). Footwall alteration passes laterally, from core to edge, from quartz (only locally present), to chlorite-quartz, sericite-chlorite-quartz, and sericite-quartz zones, and finally transitions into regional sea-floor metasomatic assemblages at the margins of the system (Bobrowicz, 1995; Hidalgo et al., 2000; McKee et al., 2001; Gisbert et al., 2021). In the upper areas of the chlorite alteration zone, particularly along its northern and southern contacts with the siliceous zone, chlorite-carbonate alteration zones are found (Bobrowicz, 1995). Hanging wall alteration consists of a proximal sericite alteration zone followed by albite-dominant alteration in more distal positions (Gisbert et al., 2021). In addition, the hanging wall exhibits a younger overprinting oxidizing alteration represented by iron oxides (Tornos, 2006, Gisbert et al., 2021).

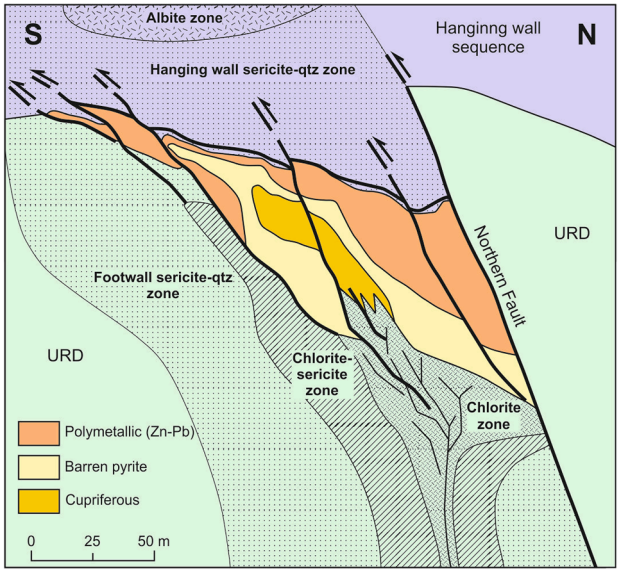

Fig. 4. Schematic cross section of the Aguas Teñidas deposit based on Sánchez-España et al. (2003). It includes shear zones described by McKee (2003), as well as hanging wall alteration zones described in Gisbert et al. (2021).

3. Methods

3.1. Sampling

Samples from proximal, medial and distal host rocks, and from shallow, medial, and deep regions of the stockwork, were collected from 12 representative drill cores provided by MATSA; this allowed for the characterization of the lithological background as well as variations (Proximal-Distal) across the hydrothermal system. Drill hole locations and their spatial relationship to the mineralization are shown in Fig. 3. A summary of drill core characteristics and the purpose of their sampling are provided in Supplementary Material 1.3. Schematic stratigraphic columns of the main studied portions are presented in Fig. 5. A list of the samples and a brief description of their location within the system and characteristics is provided in Supplementary Material 2. Sample name consists of the drill core name and the depth along the core where it was collected, in meters (e.g. sample DST-332/75.8 was collected at 75.8 m from the start of drill core DST-332).

3.2. Analytical methods

Thin sections for 112 samples were prepared for petrographic study and in situ mineral analysis for major and trace elements by EMPA and LA-ICP-MS, respectively. Samples were examined using a petrographic microscope at the IGEO followed by Scanning Electron Microscopy (SEM) at the Centro Nacional de Microscopía Electrónica (CNME) of the Universidad Complutense de Madrid.

Major element analysis of minerals was carried out by electron microprobe (EMP) at the facilities of the CNME and the Centres Científics i Tecnològics of the Universitat de Barcelona (CCiT-UB). At the CNME, a JEOL SUPERPROBE JXA-8900 M was used; analyses were conducted at 15 kV and 20nA using a 5 μm spot. Mineral reference samples were used for calibration (Si, Na: albite; Al: sillimanite; Fe, Mn: almandine; K: microcline; Mg, Ca, Ti: kaersutite; P, F, Cl: apatite). At the CCiT-UB, a JEOL JXA-8230 was used. Silicates were measured at 15 kV and 10nA with a 5 μm spot using mineral reference samples for calibration (Si: diopside; Al: kyanite; Ti: rutile; Fe: Fe2O3; Mg: periclase; Mn: rhodonite; Ca: wollastonite; Na: albite; K: orthoclase; Ba: barite; F: fluorite). Carbonates were measured at 15 kV and 6nA with a 10 μm spot, using mainly carbonate mineral reference samples for calibration (Ca: calcite; Mg: dolomite; Fe: siderite; Mn: rhodonite; Sr: strontianite; Ba: barite; Si: diopside; Na: albite).

Trace element analysis of minerals was carried out using LA-ICP-MS at the iCRAG Raw Material Characterization Laboratory of Trinity College in Dublin. A Teledyne PhotonMachines G2 193 nm Excimer ArF laser with a HelEx II 2- vol cell coupled to a Thermo Elemental iCapQs ICP-MS was used. Silicates (white micas and chlorite) were analysed for ^{7}Li, ^{23}Na, ^{24}Mg, ^{27}Al, ^{29}Si, ^{34}S, ^{35}Cl, ^{39}K, ^{44}Ca, ^{49}Ti, ^{51}V, ^{53}Cr, ^{55}Mn, ^{57}Fe, ^{59}Co, ^{60}Ni, ^{63}Cu, ^{66}Zn, ^{75}As, ^{77}Se, ^{81}Br, ^{85}Rb, ^{88}Sr, ^{111}Cd, ^{115}In, ^{118}Sn,

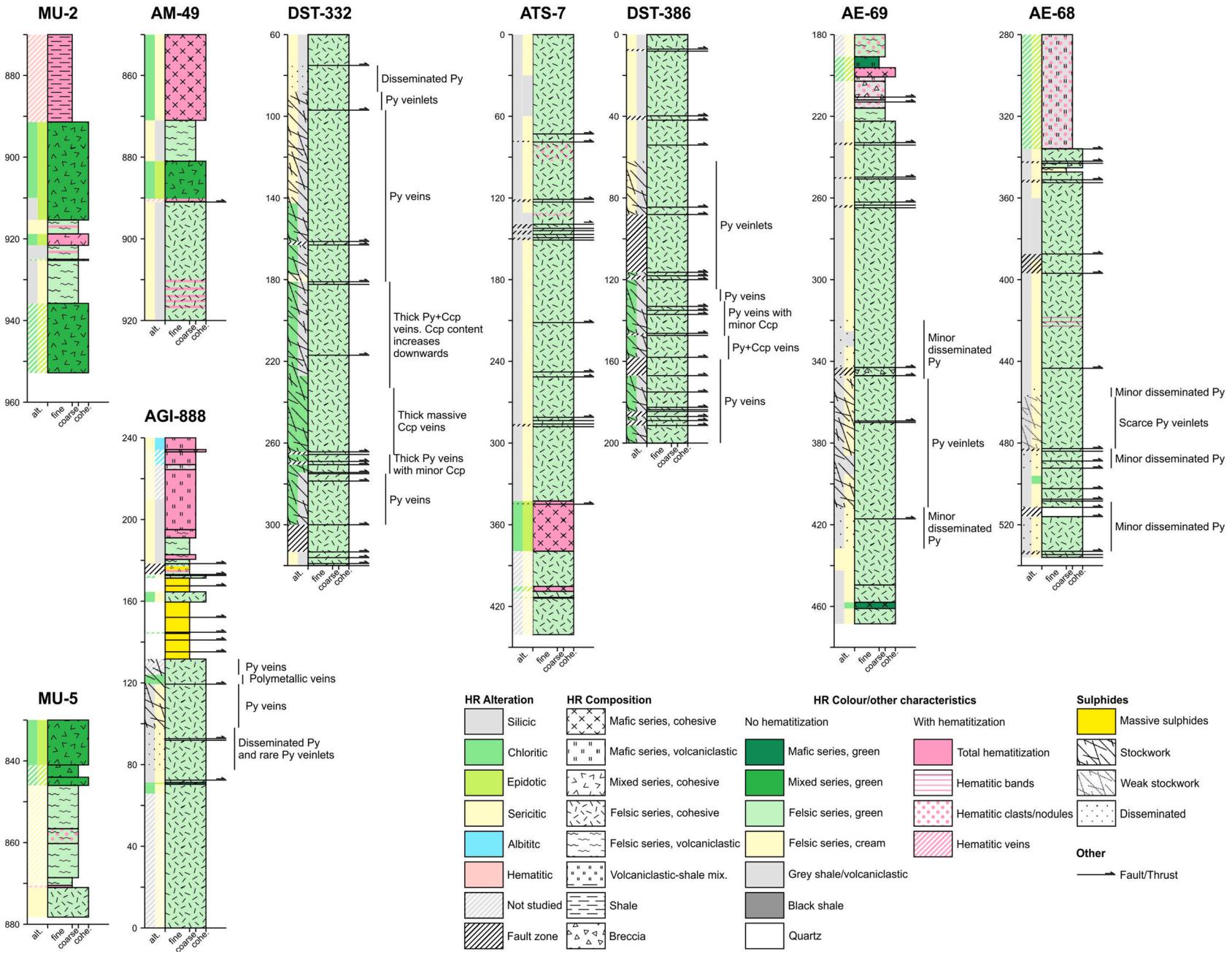

Fig. 5. Schematic columns of the main studied drill cores. Depth along cores in meters. HR: host rock.

^{123}Sb, ^{125}Te, ^{133}Cs, ^{137}Ba, ^{202}Hg, ^{205}Tl, ^{208}Pb, ^{209}Bi. Isotopes were selected to avoid significant isobaric-mass and polyatomic-molecular interferences. For the analyses, a spot size of 35 μm (square) was used, with a repetition rate of 6 Hz and fluences ranging from 1.35 to 1.44 J/cm^2. Data were calibrated using NIST610 and NIST612 glass standards and BCR-2G basalt glass standard. Sulphide phases (pyrite, chalcopyrite) were analysed for ^{55}Mn, ^{59}Co, ^{60}Ni, ^{65}Cu, ^{67}Zn, ^{71}Ga, ^{73}Ge, ^{75}As, ^{77}Se, ^{95}Mo, ^{109}Ag, ^{111}Cd, ^{115}In, ^{118}Sn, ^{121}Sb, ^{125}Te, ^{197}Au, ^{202}Hg, ^{207}Pb, ^{209}Bi. A spot size of 20 μm (square) was used, with a repetition rate of 6 Hz and fluences of 1.25 J/cm^2 for chalcopyrite and 1.34 J/cm^2 for pyrite. Data were calibrated using MUL-ZnS (Onuk et al., 2017) and MASS-1 (Wilson et al., 2002) sulphide standards. Limits of detection were <10 ppm for trace elements and <0.1 wt% for major elements. Precision of results were within 10 % error and accurate to within 5 %. Data reduction was performed in Iolite using Fe as an internal standard for pyrite and chalcopyrite, and Si for silicate minerals. Concentration data were obtained by applying the data reduction scheme 'Trace-Elements' (Woodhead et al., 2007) in 'Internal Element Standard' mode. Fully quantitative concentrations were calculated applying the internal standardization method of Ulrich et al. (2009), Ulrich et al. (2011).

The typically fine-grained nature of the mineral assemblage around VMS deposits such as Aguas Teñidas, combined with the common close association of several mineral phases (e.g. muscovite, chlorite, quartz, pyrite, etc.) makes the identification of appropriately sized targets for EMP and especially LA-ICP-MS analyses problematic (e.g. Soltani Dehnavi et al., 2018a; Soltani Dehnavi et al., 2018b; Soltani Dehnavi et al., 2019). Thus, compositional values reported in this study may be influenced by micro-inclusions or partial analysis of encroaching mineral phases. Criteria to filter out mixed analyses are described in Supplementary Material 1.4; the selection of normalization values for LA-ICP-MS analyses is also described.

4. Results

The mineral assemblages, textures, and chemistry here described are the result of original rock composition, seafloor metasomatism, mineralization-related hydrothermal alteration, and subsequent modification by diagenesis and metamorphism in the prehnite-pumpellyite facies. Based on 1) a clear relationship of mineralogy and mineral chemistry with location relative the hydrothermal system, and 2) no evidence of major recrystallization during post-mineralization metamorphism (Gisbert et al., 2021), we suggest that the distribution and composition of the currently observed white micas and chlorite are predominantly controlled by seafloor metasomatism and hydrothermal alteration through their precursory alteration phases. Accordingly, and to simplify the description of results in this section, the current mineral assemblage will be used to describe the characteristics of hydrothermal alteration in this deposit. Nevertheless, the nature and influence of primary alteration minerals will be addressed in the discussion section.

4.1. Petrography and mineral distribution

Quartz, white micas and chlorite dominate the alteration mineral assemblage of rocks around the Aguas Teñidas deposit. In addition, other phases such as epidote, carbonates and Fe and Ti oxides occur depending on original rock composition and location relative to the hydrothermal system. Schematic sections of the studied cores are provided in Fig. 5, in which lithology, dominant alteration assemblage and mineralization types are shown. A detailed description of textures and mineral assemblages in the different parts of the studied system is provided in Supplementary Material 1.5.

In distal locations (e.g. cores MU-2, MU-5), seafloor metasomatism of volcanic and subvolcanic rocks resulted in the albitization of feldspar and the variable alteration of groundmass to white mica, quartz and chlorite. The alteration assemblage also includes epidote and carbonates in mafic rocks. Accessory phases include Fe and Fe-Ti oxides, zircon and apatite.

In URD footwall rocks, the intensity of alteration increases towards the ore, with sericite-quartz alteration dominating the external parts of the stockwork system and areas around it. Feldspar phenocrysts may be partially to entirely replaced by white mica aggregates coarser than the groundmass; in this zone chlorite is usually a minor component. Close to the disseminated pyrite zone that surrounds the feeder system (Fig. 5), Fe and Fe-Ti oxides disappear and only rutile is observed in more internal locations. In rocks exhibiting a higher degree of alteration, the original rock texture is completely obliterated except for the modified remnants of quartz phenocrysts. Sericite-quartz alteration transitions to chlorite-quartz alteration towards the centre of the system. Increasing chlorite abundances occur at different locations relative to the appearance of sulphides depending on the area (marginal vs. central, deep vs. shallow, Fig. 5). The most intense chloritization is usually found in rocks hosting mineralized veins with chalcopyrite in the sulphide assemblage (e.g. central parts of the stockwork system in DST-332 and DST-386). In the most heavily chloritized rocks white mica is not typically present, only occasionally occurring as rare individual grains.

The hanging wall proximal alteration was investigated in drill core AGI-888, where mafic to felsic volcaniclastic rocks dominate. Regardless of original composition, these show a proximal sericite alteration zone (fine-grained assemblage of white micas, quartz and minor to rare chlorite) followed by albite alteration (fine-grained assemblage of albite, muscovite and minor amounts of chlorite). In addition, hanging wall rocks predominantly show an overprinted (Tornos, 2006) oxidizing alteration in which widespread pervasive very fine-grained Fe oxides occur.

4.2. White micas

4.2.1. Major elements

White micas mostly consist of solid solutions between four main end-members: muscovite ($KAl_2(AlSi_3O_{10})(OH)_2$), alumino-celadonite ($K(Mg,Fe^{2+})Al(Si_4O_{10})(OH)_2$), celadonite ($K(Mg,Fe^{2+})Fe^{3+}(Si_4O_{10})(OH)_2$) and paragonite ($NaAl_2(AlSi_3O_{10})(OH)_2$) (Rieder et al., 1998). Solid solutions between muscovite and celadonite (*s.l.*) are commonly known as phengite, and are the dominant phase in VMS systems alteration halos. The celadonitic content in phengite is known as phengicity. Typical major element chemical vectors include variations related to the Tschermak substitution ($(Fe^{2+}, Mg)^{VI} + Si^{IV} \leftrightarrow Al^{IV} + Al^{VI}$; phengicity), and substitutions between K, Na and Ba. (e.g. Large et al., 2001a). Results of white micas characterization by EMP analysis performed in this study are provided in Supplementary Material 2.

White micas within individual samples tend to present relatively homogeneous compositions regardless of textural variations (e.g. fine-grained groundmass white mica vs. coarser crystals in feldspar pseudomorphs; white micas in the host rock vs. white micas in mineralized veins). They have been classified following Rieder et al. (1998) based on EMP data (Fig. 6a and b). Since EMP does not differentiate between Fe^{2+} and Fe^{3+}, molar Fe^{3+} has been roughly estimated as Fe + Mg + Mn + (Al^{IV}-1) – (Ti + Na + K + 2Ca + 2Ba), and constrained to be ≥ 0 and $\leq$ Fe. White micas classify as muscovite/paragonite (Fig. 6a), with a muscovite/paragonite component mostly in the range of molar (Mg + Fe^{2+})/(Mg + Fe + Al^{VI}) 0.2–0.02. Since the Fe + Mg contents are below 0.5 a.p.f.u. in all cases, projection of white micas within the muscovite/paragonite field would occur even if Fe was considered to occur exclusively as Fe^{2+} or Fe^{3+}. Sodium contents indicate that muscovite is the dominant white mica, and that it coexists with paragonite in some samples from the most proximal hanging wall (AGI-888/179.8, AGI-888/180.9, AGI-888/191.5) and the area surrounding the stockwork in the footwall (e.g. AE-68/367.6, AE-68/420.0, AE-69/217.0, AE-69/273.2, AGI-888/74.3) (Fig. 6b). This coexistence does not occur as two separate mica populations but as crystals with interleaved muscovite and paragonite laminae (Supplementary Material 1.6); the fine character of this interleaved structure results in analytical mixtures upon

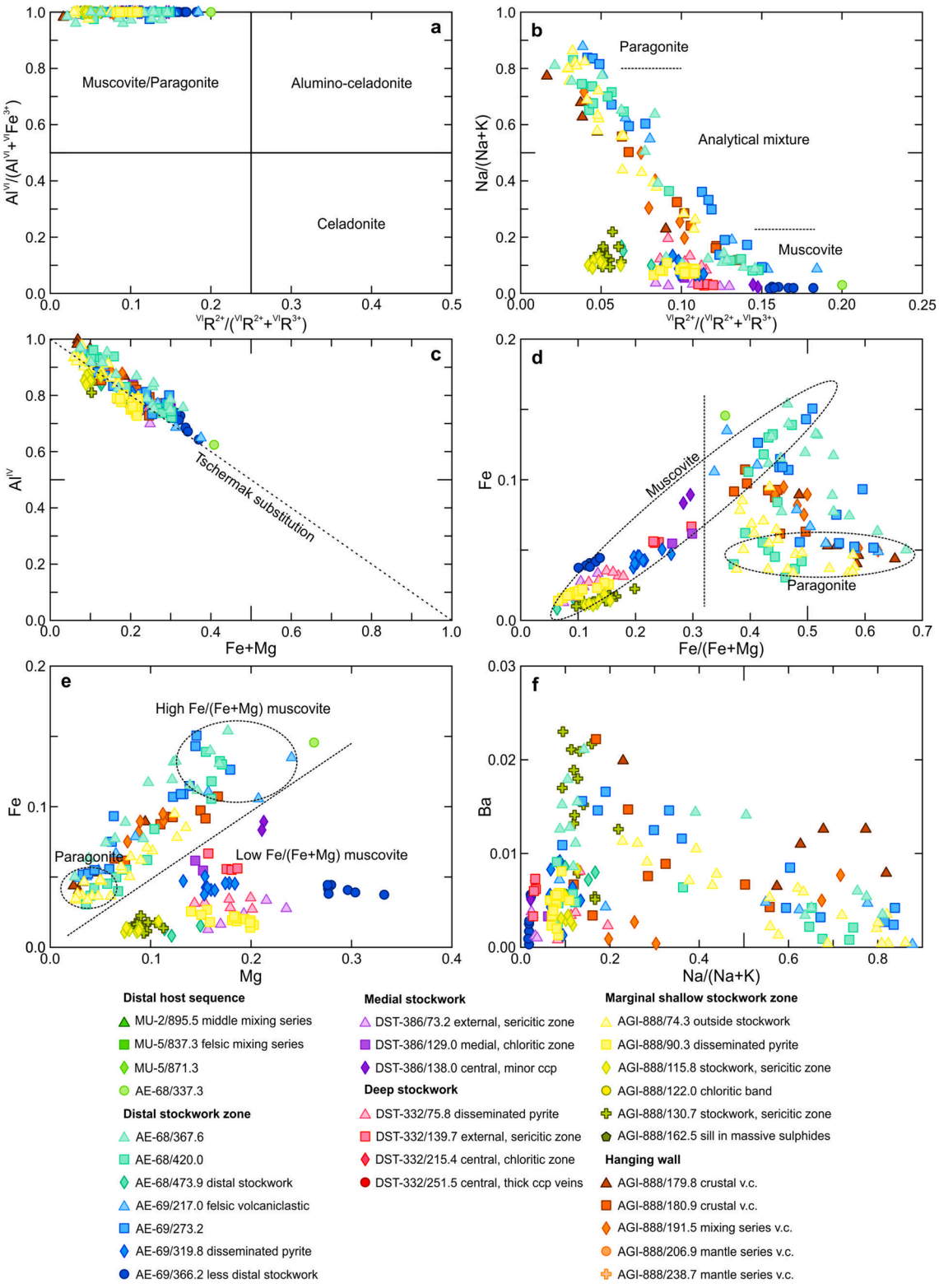

Fig. 6. Composition of white micas from the Aguas Teñidas deposit area derived from EMPanalysis. Cations calculated for 11 O with all Fe as Fe^{2+}. (a) Classification diagram of Rieder et al. (1998); Fe^{3+} was estimated as Fe + Mg + Mn + (Al^{IV}-1) – (Ti + Na + K + 2Ca + 2Ba), and constrained to be ≥ 0 and ≤ Fe. (b) Na/(Na + K) vs. $^{VI}R^{2+}/(^{VI}R^{2+}+^{VI}R^{3+})$ diagram to differentiate muscovite and paragonite. (c) Al^{IV} vs Fe + Mg diagram depicting the chemical trend associated to the Tschermak substitution. (d) Fe vs. Fe/(Fe + Mg) diagram; the dotted line separates high and low FeO/(FeO + MgO) micas described in the main text. (e) Fe vs. Mg diagram; the dotted line separates high and low FeO/(FeO + MgO) micas described in the main text. (f) Ba vs. Na/(Na + K) diagram.

analysis by either electron microprobe or LA-ICP-MS (Fig. 6b). Our data follow the ideal Tschermak substitution trend (Fig. 6c), with minor deviations that can be attributed to the effect of analytical uncertainty, interlayer cation deficiency, and Fe^{3+} content. Magnesium dominates over Fe, with molar Fe/(Fe + Mg) mostly below 0.5 (Fig. 6d). A positive correlation is observed between Fe and Fe/(Fe + Mg) in muscovite, whereas high Fe/(Fe + Mg) in paragonite occurs at low Fe associated with lower Mg (Fig. 6d, e). Indeed, paragonite presents lower phengicity compared to muscovite, with compositions close to the pure muscovite/paragonite end-member. Ba is a significant interlayer cation in some white micas, showing higher concentrations in muscovite (Fig. 6f).

Systematic variations in muscovite mineral chemistry have been observed for the Fe/(Fe + Mg) and Na/(Na + K) ratios, which can therefore be used as vectoring tools. Indicators based on oxide contents have been preferred to cations to reduce the amount of calculations required (Fig. 7). Three main parts of the system can be identified in diagrams in Fig. 7 which present different white mica characteristics: distal host rocks beyond the influence of the hydrothermal system, footwall proximal rocks, and hanging wall rocks.

4.2.1.1. Distal rocks. These are characterized by high FeO/(FeO + MgO) (>0.42) and low $Na_2O/(Na_2O + K_2O)$ (<0.05) (Fig. 7a-c, zone 1 in Fig. 7b).

4.2.1.2. Footwall proximal rocks. These include from rocks outside the stockwork system but with characteristics different from those of the distal rocks, to rocks at the centre of the feeder zone. Rocks in external zones present both muscovite and paragonite (e.g. AE-68/367.6, AE-69/217.0), which are characterized by high FeO/(FeO + MgO) (>0.45) and $Na_2O/(Na_2O + K_2O)$ (>0.05) (zone 2 in Fig. 7b). Rocks in internal zones bear low FeO/(FeO + MgO) (<0.45) muscovite, with variable $Na_2O/(Na_2O + K_2O) < 0.2$ (zones 3 to 5 in Fig. 7b).

Samples from cores AE-68 and AE-69 show the transition from distal rocks to the centre of the distal stockwork (Fig. 7c). Starting from distal compositions (e.g. AE-68/337.3), an increase in the $Na_2O/(Na_2O + K_2O)$ of muscovite occurs (>0.05) (trend 1 in Fig. 7c) when approaching the hydrothermal system, coupled with the appearance of paragonite in the mineral assemblage (trend 2) (e.g. AE-68/367.6, AE-69/217.0). Towards more internal locations, the FeO/(FeO + MgO) ratio of paragonite decreases (trend 3) (AE-68/420.0, also seen in AGI-888/74.3 outside the shallow stockwork), followed by a disappearance of paragonite and further decrease of FeO/(FeO + MgO) in muscovite (AE-69/319.8) (trend 4). Finally, at the centre of the distal stockwork, low FeO/(FeO + MgO) muscovite is present with medium (AE-68/473.9, more distal, zone 3 in Fig. 7b) to low (AE-69/366.2, more proximal, zone 4 in Fig. 7b) $Na_2O/(Na_2O + K_2O)$ (trend 5).

In more proximal or central cores, further evolution of muscovite composition when approaching the centre of the hydrothermal system is observed. In the marginal shallow stockwork in AGI-888 (Fig. 7d), a slight increase in FeO/(FeO + MgO) and $Na_2O/(Na_2O + K_2O)$ occurs when approaching the massive sulphides (trend 5′) (AGI-888/90.3, AGI-888/115.8, AGI-888/130.7). In the deeper stockwork (central in DST-332, lateral in DST-386, Fig. 7e) muscovite shows a decrease in $Na_2O/(Na_2O + K_2O)$ and an increase in FeO/(FeO + MgO) towards the centre of the system (trend 6), reaching higher FeO/(FeO + MgO) values but still below those of distal rocks and proximal rocks with paragonite (<0.45) (zone 5 in Fig. 7b). Sample AGI-888/162.5 (Fig. 7d), which was collected from a sill within the massive sulphides, represents an exception to the previously described behaviour. The rare muscovite in this sample has the highest FeO/(FeO + MgO) of all analysed muscovite (ca. 0.8), and $Na_2O/(Na_2O + K_2O) > 0.2$.

These mineral-chemical trends are coupled with mineralogical changes in the host rock, particularly related to oxides and sulphides. The most distal rocks with paragonite in the mineral assemblage bear Fe and Fe-Ti oxides, similar to regional protoliths. Towards the centre of the hydrothermal system, Fe oxide abundance decreases and rutile appears, representing the only oxide in the internal mineral assemblage. Paragonite with the lowest FeO/(FeO + MgO) (e.g. samples AE-68/420.0 and AGI-888/74.3) occurs in rocks where already only rutile is present. On the other hand, the transition to low FeO/(FeO + MgO) (<0.45) muscovite occurs in still more internal locations, apparently close to the first appearance of sulphides (e.g. disseminated pyrite in sample AE-69/319.8).

4.2.1.3. Hanging wall rocks. White micas in the hanging wall are characterized by high FeO/(FeO + MgO) (>0.45) and present variably high $Na_2O/(Na_2O + K_2O)$ contents above 0.05, with coexisting muscovite and paragonite in the most proximal samples (Fig. 7f). In the most distal analysed samples (AGI-888/206.9, AGI-888/238.7) paragonite is absent, but muscovite presents $Na_2O/(Na_2O + K_2O)$ values still above those of more distal rocks. Sample AGI-888/238.7 was collected in the albite alteration zone, and therefore still within the hydrothermal alteration halo of the deposit. Thus, we interpret that between distal and paragonite-bearing rocks there is a transitional area of higher $Na_2O/(Na_2O + K_2O)$ muscovite that, although not observed in the footwall, also likely exists (e.g. between AE-68/337.3 and AE-68/367.6). No clear trends are seen in the composition of muscovite and paragonite in the hanging wall rocks. However, the increase in the paragonite component within the white mica population towards the ore is likely to produce an overall increase in FeO/(FeO + MgO) and $Na_2O/(Na_2O + K_2O)$ of white micas.

4.2.1.4. Barium. Barium represents a major component of muscovite in some rocks around the Aguas Teñidas deposit, with up to 3 wt% BaO in sample AGI-888/162.5. BaO contents are predominantly below 0.4 wt% for muscovite and paragonite (which presents lower contents compared to coexisting muscovite, Fig. 6f), but higher concentrations occur in muscovite around the massive sulphides and stockwork (Fig. 6f, Fig. 8). In cores AE-68 and AE-69 in the distal stockwork area, Ba seems to peak along with Na in the paragonite-bearing zone. In the shallow stockwork (AGI-888), an initial decrease in Ba towards the massive sulphides (AGI-888/74.3 to AGI-888/90.3) is followed by a subsequent increase (AGI-888/90.3 to AGI-0.888/130.7). In the deeper stockwork, a decrease in Ba content towards the centre of the stockwork is observed in DST-332, although the opposite trend occurs in the lateral and slightly shallower DST-386. Thus, except for DST-386, Ba is seen to increase from distal to proximal locations, peaking along the margin of the hydrothermal system and within the massive sulphides, and decreasing towards the innermost parts of the stockwork system.

4.2.1.5. Comparison with VMS deposits in the IPB and other districts. There is no universal trend for all VMS districts and deposits regarding white mica composition, which therefore require individual study and characterization. According to Soltani Dehnavi et al. (2018a) there are two main trends of compositional variation:

1) phengitic and Ba-rich white mica occurs proximal to the massive sulphide horizon. Examples: Hellyer and Rosebery, Tasmania; several deposits in the Bathurst Mining Camp, Canada (Soltani Dehnavi et al., 2018a and references therein).
2) phengitic white mica occurs at the outer edge of the alteration zone, with sodic muscovite proximal to massive sulfides. Examples: Western Tharsis and Mt. Lyel, Tasmania; Highway Reward and Mt. Windsor subprovince, Queensland (Soltani Dehnavi et al., 2018a and references therein).

Within the IPB, VMS systems broadly fall within the first category of Soltani Dehnavi et al. (2018a) (e.g. Masa Valverde, Toscano et al., 1994b; Rio Tinto, Costa, 1996; Neves Corvo, Relvas et al., 2006). However, the presence of Na-muscovite in both external and internal

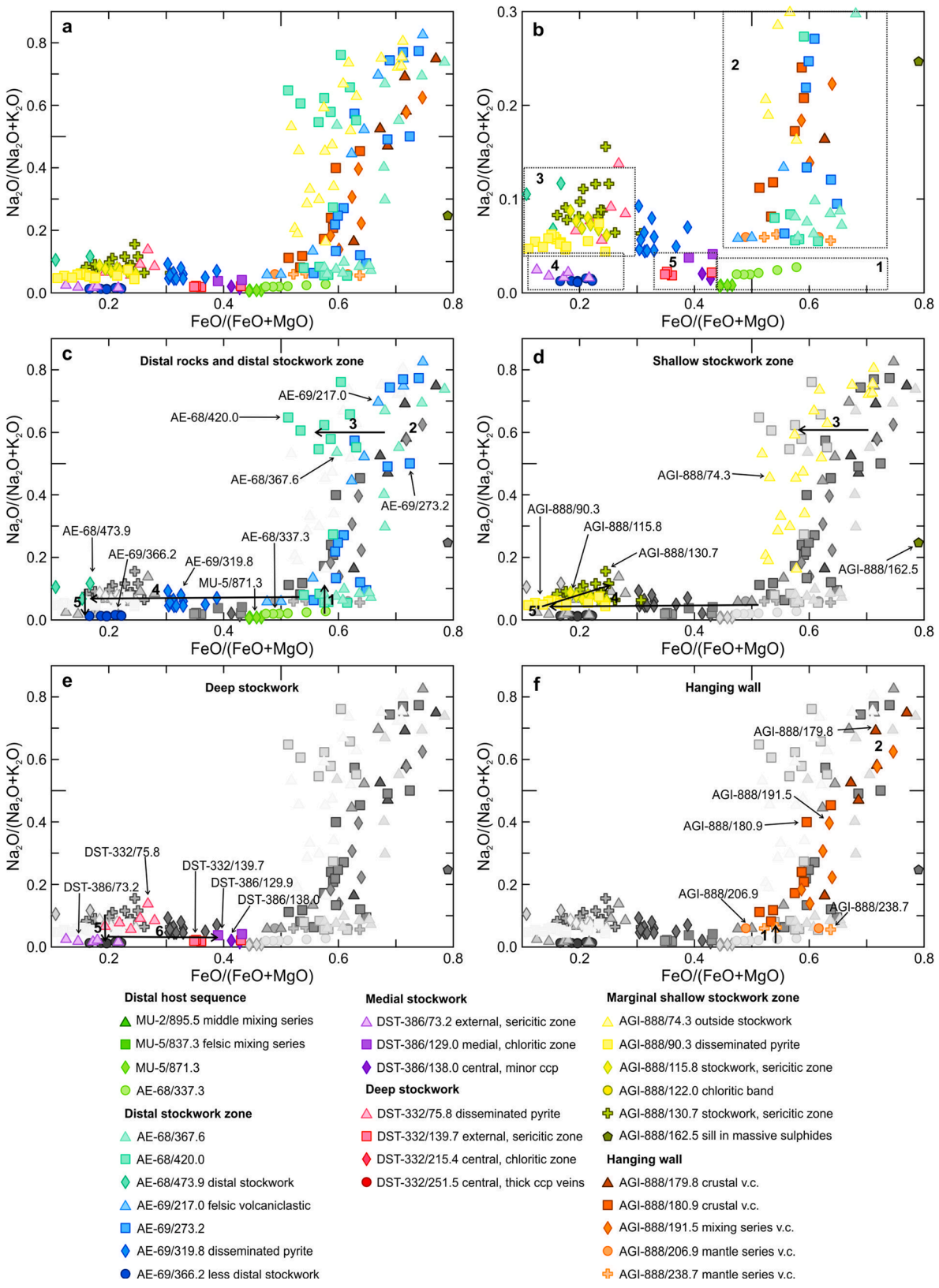

Fig. 7. Composition of white micas from the Aguas Teñidas deposit area derived from EMP analysis in a $Na_2O/(Na_2O + K_2O)$ vs. $FeO/(FeO + MgO)$ diagram. (a) all analyses. (b) lower $Na_2O/(Na_2O + K_2O)$ data. In diagrams (c) to (g) samples from specific zones of the studied system are presented in colour, whereas the remaining analyses are shown in grey scale for reference. Data with ΣM^{VI} between 2.05 and 2.1 a.p.f.u. are represented for samples MU-5/871.3, AE-68/337.3, AGI-888/206.9 and AGI-888/238.7, as these are the only ones available; in this case they can be used reliably (Supplementary Material 1.7).

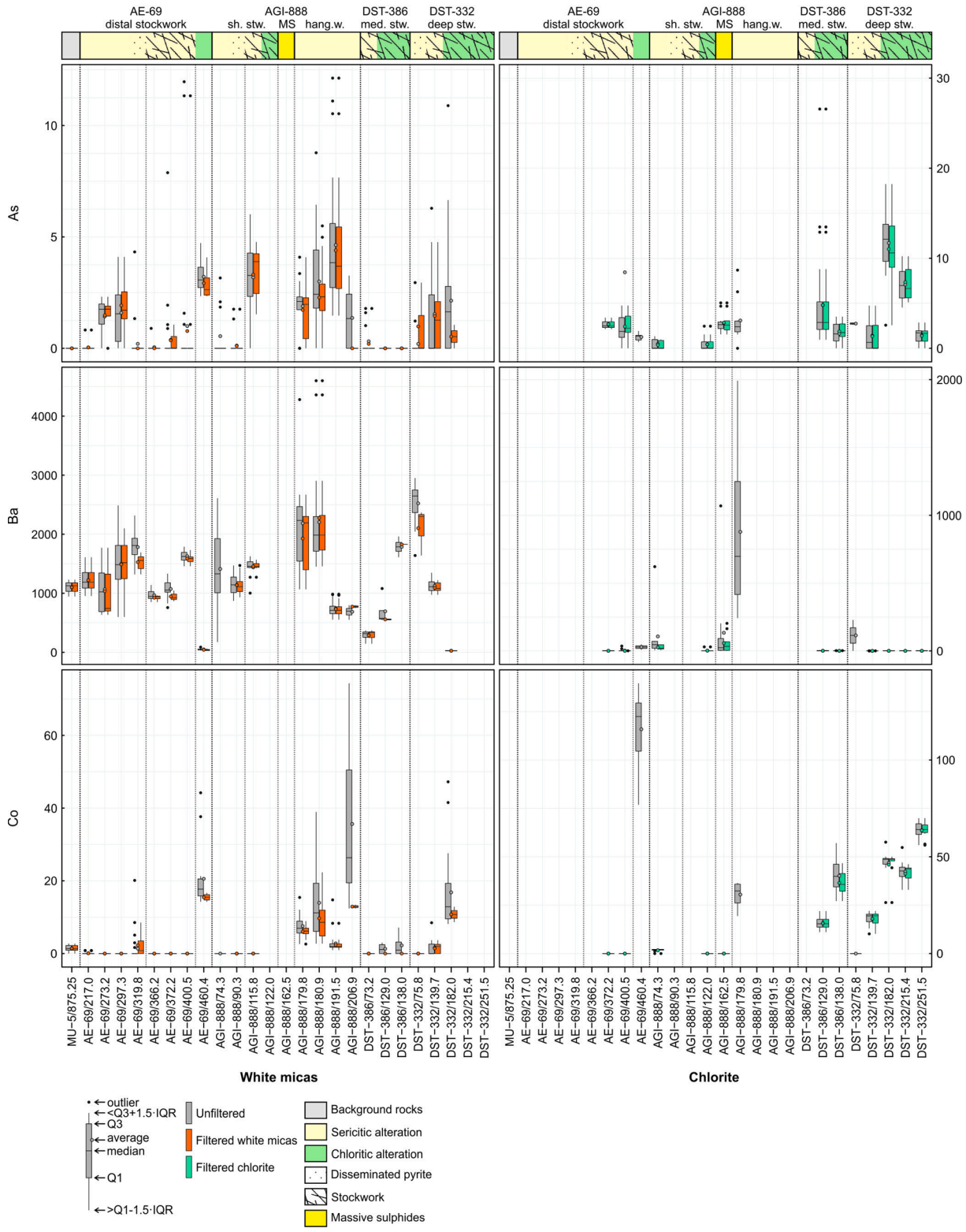

Fig. 8. Trace element contents (in $\mu g g^{-1}$) in white micas and chlorite measured by LA-ICP-MS analysis. sh. stw.: shallow stockwork; MS: massive sulphides; hang. w.: hanging wall; med. stw.: medial stockwork; deep stw.: deep stockwork.

parts of the system is not uncommon (e.g. Rio Tinto, Costa, 1996). Similar to Aguas Teñidas, Ba-rich micas occur in the innermost part of the system in Rio Tinto (up to 3.5 wt% BaO, Costa, 1996) and Masa Valverde (up to 5.78 wt% BaO, Toscano et al., 1994b). Toscano et al. (1994b) suggested that K/Ba in hydrothermal micas can be a good vector to ore in the VMS systems in the IPB, although this indicator does not produce distinctive trends at the Aguas Teñidas deposit.

Similar to other deposits in the IPB, the Aguas Teñidas deposit seems to combine the two main categories of Soltani Dehnavi et al. (2018a), with Na-Ba-muscovite proximal to the massive sulphides, and with

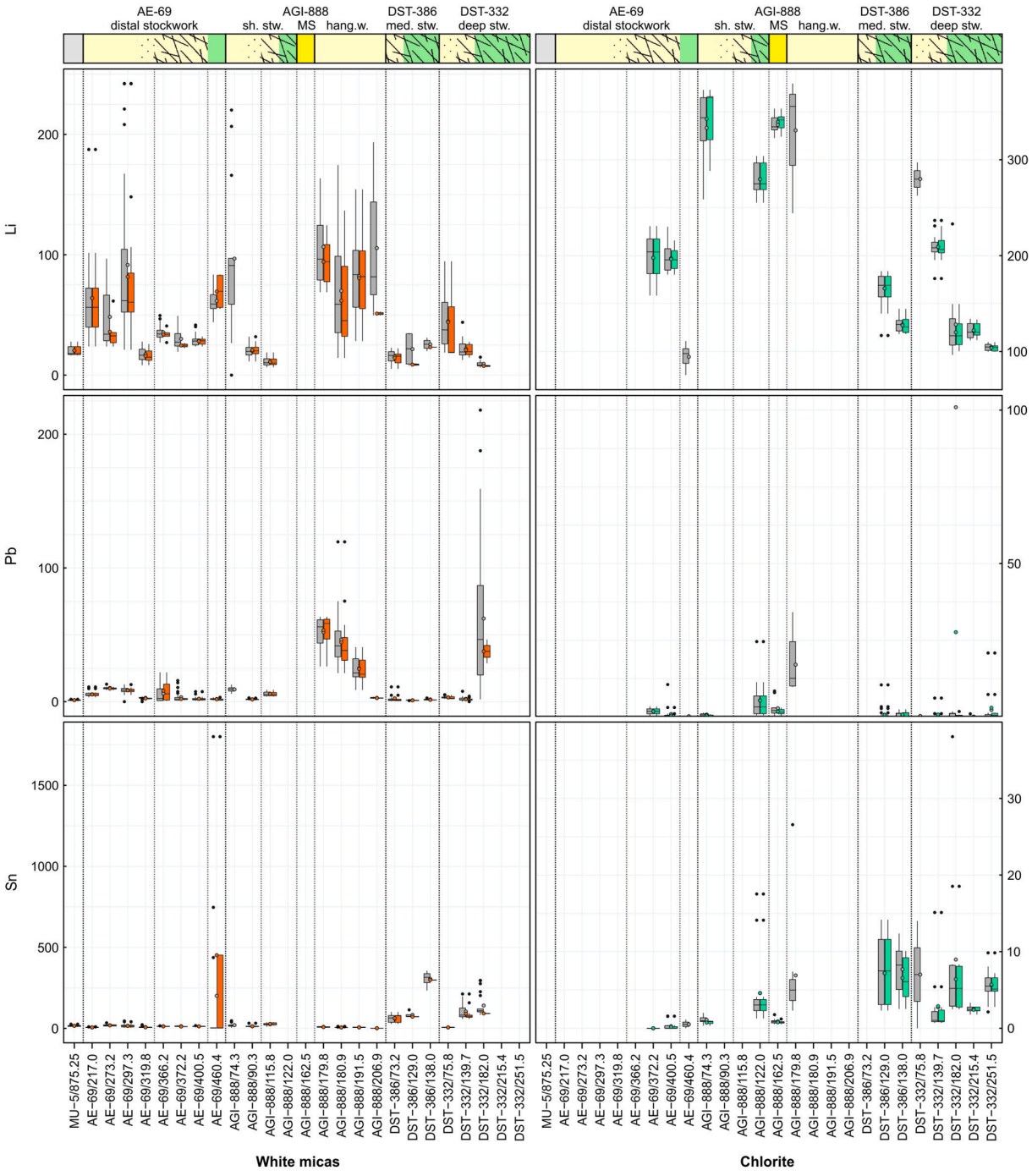

Fig. 8. (*continued*).

especially Na-rich white mica in the hanging wall and external parts of the system. However, in the influence area of the hydrothermal system, whereas systematic FeO/(FeO + MgO) variations have been observed with distance to ore, trends are not evident in phengicity.

4.2.2. Trace elements

Results of LA-ICP-MS analyses are provided in Supplementary Material 2, and contents of selected trace elements are depicted in Fig. 8. Concentrations were mostly below the detection limit or did not show any trend related to sample location within the system for many elements. However, systematic variations have been observed for Ba (described in the previous section), Cs, Li, Pb, Rb, Sn, Sr, Tl and Zn. In paragonite-bearing rocks, Ba, Cs, Li, Pb, Rb, Sr, Tl, V and Zn concentrations in each individual sample have been observed to broadly correlate to $Na_2O/(Na_2O + K_2O)$. LA-ICP-MS data indicate that Cs, Rb, Tl, V and Zn partition preferentially into muscovite, whereas Li, Pb and Sr partition into paragonite; this must be considered when describing and interpreting chemical trends, as different muscovite-paragonite analytical mixtures will produce different concentrations for these elements. Rubidium, Sr and Zn show trends similar to those of K_2O, Na_2O and MgO respectively, suggesting a close relationship between these elements.

Rubidium contents in white micas broadly correlate to K_2O (Fig. 9), although minor differences occur which are shown by the Rb/K_2O ratios (Fig. 10). A positive correlation between these two elements indicates that Rb substitutes for K in the crystal structure of white micas and, thus,

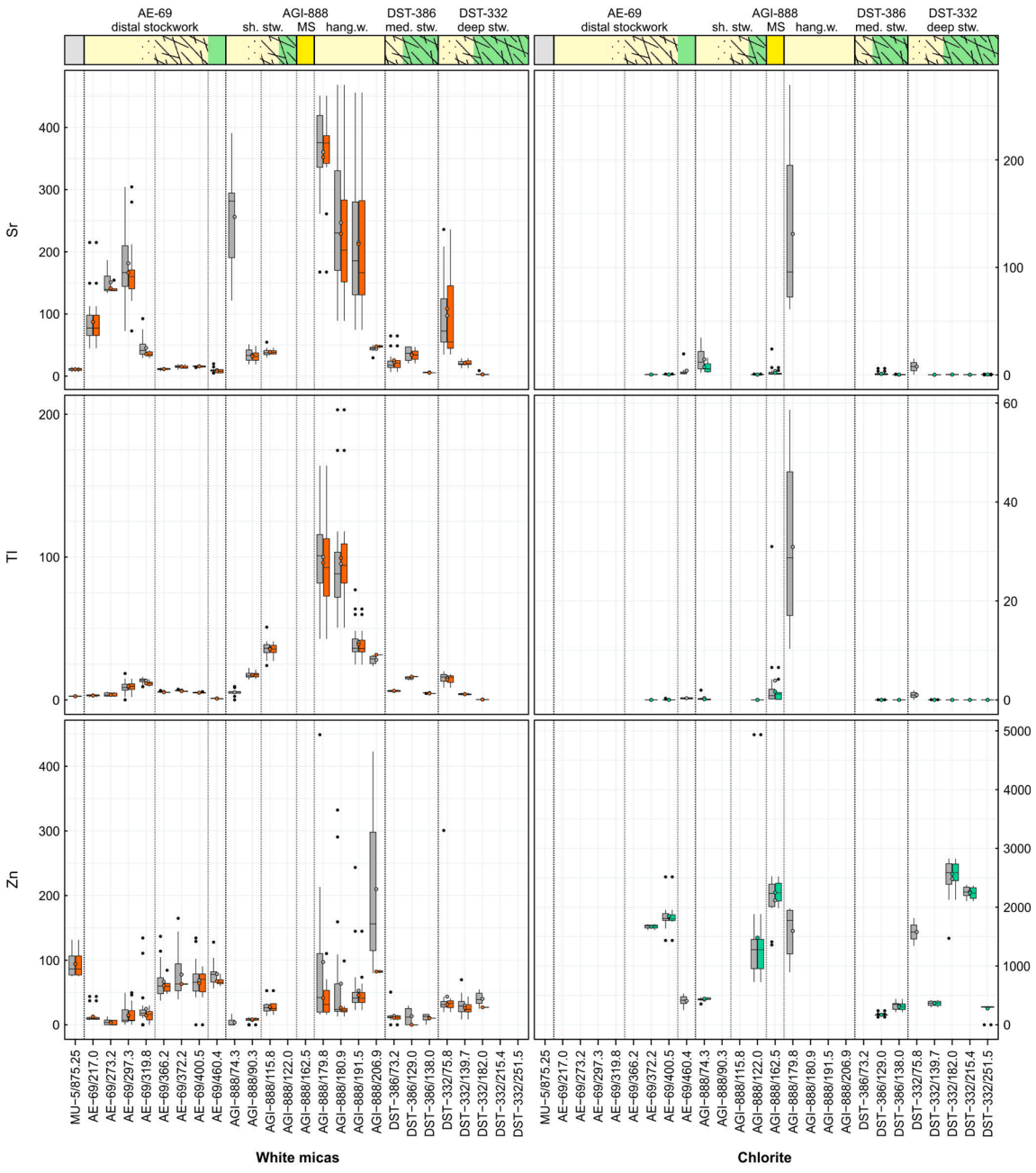

Fig. 8. (*continued*).

only minor contents are expected to occur in paragonite. Accordingly, the lowest Rb contents occur in paragonite-bearing samples (e.g. AE-69/273.2, AGI-888/74.3, AGI-888/179.8), which present concentrations below those of regional protoliths of equivalent initial composition (e.g. MU-5/875.25). However, low Rb values are also seen in distal mafic rocks (e.g. AE-69/460.4); indeed, different Rb contents in muscovite in felsic and mafic regional protoliths stress the importance of rock characterization when using chemical vectors to ore in order to discriminate trends related to hydrothermal influences as opposed to initial whole rock composition. The Rb/K_2O ratio has the advantage, compared to Rb concentration, of not being influenced by LA-ICP-MS data normalization or by the simultaneous analysis of muscovite and paragonite. The Rb/K_2O ratio shows trends across the hydrothermal system and can thus be used for vectoring purposes (Fig. 10). In the distal stockwork area in core AE-69, Rb/K_2O ratios are nearly constant beyond the mineralized area, with values slightly above those of regional protoliths (Fig. 10); hence, they present a minimum in the zone with disseminated pyrite outside the stockwork before increasing towards its centre. Within the deeper stockwork (DST-332, DST-386), an initial increase in Rb/K_2O occurs from external to medial parts of stockwork, followed by a decrease towards its centre. The trend is less evident in the shallow stockwork due to insufficient data. In the hanging wall, Rb/K_2O peaks above the massive sulphides, decreasing towards more distal locations.

Equivalent to Rb and K_2O, Sr contents in white micas broadly correlate to Na_2O (Fig. 9), mimicking its trends, although with minor differences which are more clearly seen in the Sr/Na_2O ratio (Fig. 10). Contents of Na_2O and Sr peak outside the stockwork system in the footwall, and in the proximal hanging wall, decreasing both away from the hydrothermal system and towards its centre (with the exception of the Na and Sr increase towards the massive sulphides in the marginal shallow stockwork in AGI-888). Like Rb/K_2O, the Sr/Na_2O ratio can also be used for vectoring purposes. In the distal stockwork area (core AE-

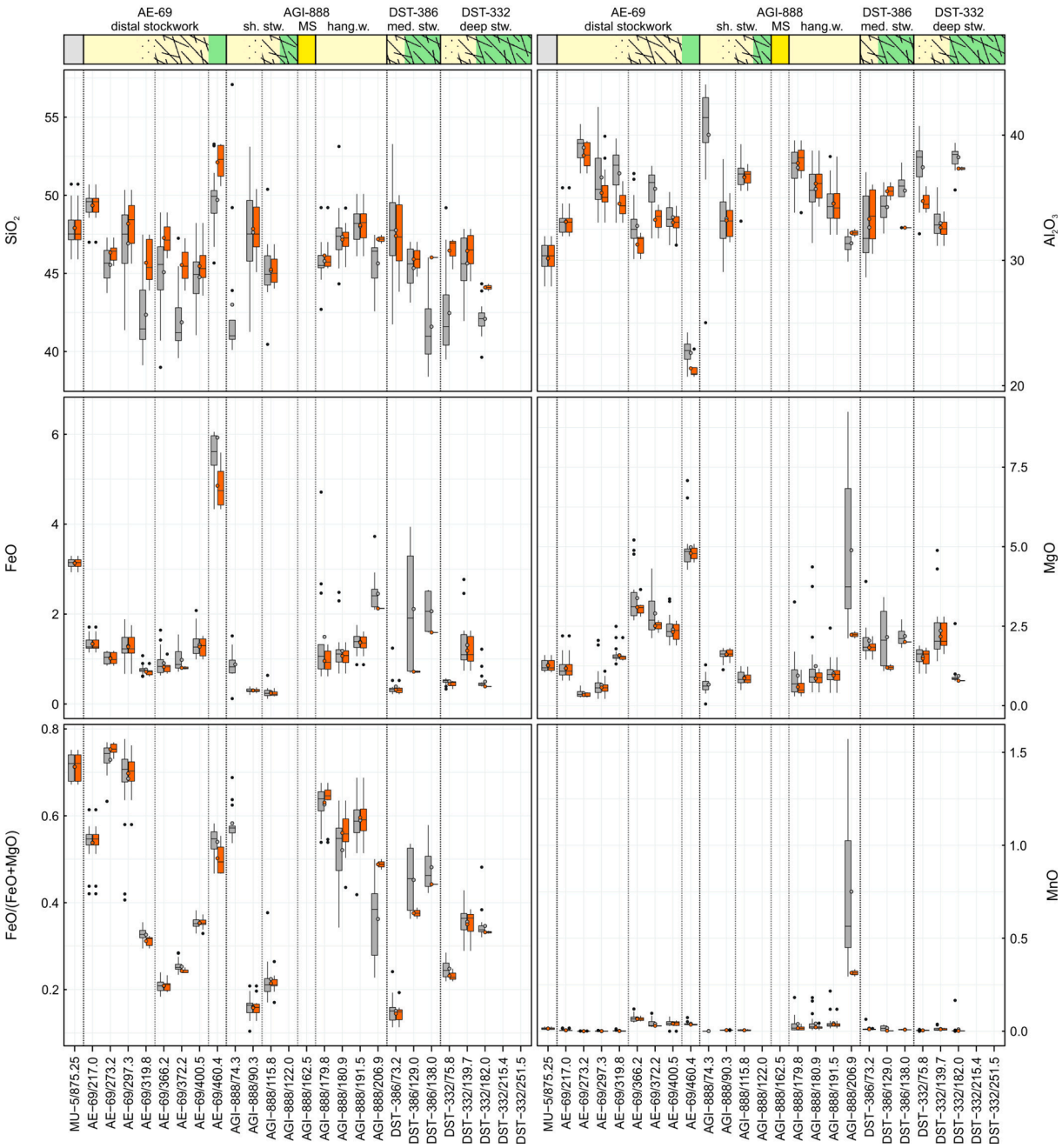

Fig. 9. Box and whiskers diagrams showing the major element composition (in wt. %) of white micas derived from LA-ICP-MS analysis.

69), paragonite-bearing rocks outside the stockwork system present nearly constant Sr/Na_2O values below those of distal rocks of equivalent initial composition, which then increase towards the centre of the distal stockwork. Changes in Sr/Na_2O ratio in other parts of the system are less well constrained by the available data. Remarkably, no significant changes occur along AGI-888, which goes from the external part of the shallow stockwork, through the massive sulphides, to the distal hanging wall, where lithologies change from felsic to intermediate in original composition. In core DST-386, Sr/Na_2O seems to consistently decrease from the margin towards the centre of stockwork, whereas in core DST-332 the highest value occurs in medial parts, decreasing towards the centre and outer parts of the stockwork. The high Sr/Na_2O in AE-69/460.4 is possibly related to its mafic original composition. The similarity between Rb and K on one hand, and Sr and Na on the other, is translated into similar behaviour of the $Sr/(Sr + Rb)$ and $Na_2O/(Na_2O + K_2O)$ ratios, which can therefore be used for vectoring purposes in an equivalent manner.

Zn concentrations in white micas broadly correlate with MgO (Fig. 9), with minor differences that are more clearly seen in the Zn/MgO ratio (Fig. 10). In this case, the correlation of Zn with $Na_2O/(Na_2O + K_2O)$ in paragonite-bearing samples relates to the different MgO contents in coexisting muscovite (higher MgO) and paragonite (lower MgO) (Fig. 6d and e). In the distal stockwork area, white micas in the paragonite-bearing rocks present Zn values below those of regional protoliths, which then increase towards the centre of the stockwork. In the shallow stockwork there also seems to be an increase in Zn towards the centre, towards the massive sulphides, whereas no clear trend is seen in the deeper stockwork. In the hanging wall there is a Zn concentration increase from paragonite-bearing proximal rocks to the paragonite-free more distal sample, towards values similar to regional protoliths. The

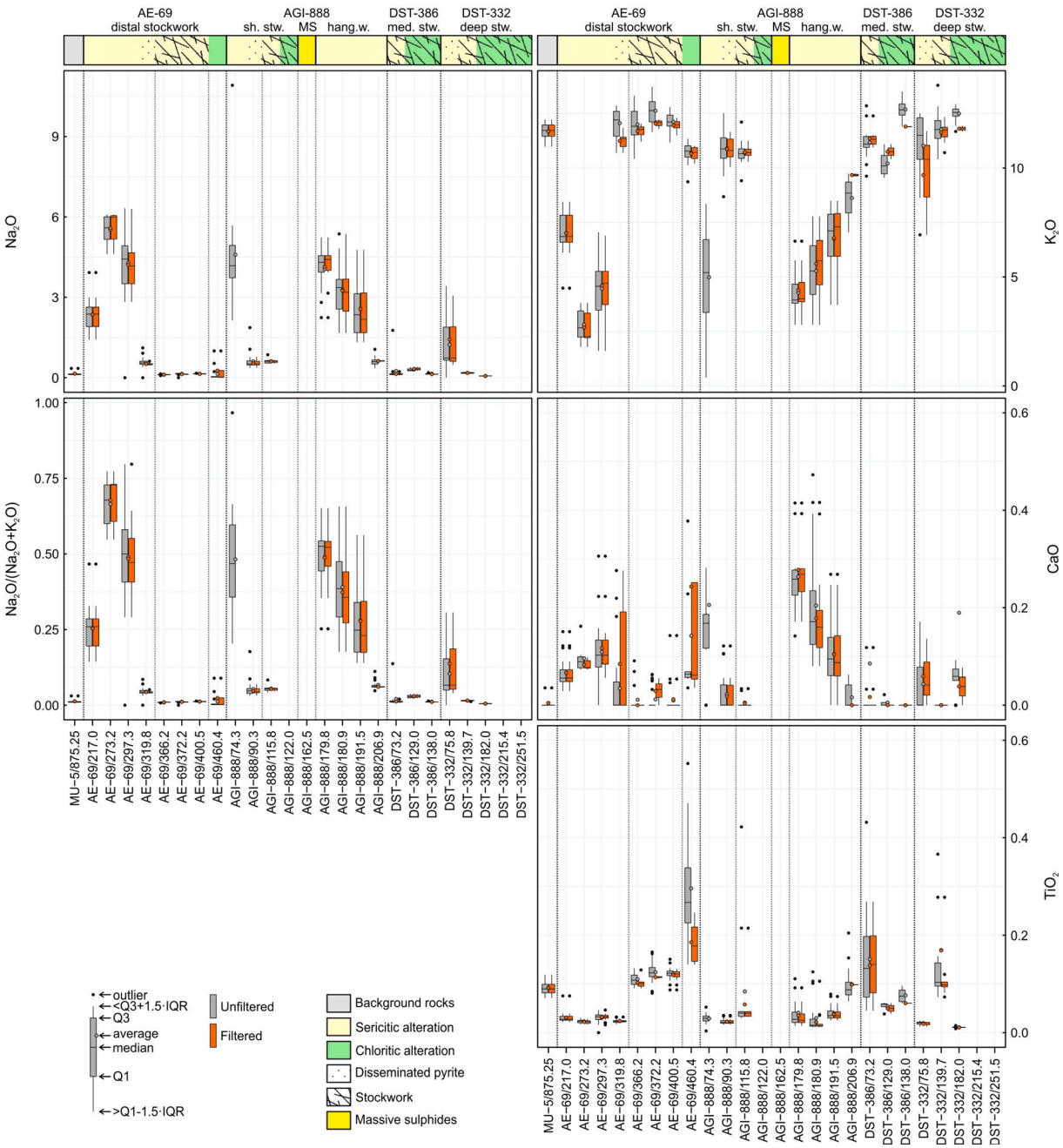

Fig. 9. (*continued*).

effect of the simultaneous analysis of paragonite and muscovite is reduced in the Zn/MgO ratio. Zn/MgO ratios are lower than background values along the margin of the hydrothermal system in the footwall, and increase towards its centre in all the studied drill cores except for DST-386. Zn/MgO ratios are remarkably high in the proximal hanging wall, with values in the most proximal sample being higher than in any other part of the hydrothermal system. From there, Zn/MgO ratios consistently decrease away from the massive sulphides. Our results indicate that Zn/MgO ratios can be used as a vectoring tool, with more consistent trends than those shown by Zn concentrations, which are influenced by the presence of paragonite.

No clear correlation has been found between Cs, Li, Pb, Sn and Tl and major elements. However, preferential partition of these elements into either muscovite or paragonite has a strong effect on the observed trends due to the inevitable analytical mixture in LA-ICP-MS data. Cesium and Li concentrations seem to peak along the margin of the hydrothermal system, decreasing away from it towards background values as well as towards its centre (e.g. AE-69, DST-332, Fig. 8). Lead contents in white micas are consistently low around the Aguas Teñidas deposit except for higher concentrations in the immediate hanging wall of the massive sulphides, with concentrations decreasing away from the mineralization. Slightly higher values also occur in the paragonite-bearing samples around the distal stockwork in AE-69. Due to this behaviour, Pb seems to represent a good vectoring tool in hanging wall alteration above the massive sulphides. Significant Sn contents have only been observed in rocks of the proximal deeper stockwork in DST-386 and DST-332, where enrichment occurs towards its centre. Thalium contents show consistent trends across the hydrothermal system, with low values in regional protoliths increasing towards the margin of the hydrothermal system, and then decreasing towards its centre (e.g. deep stockwork). The highest values occur around the massive sulphides in AGI-888, both in the hanging wall and footwall. In the distal stockwork, the highest

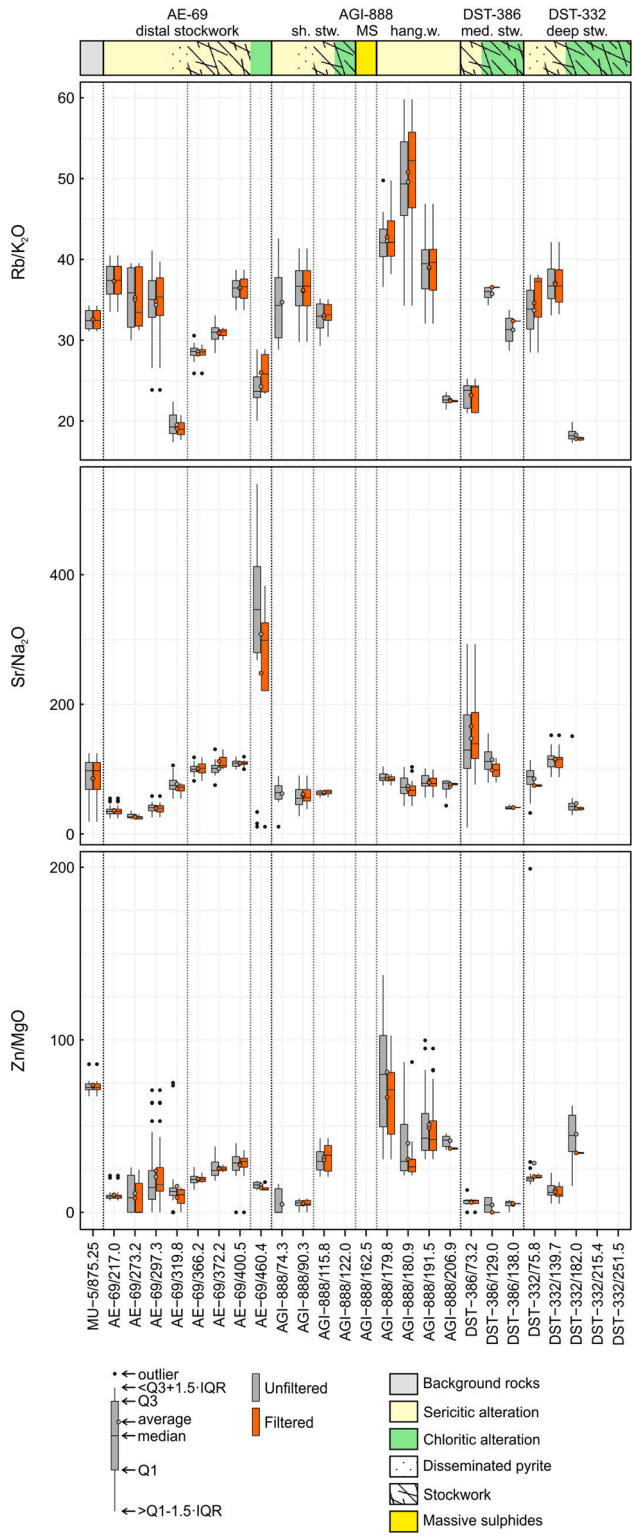

Fig. 10. Box and whiskers diagrams of Rb/K_2O, Sr/Na_2O and Zn/MgO ratios ($\mu g g^{-1}$/wt. %) in white micas measured by LA-ICP-MS analysis.

values occur along the margin of the stockwork, in the disseminated pyrite zone surrounding it (AE-69/319.8). In the more proximal stockwork in DST-386 the highest values occur in medial portions of the stockwork, whereas in the deep central stockwork in DST-332 they are found outside the stockwork. It is important to bear in mind that the profile across the massive sulphides studied here is located in a lateral position, above sericitic stockwork. Therefore, trends in more central locations (e.g. above chloritic or silicic stockwork) are likely to be different (e.g. depleted Tl in the immediate footwall within the chloritic stockwork as seen in the deep stockwork in cores DST-386 and DST-332).

Finally, analysed As contents are mostly <8 ppm. Although compositional trends are not marked, there seems to be an initial enrichment away from the massive sulphides in the proximal hanging wall.

4.2.2.1. Comparison with VMS deposits in the IPB and other districts. No other trace element data in white micas are available for the IPB. However, trace elements in muscovite have been explored as potential vectoring tools in other VMS districts, such as the Bathurst Mining Camp, Canada (Soltani Dehnavi et al., 2018a). In this district, white mica immediately adjacent (within 50 m) to the massive sulphides (in both the hanging wall and footwall) is enriched in Tl, Sb, Hg (most abundant volatile elements), and variably enriched in As, Sn, In, Se, Bi, and Cd. Contents in these elements decrease with distance, but were recognized up to several hundred meters away from mineralization. Soltani Dehnavi et al. (2018a) thus suggested that these elements could be used as vectors to mineralization as single elements in proximal locations, and as ΣTl + Sb + Sn + Hg in distal areas with lower concentrations.

4.3. Chlorite

4.3.1. Major elements

Although there is typically a large chemical variability in chlorite around VMS deposits, it can be described in most cases as mixtures between two extreme end-members: clinochlore $(Mg_{10}Al_2)(Si_6Al_2O_{20})(OH)_{16}$ and chamosite $(Fe^{2+}_{10}Al_2)(Si_6Al_2O_{20})(OH)_{16}$ (Bayliss, 1975; Wiewióra and Weiss, 1990; Large et al., 2001a, Franklin et al., 2005). Main substitutions include $Fe^{2+} \leftrightarrow Mg$, Tschermak $((Fe^{2+},Mg)^{VI} + Si^{IV} \leftrightarrow Al^{VI} + Al^{IV}$, towards amesite composition) and di-trioctahedral $(3(Mg, Fe^{2+})^{VI} \leftrightarrow \square + 2Al^{VI}$, towards sudoite composition) substitutions (Wiewióra and Weiss, 1990). Results of chlorite characterization by EMP analysis performed in this study are provided in Supplementary Material 2.

Even though several chlorite types can be identified within most samples at the Aguas Teñidas deposit (e.g. host rock vs. veins; different vein populations; different anomalous birefringence colours), intra-sample compositional variability is not significant, with analyses mostly clustering around a single composition (Fig. 11). This may reflect either formation of all chlorite in a given sample under similar conditions and/or re-equilibration of all chlorite populations within the sample.

Chlorite has been classified following Wiewióra and Weiss (1990) using WinCcac (Yavuz et al., 2015). All analysed crystals correspond to trioctahedral chlorite, with dominant clinochlore (Fe/(Fe + Mg) < 0.5 in a.p.f.u.) and minor chamosite, which is restricted to the innermost parts of the hydrothermal system (Fig. 11a and c). Chemical variability is dominated by Fe ↔ Mg (Fe/(Fe + Mg) ca. 0.05 to 0.7, Fig. 11d) and Tschermak (Al^{IV} 1.0 to 1.5 a.p.f.u., and Al ca. 2.25 to 3 a.p.f.u., Fig. 11a and b) substitutions, with minor di-trioctahedral substitutions resulting in low vacancies (<0.2 a.p.f.u.). The Fe/(Fe + Mg) ratio in the analysed chlorite broadly correlates negatively to F content (Fig. 11f), with chlorite in samples AGI-888/122.0 and AGI-888/238.7 falling outside the trend.

Compositional differences have been observed between chlorite in regional protoliths and in locations proximal to and within the hydrothermal system; in addition, systematic compositional variations occur in the latter group. These variations mostly relate to the molar Fe/(Fe + Mg) ratio and Al content. Chlorite from the regional background ("Distal host sequence" in diagrams) presents lower Tschermak substitutions; it has lower Al and higher Si and Fe + Mg compared to proximal chlorite (Fig. 11a and b), thus being closer to the clinochlore-chamosite end

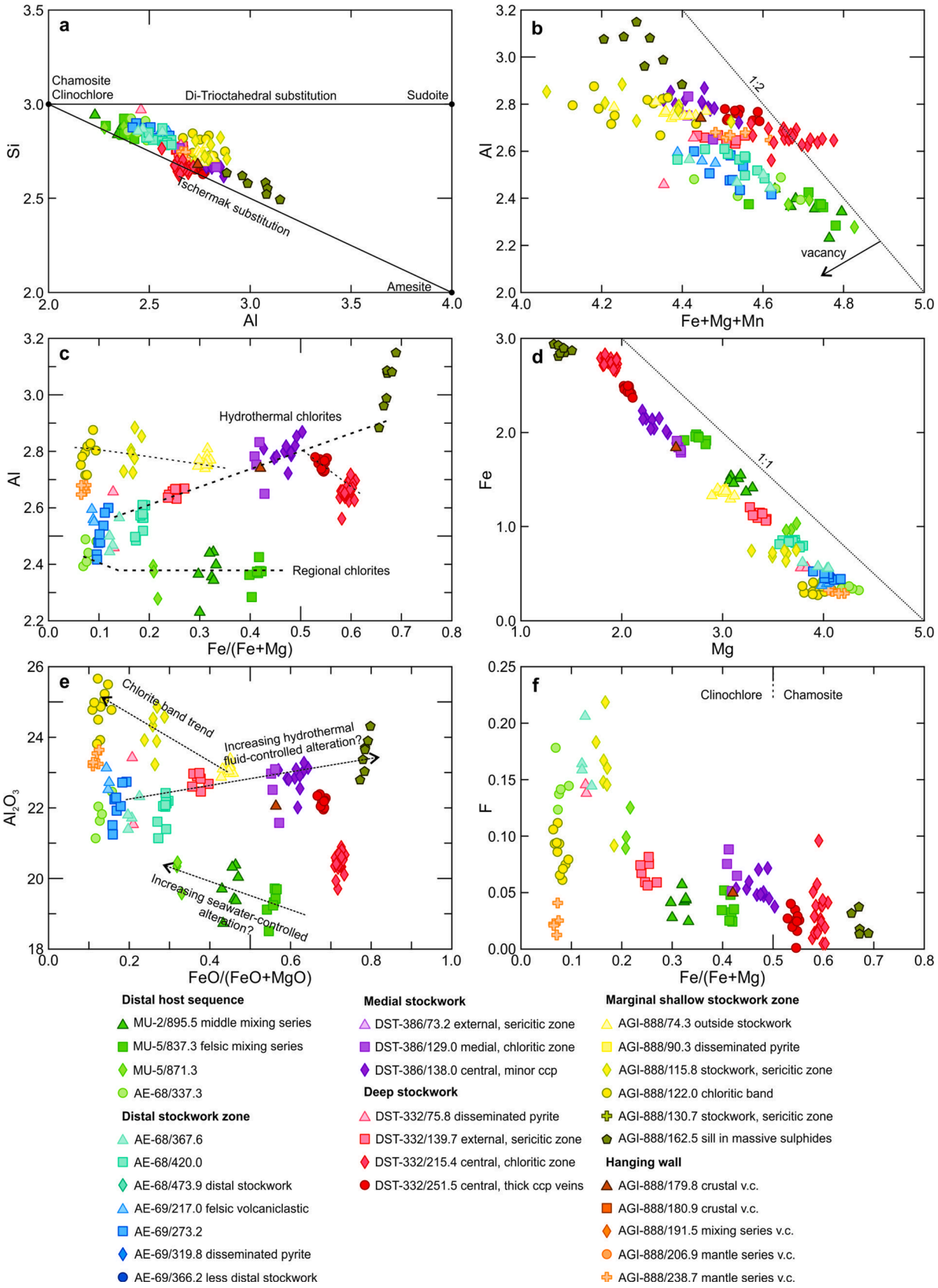

Fig. 11. Composition of chlorites from the Aguas Teñidas deposit area derived from EMP analysis. Cations calculated for 14 O with all Fe as Fe^{2+}. Element units are atoms per formula unit; oxides are wt. %. (a) Si vs. Al diagram showing the Tschermak and di-trioctahedral substitutions; modified from Trincal and Lanari (2016). (b) Al vs. Fe + Mg + Mn diagram with a dotted line indicating the ideal Tschermak substitution. (c) Al vs. Fe/(Fe + Mg) diagram; trends are described in the main text. (d) Fe vs. Mg diagram; the dotted line indicates the ideal Fe-Mg substitution. (e) Al_2O_3 vs. FeO/(FeO + MgO) diagram; interpretations are described in the main text. (f) F vs. Fe/(Fe + Mg) diagram.

member. This difference in Al contents is evident in the Al vs. Fe/(Fe + Mg) diagram (Fig. 11c), where distal chlorite has Al values <2.5 a.p.f.u., whereas proximal chlorite mostly has Al contents >2.5 a.p.f.u. Within the distal chlorite, there seems to be no correlation between Al and Fe/(Fe + Mg), with only sample AE-68/337.3 presenting slightly higher Al contents at low Fe/(Fe + Mg); this could indicate a transitional character of this sample towards chlorite compositions influenced by the hydrothermal system (e.g. AE-68/367.6, AE-69/217.0), which will be discussed later. In the most distal samples (cores MU-2 and MU-5), similar Al contents occur in rocks with different initial compositions (e.g. felsic in MU-5/837.2 and MU-5/871.3, intermediate in MU-2/895.5). The Fe/(Fe + Mg) ratio neither correlates with the original rock composition; for instance, chlorite in samples with the same initial composition (e.g. URD samples MU-5/871.3 and AE-68/337.3) presents markedly different ratios. Samples from the proximal areas around the stockwork in the footwall (e.g. paragonite-bearing rocks in cores AE-68 and AE-69) are close to the low Fe/(Fe + Mg) end of the trend depicted by background chlorites. From these compositions, samples from cores AE-68, AGI-888, DST-332, and DST-386 mostly show increasing Al and Fe/(Fe + Mg) values towards the centre of the hydrothermal system, peaking in sample AGI-888/162.5 within the massive sulphides. Exceptions to this main trend are: 1) sample DST-332/215.5 and to a lesser degree DST-332/251.5; 2) samples AGI-888/115.8 and AGI-888/122.0, which were collected from within and close to the chlorite band in the shallow stockwork described in Gisbert et al. (2021); and 3) sample AGI-888/238.7, from the most distal area of the proximal hanging wall.

The origin of these apparent trends and the possible causes for deviations from them are covered in the discussion section. However, our data already show that Al content can be used to discriminate between chlorite from proximal (influenced by hydrothermal fluids) and distal (dominated by seafloor metasomatism) locations, and that, within the hydrothermal system, the Fe/(Fe + Mg) ratio in chlorite vectors towards its centre. Differentiation between distal and proximal chlorites is crucial, as Fe/(Fe + Mg) variation may not be systematic outside the influence area of hydrothermal fluids as shown by regional protoliths. Element mass concentrations derived from EMP analysis can also be directly used for vectoring purposes, although there may be more overlap between Al_2O_3 contents in distal and proximal chlorite (e.g. sample AE-68/337.3 is richer in Al_2O_3 than DST-332/215.4) (Fig. 11e).

4.3.1.1. Comparison with VMS deposits in the IPB and other districts. Systematic detailed studies of chlorite compositional trends at other deposits in the IPB are needed, as most characterizations are generic. Sánchez-España et al. (2000) described altered felsic volcanic rocks in the northern IPB as showing a general trend of lower Fe/(Fe + Mg) in hydrothermal alteration chlorites compared to regional varieties. However, in the Rio Tinto area the opposite trend has been observed (Costa, 1996), and at the Aguas Teñidas deposit Fe/(Fe + Mg) in hydrothermal and background chlorites overlap. Regarding trends within the hydrothermal system, divergence in alteration trends is also observed; in La Zarza and Rio Tinto deposits Fe/(Fe + Mg) in chlorite decreases from distal to inner chlorites (Strauss et al., 1981; Leistel et al., 1994; Costa, 1996), whereas the opposite is observed at Masa Valverde and Aznalcóllar deposits (Toscano et al., 1993; Almodóvar et al., 1998). Toscano et al. (1994a) also describe for the Masa Valverde deposit a decrease in Fe relative to Mg with depth within the inner part of the hydrothermal alteration halo and, in the most chloritized areas, the presence of aluminous chlorite together with chamositic chlorite. More work is required for the appropriate characterization of this vector in the IPB.

The Fe/Mg ratio has long been suggested to be a useful VMS vector to ore (e.g. Lydon, 1988). However, as in the IPB, studies and reviews show that Fe-Mg compositional changes, although large, may not be systematic (e.g. Large et al., 2001a). For example, in the Seneca, Southbay, and Corbet deposits in Canada, Mg content of Fe-Mg chlorite commonly increases passing from the margin to the core of the footwall alteration system (Urabe et al., 1983). An opposite trend is described in the Bathurst Mining Camp, also in Canada, where the Fe content in chlorite increases towards the ore (e.g Heath Steele, Lentz et al., 1997). In addition, in the less altered portions of the system with lower fluid/rock ratios (e.g. regional protoliths) chlorite composition can be strongly conditioned by the initial host rock/sediment composition, overlapping the entire compositional range of hydrothermal-related chlorite (Large et al., 2001a, Herrmann et al., 2001, Gemmell and Fulton, 2001). Therefore, this tool needs to be investigated in detail in every district.

4.3.2. Trace elements

Results of LA-ICP-MS analyses are provided in Supplementary Material 2. The study of trends in trace element contents in chlorite is hampered by the lower number of samples from which reliable data could be obtained compared to muscovite. This was mostly due to the low abundance and small size of chlorite crystals and patches in rocks from the external zones of the hydrothermal system, which precluded appropriate targets for LA-ICP-MS analysis. In addition, for many of the analysed elements, contents were mostly below the detection limit or did not show any trend related to sample location within the system. Nevertheless, systematic variations have been observed in the contents of As, Co, Li and Zn (Fig. 8). Ba, Rb, Sr and Tl, which are useful vectoring tools in white micas, are not found in significant amounts in chlorite.

In the deep stockwork in cores DST-386 and DST-332 As contents seem to peak in medial parts of the feeder system (samples DST-386/129.0 and DST-332/182.0), decreasing both towards its centre and towards its margin. In the distal stockwork, the highest As contents seem to occur at its centre, with concentrations decreasing outwards. Co contents above the detection limit mainly occur in the deep stockwork in cores DST-386 and DST-332, where an increase in Co concentration in chlorite is seen towards the centre of the stockwork. In the deep stockwork, Li contents decrease from the margin towards the centre of the stockwork. High values also occur along the margin of the shallow stockwork (sample AGI-888/74.3), and remarkably also in the chloritic band in AGI-888/122.0 and within the massive sulphides (AGI-888/162.5). Thus, Li in chlorite seems to behave like in muscovite, with contents peaking along the margin of the hydrothermal system in the footwall, and decreasing both outwards and inwards except for the peak in the massive sulphides. Li contents in chlorite are higher than those in white micas. Although trends for Zn contents are less clear, this element seems to exhibit an increase above background values towards the centre of the hydrothermal system, but with depletion in its most central parts, where intense chloritic alteration and chalcopyrite occur. Zinc contents in chlorite are an order of magnitude higher than those in coexisting muscovite. Finally, although Sn shows no systematic trends, its contents seem to be higher in the deep stockwork (DST-386, DST-332).

4.3.2.1. Comparison with VMS deposits in the IPB and other districts. No previous data on the trace element contents in chlorite are available for the IPB. Trace elements in chlorite in combined chlorite-white mica pair studies have been recently proposed as a useful vector to ore, especially in proximal zones (e.g. Bathurst Mining Camp, Canada, Soltani Dehnavi et al., 2019). In the Bathurst Mining Camp, chlorite presents a behaviour similar to that of white mica, with fluid-mobile element enrichment with proximity to ore (e.g. Tl, Sb, Sn, and Hg), although this enrichment is several times lower than in coexisting white mica (Soltani Dehnavi et al., 2019). In the proximal footwall and hanging wall (up to 100 m from ore), fluid-mobile element enrichment was observed to be relatively systematic, whereas in more distal areas increased variability is conditioned by protholith whole rock composition (Soltani Dehnavi et al., 2019). Based on this behaviour, combined with typically decreasing chlorite contents in the alteration mineral assemblage with distance to ore, the authors argued that trace elements in chlorite are a less useful

vector compared to white mica. Our observations support this conclusion.

4.4. Carbonates

The use of carbonates as vectoring tool requires special attention because of the several generations of carbonates that typically occur within rocks hosting VMS deposits. The full vectoring potential of carbonates may be realised through discrimination of phases formed during mineralization-related alteration, which typically occur as disseminated patches and veins; whereas information obtained from late post-mineralization veins (e.g. formed during metamorphic and tectonic deformation stages) is of limited use (e.g. Large et al., 2001b; Tornos, 2006). Therefore, correct identification and characterization of carbonate phases and generations is of great importance. Carbonates associated with VMS deposits typically consist of calcite ($CaCO_3$), dolomite ($CaMg(CO_3)_2$), ankerite ($CaFe(CO_3)_2$), and siderite ($FeCO_3$). Results of carbonate characterization by EMP analysis performed in this study are provided in Supplementary Material 2.

At the Aguas Teñidas deposit, three main carbonate phases were identified: calcite, dolomite and ankerite (Fig. 12). Carbonates in distal rocks are calcite, found mostly as veins, groundmass patches or vesicles fill. Proximal rocks contain calcite, with additional dolomite or ankerite depending on location. Fe content in dolomite increases towards the centre of the hydrothermal system, with ankeritic compositions occurring in the most central parts (Fig. 12b). Low Fe contents in dolomite from the Mg-rich sample AGI-888/122.0 are consistent with other whole-rock and mineral chemistry presented in previous sections for this sample, further supporting a separate origin for this chlorite band within the sericitic stockwork (Gisbert et al. 2021).

4.4.1. Comparison with VMS deposits in the IPB and other districts

In the IPB, systematic studies on carbonate minerals compositions are rare. However, as in the Aguas Teñidas deposit, ankerite has been commonly reported in the central parts of the hydrothermal system and massive sulphides (Tornos, 2006; e.g. Masa Valverde, Toscano et al., 1993; Tharsis; Tornos et al., 1998; Migollas, Velasco-Acebes et al., 2019). A significant detailed study is that by Velasco-Acebes et al. (2019), performed in the shale-hosted Migollas deposit. In this deposit, carbonate content in shale away from it is low; instead, carbonates are mostly related to hydrothermal alteration. Carbonates fall within the siderite-magnesite series, with increasing Fe content with proximity to ore (Velasco-Acebes et al., 2019). In addition, carbonate-rich ores have been described at Sotiel-Migollas and Tharsis, which consist of ankerite, ferroan dolomite and Mg-rich siderite, with Fe content increasing towards the base of the massive sulphides in the Migollas orebody (Velasco-Acebes et al., 2019).

The carbonate chemical trend observed at the Aguas Teñidas deposit is similar to those seen in other VMS districts. In deposits of the Cambrian Mt. Read Belt in Tasmania, hydrothermal alteration-related carbonates occur mostly in areas close to orebodies in both the footwall and hanging wall (Large et al., 2001a and references therein); distal carbonates within the less altered samples are relatively pure calcite and dolomite, which increase in Fe (towards siderite and ankerite compositions) and/or Mn towards the ore. At the K Lens of Rosebery deposit, Large et al. (2001b) describe Mn content in disseminated carbonate as an excellent vector to ore, with contents increasing with proximity to ore over distances of up to 200 m. Similar trends (dolomite to Mn-bearing siderite) in carbonate composition have been described in other areas, such as in the footwall alteration zone of the Mattabi deposit in Canada (Franklin et al., 1975). At the Aguas Teñidas deposit, higher Mn contents

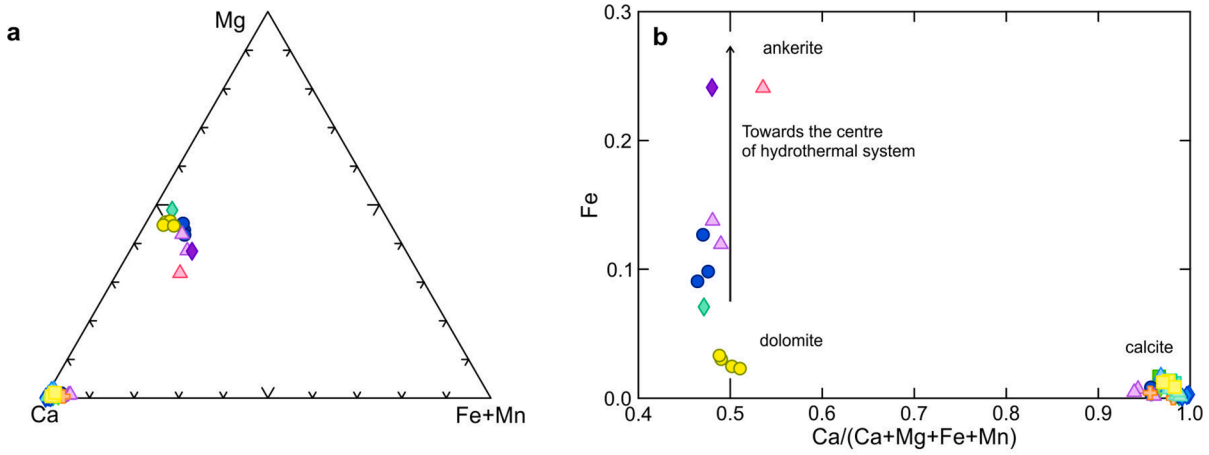

Distal host sequence
- MU-2/895.5 middle mixing series
- MU-5/837.3 felsic mixing series
- MU-5/871.3
- AE-68/337.3

Distal stockwork zone
- AE-68/367.6
- AE-68/420.0
- AE-68/473.9 distal stockwork
- AE-69/217.0 felsic volcaniclastic
- AE-69/273.2
- AE-69/319.8 disseminated pyrite
- AE-69/366.2 less distal stockwork

Medial stockwork
- DST-386/73.2 external, sericitic zone
- DST-386/129.0 medial, chloritic zone
- DST-386/138.0 central, minor ccp

Deep stockwork
- DST-332/75.8 disseminated pyrite
- DST-332/139.7 external, sericitic zone
- DST-332/215.4 central, chloritic zone
- DST-332/251.5 central, thick ccp veins

Marginal shallow stockwork zone
- AGI-888/74.3 outside stockwork
- AGI-888/90.3 disseminated pyrite
- AGI-888/115.8 stockwork, sericitic zone
- AGI-888/122.0 chloritic band
- AGI-888/130.7 stockwork, sericitic zone
- AGI-888/162.5 sill in massive sulphides

Hanging wall
- AGI-888/179.8 crustal v.c.
- AGI-888/180.9 crustal v.c.
- AGI-888/191.5 mixing series v.c.
- AGI-888/206.9 mantle series v.c.
- AGI-888/238.7 mantle series v.c.

Fig. 12. Composition of carbonates in rocks around Aguas Teñidas deposit derived from EMP analysis. Contents in atoms per formula unit calculated for 6 O. (a) Ca - Mg - (Fe + Mg) Ternary plot. (b) Fe vs. Ca/(Ca + Mg + Fe + Mn) diagram.

seem to occur in calcite associated with sulphides, whereas lower contents are found in barren veins (even within the same sample), as well as in rocks outside the hydrothermal system. However, more data and better carbonate-bearing veins characterization are needed to confirm these trends within calcite, as well as in dolomite.

5. Discussion

A detailed discussion of the causes of changes in the major element composition of white micas and chlorites in different parts of the hydrothermal system using thermodynamic modelling (e.g. Walshe, 1986; Schardt et al., 2001) is beyond the scope of the present study, and thus further work in this field is needed. However, some preliminary observations are made regarding elements and ratios which have been shown to be useful vectors to ore. These are the FeO/(FeO + MgO) and Na_2O/($Na_2O + K_2O$) ratios in white micas, and the FeO/(FeO + MgO) ratio and Al content in chlorite. The observed white micas and chlorite compositions reflect influences from protolith composition, that of interacting fluids (seawater and hydrothermal fluids, and their mixtures), degree of fluid/rock interaction, element partitioning (K_D) between coexisting mineral phases, physicochemical conditions (temperature, pressure, pH, fO_2, fCO_2 and fS_2), as well as the overprinting effects of diagenesis and metamorphism (e.g. Guidotti, 1984; Guidotti et al., 1994a,b; Inoue et al. 2009; Bourdelle et al., 2013; Lanari et al., 2014). In such open system, the interpretation of white micas and chlorite compositions can be complex; for the Aguas Teñidas deposit, the homogeneous initial rock composition in the footwall (URD host dome) makes interpretation possible.

The marked differences between the mineral chemistry of white micas and chlorite in distal and proximal rocks, and the systematic variations within different parts of the hydrothermal system, indicate that the resulting composition of these phases was mostly controlled by processes related to seafloor metasomatism and hydrothermal alteration, thus mostly contemporaneous with ore emplacement. Therefore, although some re-equilibration and re-crystallization may have occurred during subsequent diagenesis and low-grade metamorphism, it is suggested that these did not have a significant effect on mineral chemistry.

Hydrothermal fluids in VMS feeder systems are typically a mixture of deep hydrothermal fluids (hot, Fe-rich, mostly reducing) and seawater (cooler, Mg-rich, usually oxidized) (Large et al., 2001a; Franklin et al., 2005; Hannington, 2014). In proximal locations (i.e. within the hydrothermal system), higher fluid/rock ratios result in hydrothermal fluids exerting greater control on final rock and mineral compositions. On the other hand, in distal locations, seafloor metasomatism typically occurs at lower fluid/rock ratios, thus resulting in greater control from the protolith composition (e.g. Large et al., 2001a). Besides a change in the fluid/rock ratio, as hydrothermal fluids flow upwards and outwards within the system, progressive interaction with host rocks and mixing with external fluids produces a change in their physicochemical properties – e.g. cooling, variations in elements which partition into precipitating or recrystallizing phases, shift from hydrothermal fluid-dominated to seawater-dominated compositions. These progressive systematic changes with depth and distance from the centre of the hydrothermal system are the source of distinct mineralogically and geochemically zoned alteration halos, which are the base for most vectoring tools used in the exploration and characterization of VMS systems (Large et al., 2001a; Gibson et al., 2007).

5.1. Major elements in white micas

White micas analysed in this work form from the transformation of original hydrothermal smectite, illite, and mixed-layer clays (Nieto et al., 1996; Li et al., 1994; Livi et al., 1997; Lackschewitz et al., 2004; Giorgetti et al., 2006). In distal areas of VMS systems, the primary alteration minerals belong to the smectite group (Giorgetti et al., 2006; Lackschewitz et al., 2004) – mainly montmorillonite-beidellite for evolved rocks (e.g. dacites, Giorgetti et al., 2006) and saponite for mafic ones (basalts, Alt, 1999). Smectites evolve, depending on their original composition, to chlorite, or to illite-smectite mixed-layer clays, then illite ± chlorite and finally muscovite ± chlorite (Inoue et al., 1987; Li et al., 1994; Nieto et al., 1996; Livi et al., 1997; Lackschewitz et al., 2004). In more proximal areas, the primary minerals are illite-smectite mixed-layer clays or illite (Giorgetti et al., 2006; Lackschewitz et al., 2004).

The paragonite-muscovite system has been largely investigated, whereas it is still unclear how ambient conditions control compositions in the muscovite-celadonite system – for example total Fe content, Fe/(Fe + Mg), or Fe^{3+}/Fe^{2+} (e.g. Baldelli et al., 1989; Guidotti, 1984; Guidotti et al., 1994a; Guidotti et al., 1994b; Guidotti and Sassi, 1998; Keller et al., 2005). Although pressure is known to have an extensive effect in the Tschermak substitution – which tends to increase with it (Guidotti 1984, Guidotti et al., 1994a; Guidotti and Sassi, 2002)-, since all investigated white micas equilibrated at similarly low pressures (Tornos, 2006), the effect of this intensive parameter has not been considered. On the other hand, the behaviour of Na, K, Fe and Mg in smectite and illite is even less constrained, mainly due to the complexity of the systems and the common occurrence of mixed-layer clays (Giorgetti et al., 2006; Lackschewitz et al., 2004; Livi et al., 2008). For instance, little is known about the relationship between illite and its Na counterpart, brammallite. Further work is needed in this field as this lack of knowledge inhibits the thorough interpretation of observed white micas compositions.

5.1.1. FeO/(FeO + MgO)

White micas around the Aguas Teñidas deposit can be subdivided into two main populations based on their FeO/(FeO + MgO) composition: high (>0.45) and low (<0.45) FeO/(FeO + MgO) micas. High FeO/(FeO + MgO) micas are found in regional protoliths (field 1 in Fig. 7b), in proximal rocks surrounding the stockwork and above the massive sulphides (field 2 in Fig. 7b), and within the massive sulphides (AGI-888/162.5), and predominantly coexist with Fe and Fe-Ti oxides in the mineral assemblage. Low FeO/(FeO + MgO) micas are located in rocks in the footwall proximal or within the stockwork system (fields 3 to 5 in Fig. 7b), which present no Fe oxides in the mineral assemblage and, instead, bear rutile and sulphides. These observations suggest a relationship between FeO/(FeO + MgO) in white micas and redox conditions. Given the uncertainty in the exact genetic and temporal relationship between the mineralizing event and the oxidizing alteration that produced red rocks in the proximal hanging wall, and the exception in the general behaviour of sample AGI-888/162.5 (which is transitional between footwall and hanging wall), footwall and hanging wall rocks will be discussed separately.

The study of metapelitic rocks has revealed that Fe^{3+} and Fe^{2+} are both usually present within muscovite at variable Fe^{3+}/Fe^{2+} ratios, even in reducing rocks bearing graphite, and that in oxidising mineral assemblages there is a coupled increase in Fe^{3+}/Fe^{2+} and total Fe content in muscovite (Guidotti et al., 1994b; Guidotti and Sassi, 2002). These authors suggested that, under more oxidizing conditions, more Fe^{3+} is incorporated in addition to, not instead of, Fe^{2+}, thus resulting in an increase in total Fe without a significant change in $Fe^{2+}/(Fe^{2+}+Mg)$, which would therefore be controlled by other factors. Although differences exist between metapelitic systems and the Aguas Teñidas rocks, our observations are compatible with this behaviour and therefore we suggest that the higher FeO/(FeO + MgO) for white micas in footwall rocks outside the stockwork system was likely produced by equilibration under oxidizing conditions, with additional Fe being incorporated into white micas in the form of Fe^{3+}. Since Fe^{3+} partitions preferentially into muscovite compared to chlorite (Guidotti et al., 1994b), under oxidizing conditions FeO/(FeO + MgO) in muscovite could be expected to be higher than that in coexisting chlorite. This has been observed in all samples of rocks bearing Fe oxides or close to the transition to rutile-

bearing rocks (Fig. 13), supporting our hypothesis. Nevertheless, whether the same behaviour here described for white micas also applies to the illite system needs to be investigated, as the observed final ratios could be inherited from the precursor phase and/or be modified during transformation into white micas.

Seafloor metasomatism predominantly occurred under oxidizing conditions, as indicated by the presence of Fe oxides and the high FeO/(FeO + MgO) in muscovite in regional protoliths. This could be due to the effect of potentially oxidizing fluids during seafloor metasomatism and/or a stronger control of the initial Fe redox state in the original igneous rock (only volcanic and subvolcanic rocks have been analysed in this study). Although black shale has been reported in the IPB, particularly for VMS deposits in the southern IPB (Tornos, 2006), the absence of black shale in the sequence around the Aguas Teñidas deposit (Bobrowicz, 1995; Hidalgo et al., 2000; Conde and Tornos, 2020) could indicate oxidizing contemporary seawater (seafloor) conditions.

For rocks near the hydrothermal system, increasing influence of the reducing hydrothermal fluid, as well as of the fluid/rock ratios, would be responsible for a shift towards more reducing conditions, producing the destabilization of Fe and Fe-Ti oxides, and a decrease in the FeO/(FeO + MgO) of white micas due to a strong reduction in Fe^{3+}/Fe^{2+}. Our observations indicate that the shift to low FeO/(FeO + MgO) in white micas occurs later than the Fe oxides destabilization and disappearance, although paragonite in rutile-bearing rocks already presents lower FeO/(FeO + MgO) than in Fe oxide-bearing rocks. The main decrease in FeO/(FeO + MgO) seems to occur around the area of pyrite stabilization (e.g. AE-69/3198). This shift upon transition from oxidized to reduced conditions is strong, with FeO/(FeO + MgO) changing from values above 0.42 (zone 2 in Fig. 7b) to around and below 0.2 (zones 3 and 4). Muscovite in sample AE-69/319.8 presents intermediate compositions and can thus be considered as transitional.

In the hanging wall in core AGI-888, oxidized proximal rocks were clearly affected by hydrothermal fluids as evidenced by whole rock geochemistry and mineralogical zoning (Gisbert et al., 2021), as well as by the chemistry of white micas in them; paragonite in the most proximal samples, decreasing paragonite/muscovite with distance to ore, and finally presence of Na-rich muscovite; trace elements that can be related to hydrothermal activity (e.g. Tl, Pb) with contents decreasing with distance to ore. The temporal relationship between the mineralizing event and the oxidizing alteration, and its effect on the pre-existing mineral assemblage composition, still need to be studied in detail. However, the proximity of oxidized rocks to the replacive massive sulphides suggests that oxidation was produced by a later event that modified rocks which had potentially been reduced by upwelling hydrothermal fluids during the mineralizing event. Based on textural relationships, Tornos (2006) also suggested a younger age for the oxidizing alteration, coeval with the Variscan deformation. Since the composition of micas that formed during the initial reducing hydrothermal alteration is unknown, the origin of the current high FeO/(FeO + MgO) can only be inferred. Two main options exist: 1) original micas (and resulting white micas) had low FeO/(FeO + MgO), similar to that in reduced rocks in the footwall, and subsequent recrystallisation during the oxidizing event produced additional incorporation of Fe as Fe^{3+} causing an increase in FeO/(FeO + MgO); or 2) although formed under reducing conditions, original micas already presented high FeO/(FeO + MgO), as is the case for sample AGI-888/162.5, in which muscovite formed under reducing conditions within the massive sulphides but presents the highest measured FeO/(FeO + MgO) (ca. 0.8, Fig. 7b). The

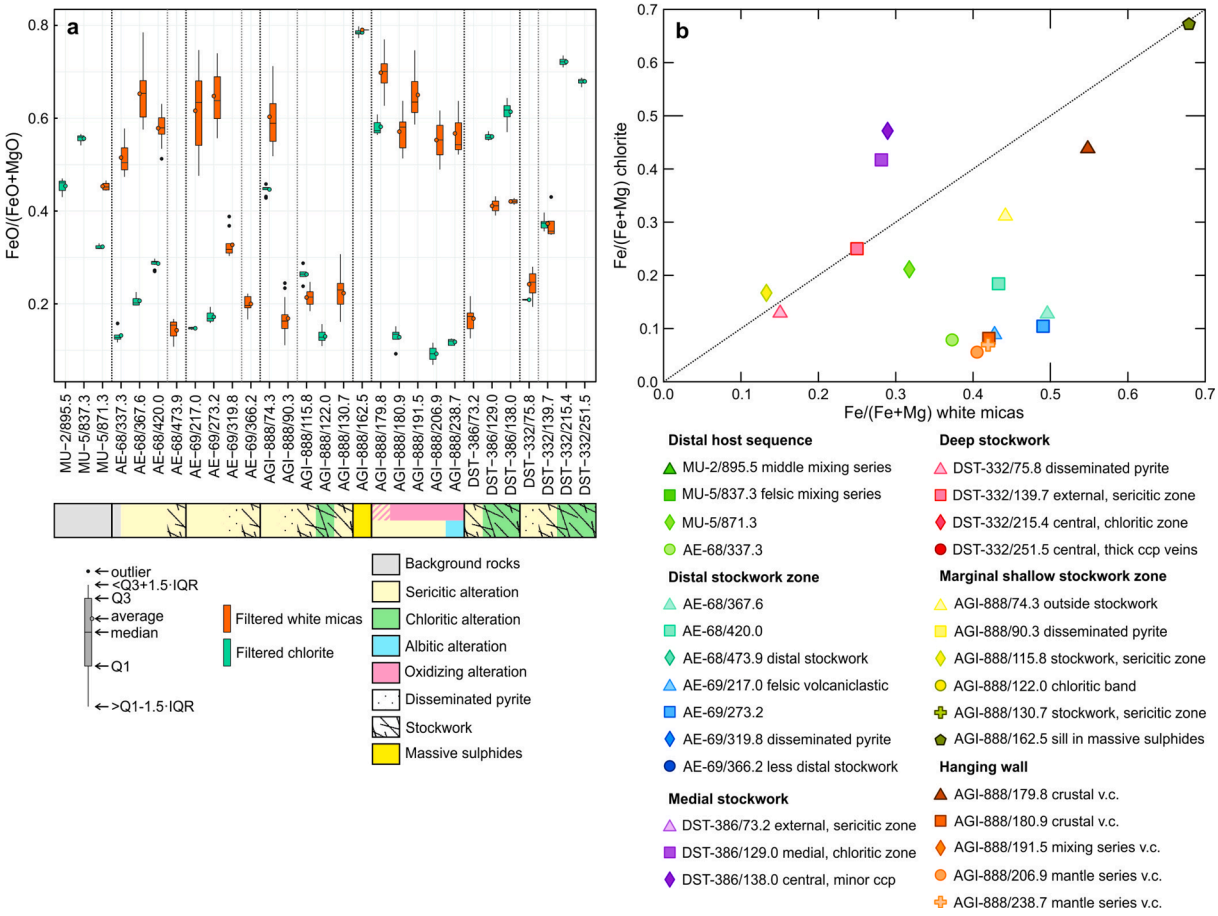

Fig. 13. Comparison between FeO/(FeO + MgO) derived from EMP data in chlorite and white micas in each sample. (a) Box and whiskers plot of FeO/(FeO + MgO). (b) Fe/(Fe + Mg) average compositions of chlorite and muscovite in each sample calculated from all available data. Q: quartile; IQR: inter-quartile range (=Q3-Q1).

high FeO/(FeO + MgO) in muscovite in sample AGI-888/162.5 may indicate formation from especially Fe-rich hydrothermal fluids which would have also reached the hanging wall of this replacive deposit, and/or formation of micas within and above the massive sulphides under particular ambient conditions, different from those in the footwall (e.g. different from those in the central deep stockwork, where Fe-rich fluid component and T should be at a maximum), supporting the second option. If this interpretation holds true, the presence of high FeO/(FeO + MgO) illite and muscovite formed under reducing conditions in the hanging wall of the massive sulphides would need to be considered, although it would not have important implications when using this ratio for vectoring purposes. On the other hand, whereas in sample AGI-888/162.5 the FeO/(FeO + MgO) ratios in muscovite and chlorite are coincident (Fig. 13), the strong difference in FeO/(FeO + MgO) ratios between these two minerals in hanging wall rocks strongly suggest mineral reequilibration during the oxidizing event, thus supporting the first option. Further work is needed to solve this problem.

Besides the main change in FeO/(FeO + MgO), minor variations occur within each of the two main groups of white micas, which need to be considered. In regional protoliths, variations are likely strongly controlled by the original rock composition and the degree of seafloor metasomatism. In footwall proximal rocks outside the stockwork, no clear trends are seen other than the decrease in the FeO/(FeO + MgO) ratio of paragonite upon disappearance of Fe oxides from the mineral assemblage. On the other hand, rocks within the hydrothermal system show a clear trend of increasing FeO/(FeO + MgO) ratio towards its centre. This can be directly related to the progressive change in physicochemical conditions towards the centre of hydrothermal system caused by increasing influence of hot Fe-rich fluids. Besides the control of FeO/(FeO + MgO) in the fluid, although little investigated, changes in T may also exert a control on the differential partition of Fe and Mg into illite as seen for muscovite, and thus on the FeO/(FeO + MgO) ratios (e.g. Guidotti, 1984; Guidotti et al., 1994a). No clear trends have been observed in muscovite composition in rocks from the hanging wall, which may be in part due to their more complex history.

Finally, the studied white micas present a nearly pure paragonitic composition for the paragonite end-member, with only a minor celadonitic component. This is consistent with the low solubility of the celadonitic component in the paragonite structure compared to muscovite (Guidotti, 1984; Keller et al., 2005). On the other hand, paragonite mostly presents markedly higher FeO/(FeO + MgO) of ca. 0.8 at lower Fe content compared to coexisting muscovite. The reason for preferential incorporation of Fe relative to Mg in paragonite is unknown, although it may be caused by structural constraints inducing different partition of these elements into the two phases.

5.1.2. $Na_2O/(Na_2O + K_2O)$

The Na and K contents and Na/K ratios in minerals of the smectite and illite (+brammallite) groups can be highly variable. However, a solvus exists in the muscovite-paragonite system (Guidotti, 1984; Guidotti et al., 1994a; Guidotti et al., 1994b; Keller et al., 2005). Thus, during transformation of smectite and illite to white micas, interstratified muscovite and paragonite may form to accommodate both Na and K (Frey, 1978; Livi et al., 2008); with further evolution, paragonite and muscovite recrystallize into discrete larger crystals (Frey, 1978; Livi et al., 2008). The maximum Na_2O content in muscovite is constrained by element availability – which may be controlled by rock and fluid compositions as well as by partition between coexisting mineral phases (e.g. muscovite, albite), phengicity, and formation conditions (e.g. P, T) (Guidotti, 1984, Guidotti et al., 1994a, b; Keller et al., 2005). Data on coexisting muscovite and paragonite in metapelitic rocks show that at low P (<8 kbar) and T (<300 °C), the muscovite-paragonite solvus is nearly vertical at the muscovite side and, hence, changes in P and T have little influence on the maximum Na content in muscovite, which is close to Na/(Na + K) = 0.1 for pure muscovite (i.e. without celadonitic component) (Guidotti et al. 1994a).

At the Aguas Teñidas deposit, high (mostly 0.05 – 0.15) $Na_2O/(Na_2O + K_2O)$ muscovite has been observed in proximal rocks in the hanging wall, and in the external zones of the stockwork and proximal rocks around it. This high $Na_2O/(Na_2O + K_2O)$ muscovite coexists with paragonite in the most proximal hanging wall, as well as outside the stockwork, beyond the area with disseminated pyrite. On the other hand, low (<0.05) $Na_2O/(Na_2O + K_2O)$ muscovite occurs in more internal parts of the feeder system and in regional protoliths. In the footwall and regional protoliths, overall white mica compositions are suggested to reflect the original Na and K compositions of precursory minerals based on the absence of evidence of major system modification during diagenesis and low-grade metamorphism. In the proximal hanging wall, where white micas may have reequilibrated and/or recrystallized during the oxidizing alteration event, we consider that, because 1) unlike FeO/(FeO + MgO), the $Na_2O/(Na_2O + K_2O)$ ratio is not significantly affected by Fe^{3+}/Fe^{2+}; and 2) trends in the abundance of paragonite and in the $Na_2O/(Na_2O + K_2O)$ ratio in muscovite follow those expected for VMS deposits and mimic those observed in the footwall; $Na_2O/(Na_2O + K_2O)$ ratios are likely mostly similar to those present prior to the oxidising event. Nevertheless, micas from the footwall and hanging wall are discussed separately.

Low $Na_2O/(Na_2O + K_2O)$ ratios in muscovite in the central part of the hydrothermal system reflect physicochemical conditions which inhibit Na partition into illite ± brammallite, thus favouring its leaching from this zone (where there are no other Na-bearing phases) towards more external ones as shown by whole-rock geochemistry data (Gisbert et al., 2021). Higher $Na_2O/(Na_2O + K_2O)$ ratios in muscovite in the external parts of the hydrothermal system likely reflect a change in conditions which favour Na partition into illite ± brammallite, and thus its enrichment relative to K in this area. These conditions may include higher $Na_2O/(Na_2O + K_2O)$ in the fluid due to preferential partitioning of K into illite in more internal areas. Beyond the margin of the stockwork system in the footwall, high Na partitioning into the illite and illite-smecite alteration assemblage results in the formation of paragonite in addition to high $Na_2O/(Na_2O + K_2O)$ muscovite during mineral maturation.

The poor negative correlation of Fe + Mg contents (as a proxy for phengicity) with Na/(Na + K) (Fig. 14) indicates that, as suggested by Guidotti (1984), Guidotti et al. (1994a,b) and Keller et al. (2005), phengicity plays a role in controlling Na solubility in muscovite; this poor correlation may be due to the presence of Fe^{3+}. For instance, in the proximal footwall, variations in phengicity can explain the different trends observed for the shallow stockwork compared to the deep and distal one in the $Na_2O/(Na_2O + K_2O)$ vs. FeO/(FeO + MgO) diagrams (Fig. 7). In all cases, an increase in FeO/(FeO + MgO) is seen towards the centre of the system. However, in the deep (DST-332) and distal (AE-69) stockwork this is coupled with a decrease in $Na_2O/(Na_2O + K_2O)$ related to increasing phengicity, whereas in the shallow stockwork (AGI-888) an increase in $Na_2O/(Na_2O + K_2O)$ is associated with decreasing phengicity (Fig. 14). Regarding the origin of the differing phengicity trends, several physicochemical factors exist that can have an effect on the extent of Thschermak substitution; thus, different conditions in the shallow stockwork compared to other parts of the system may result in the observed diverging trends. To give an example, increasing pH has been proposed to increase phengicity at low temperatures (sub-amphibolite facies) (Wang et al., 2017). Whether these variations in phengicity are inherited from precursory phases or produced during their evolution to white micas needs to be investigated. Finally, the occurrence of different Na/(Na + K) ratios at the same Fe + Mg in the reduced part of the system (e.g. DST-332/139.7 vs DST-332/75.8) are evidence of the participation of additional controlling factors other than phengicity on the $Na_2O/(Na_2O + K_2O)$ ratios in white micas.

In the hanging wall, the paragonite/muscovite content ratio in white micas is the highest in the most proximal rocks, decreasing with distance to the massive sulphides. Disappearance of paragonite in sample AGI-888/206.9 indicates that muscovite does not reach the paragonite

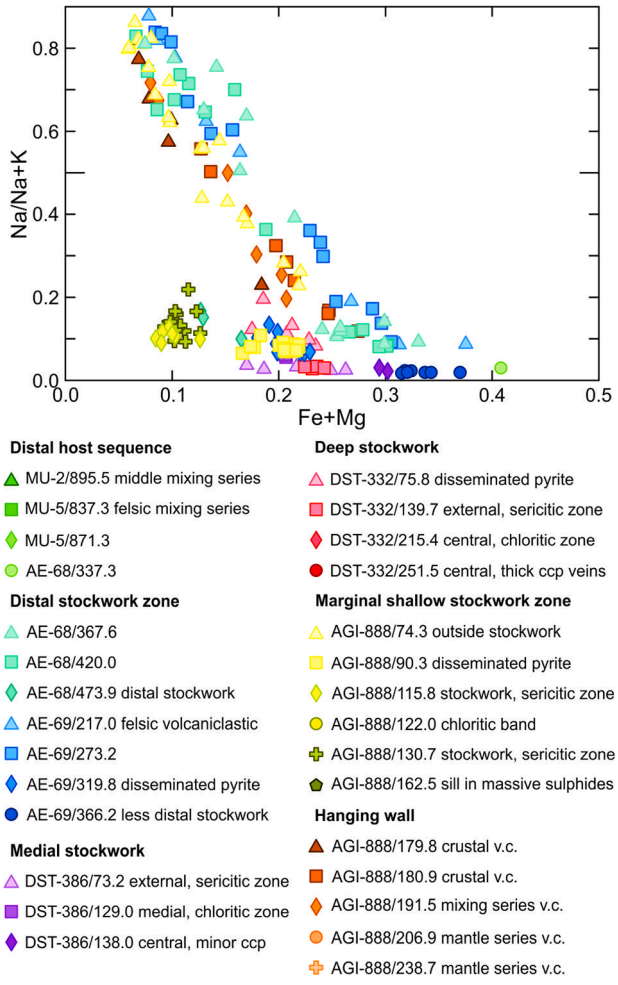

Fig. 14. Atomic Na/(Na + K) vs. Fe + Mg (as a proxy for phengicity) diagram of white micas. EMP data. Cations calculated for 11 O with all Fe as Fe^{2+}. Units are atoms per formula unit.

solvus at this distance from the ore, maybe in part due to minor albite occurrence. In AGI-888/238.7, widespread hydrothermal albite could host much of the Na in the rock. Changing fluid composition and ambient conditions necessarily play a role in the onset of albite formation at a certain distance above the massive sulphides (e.g. an increase in $a(Na^+)/a(H^+)$; Saccocia and Seyfried, 1994). Muscovite in both AGI-888/206.9 and AGI-888/238.7 still presents higher $Na_2O/(Na_2O + K_2O)$ than distal muscovite, thus evidencing the influence of the hydrothermal system beyond this distance. The Na/(Na + K) ratio of muscovite in the sill within the massive sulphides (AGI-888/162.5) is above the maximum proposed by Guidotti et al. (1994a) for metapelitic rocks, thus indicating the coexistence of muscovite and paragonite also in this part of the system.

The transition from paragonite-bearing rocks to regional protoliths has not been observed in the footwall. However, if a behaviour similar to that seen in the hanging wall is assumed, the expected transition towards more distal locations should be: 1) paragonite disappearance, with white mica consisting of high $Na_2O/(Na_2O + K_2O)$ muscovite; followed by 2) a decrease in $Na_2O/(Na_2O + K_2O)$ in muscovite towards background values. In distal muscovite (MU-2, MU-5), high phengicity and its coexistence with albite may explain the low Na contents in this phase.

Regarding textural features, separate muscovite and paragonite laminae can be seen in the hanging wall samples under SEM observation. In contrast, in paragonite-bearing rocks from the massive sulphides and footwall, white micas are seen as homogeneous phases under the SEM. Extremely fine intergrowths are known to occur in metamorphic assemblages, which require TEM for its observation (e.g. Feenstra, 1996). This suggests that hanging wall rocks underwent further recrystallization compared to footwall rocks, likely related to the oxidizing event, as has been proposed in our examination of FeO/(FeO + MgO).

The small grain size of interleaved paragonite and muscovite in the proximal hanging wall, which has resulted in mixed EMP analyses, the high celadonitic component in muscovite, and their formation under conditions below the calibration range of muscovite-paragonite pairs geothermometres like those of Guidotti et al. (1994a) and Keller et al. (2005), have precluded the use of these tools for the investigation of T conditions under which the studied muscovite formed.

5.2. *Major elements in chlorite*

In ancient VMS systems, chlorite can be a primary alteration phase in proximal zones as well as forming from the transformation of smectite group minerals in external zones (Giorgetti et al., 2006; Lackschewitz et al., 2004, Relvas et al., 2006)). The chlorite system has been extensively investigated for its use as geothermometer, which has revealed that Tschermak substitution and Fe/(Fe + Mg) in chlorite tends to increase with temperature, while vacancies in octahedral positions decrease (Walshe and Solomon 1981; Walshe, 1986; Cathelineau, 1988; Bourdelle et al., 2013; Lanari et al., 2014; Bourdelle and Cathelineau, 2015; Vidal et al., 2016). The role, controls, and effects of Fe^{3+} content in chlorite are less well established compared to white micas, although the study of diagenetic and metamorphic rocks has shown that XFe^{3+} in chlorite depends on temperature and oxygen fugacity, which is controlled by a buffering assemblage (i.e. bulk-rock composition) (Lanari et al., 2014).

The markedly different trends shown by distal and proximal chlorites in the Al vs. Fe/(Fe + Mg) diagram (Fig. 11c) indicate that the participation of hydrothermal fluids in rock alteration has a strong effect on the final chlorite composition. This could be related to the composition of the fluid itself and/or to its thermal influence, as well as to the primary formation of chlorite or of precursory smectite. Two recent semi-empirical chlorite geothermometres (Bourdelle et al., 2013; Chl(2) of Lanari et al., 2014) have been applied to the Aguas Teñidas chlorite compositions to obtain a first approximation of temperatures in the different parts of the system. Details on the geothermometers, temperature calculations for the Aguas Teñidas deposit, and evaluation of results are provided in Supplementary Material 1.8. Calculated temperatures are provided in Supplementary material 2 and shown in Fig. 15.

In the Al^{IV} vs. Fe/(Fe + Mg) diagram (Fig. 15a) trends of chlorite composition are equivalent to those observed with total Al contents (Fig. 11). In addition, the positive correlation between Al^{IV} and Fe/(Fe + Mg) in chlorite from the hydrothermal system is more regular, with samples DST-332/215.4 and DST-332/251.5 being in the main trend. However, although minor mixed analysis with other phases has a minimal effect on the total Al budget, it may produce anomalous Si contents (e.g. higher when mixing is with quartz or muscovite) which result in modified and incorrect Al^{IV} values. Therefore, Al^{IV} can be used for vectoring purposes in substitution of total Al, but great care during data selection is required.

Although available temperature data are scarce, they are consistent, showing a temperature increase towards the centre of the system. For instance, in the distal stockwork area there is a temperature increase from sample AE-68/367.6 to AE-68/420.0, the later having a temperature similar to AGI-888/74.3, which agrees with both samples presenting muscovite with similar major element characteristics (Fig. 6). A temperature increase is also observed from the external margin of the stockwork (e.g. AGI-888/74.3, DST-332/75.8) towards its centre (e.g. DST-386/129.0 and DST-386/138.0). The highest estimated temperature corresponds to sample AGI-888/162.5, in the massive sulphides

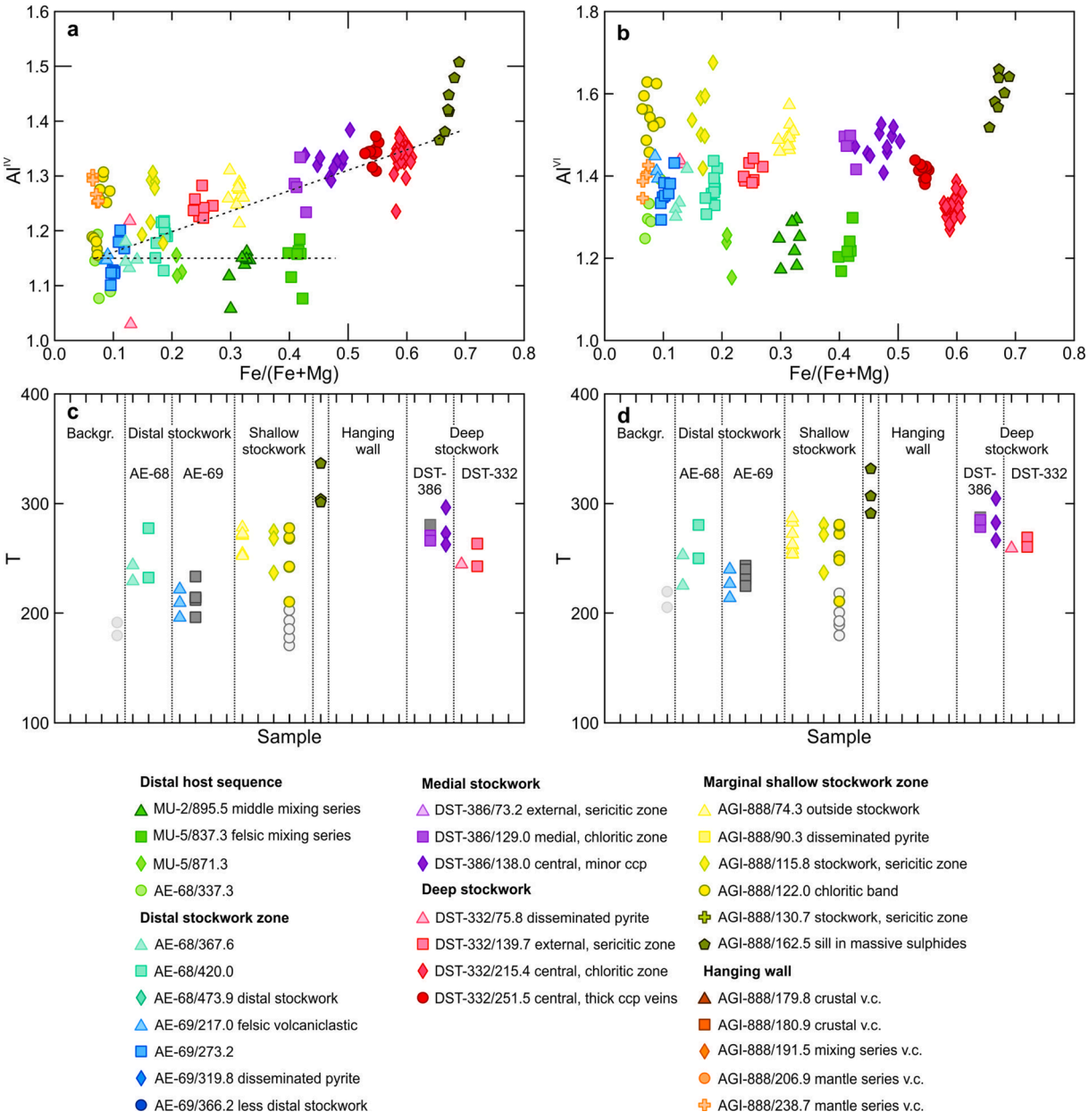

Fig. 15. Chlorite compositions derived from EMP data, and T estimated using the chlorite geothermometres of Bourdelle et al. (2013) and Lanari et al. (2014) (Chl (2)). Cations calculated for 14 O with all Fe as Fe^{2+}. Cation units are atoms per formula unit; T is in °C. (a) Al^{IV} vs. Fe/(Fe + Mg) diagram. (b) Al^{VI} vs. Fe/(Fe + Mg) diagram. (c) T estimated using Chl(2) of Lanari et al. (2014). (d) T estimated using Bourdelle et al. (2013). Symbols in grey scale in (c) and (d) correspond to temperature estimations from data showing anomalous low Al^{IV} contents, which are considered as less reliable because of the impact the distribution of Al between tetrahedral and octahedral positions has on calculated temperatures (see Supplementary Material 1.8).

zone. However, temperatures upon equilibration of rocks from which samples DST-332/215.4 and DST-332/251.5 were collected could be expected to have been higher as these were in the deep region of the central stockwork; the lack of temperature data in these samples is due to their lower vacancies in octahedral positions (Fig. 11b; Supplementary material 1.8), which support higher equilibration temperatures compared to other samples.

In distal rocks beyond the influence of the hydrothermal system (e.g. MU-2, MU-5), seawater dominates seafloor rock alteration processes and chlorite forms from precursory smectite. Three factors can be considered as the main controls of the Fe/(Fe + Mg) ratio in chlorite in this area. Firstly, interaction with cold Mg-rich seawater can be expected to lower Fe/(Fe + Mg) in whole-rock and smectite-chlorite (Fig. 11d, Fig. 16b), with the extent of any decrease depending on the degree of seafloor metasomatism. As an example, samples MU-5/837.3 and MU-5/871.3, which both had similar original felsic compositions but present different Fe/(Fe + Mg) in final chlorite and whole rock chemistries (this work, Gisbert et al., 2021). On the other hand, lower water/rock ratios compared to hydrothermal alteration (e.g. Large et al., 2001a) imply a higher initial whole-rock composition control (e.g. intermediate composition in MU-2/895.5 vs. felsic composition in MU-5/871.3). Finally, under oxidizing conditions, and due to the preferential partition of Fe^{3+} into muscovite relative to chlorite, FeO/(FeO + MgO) in chlorite can also be expected to be controlled to some extent by Fe^{3+}/Fe^{2+} and chlorite/muscovite ratios resulting from the maturation of precursory smectite, as well as by the presence of Fe oxides.

The controls on Al content in the precursory smectite are less well established than in chlorite. Thus, the interpretation of the constant Al content in chlorite in the most distal rocks is not straightforward. If the Al content is considered to be inherited from smectite, and a behaviour

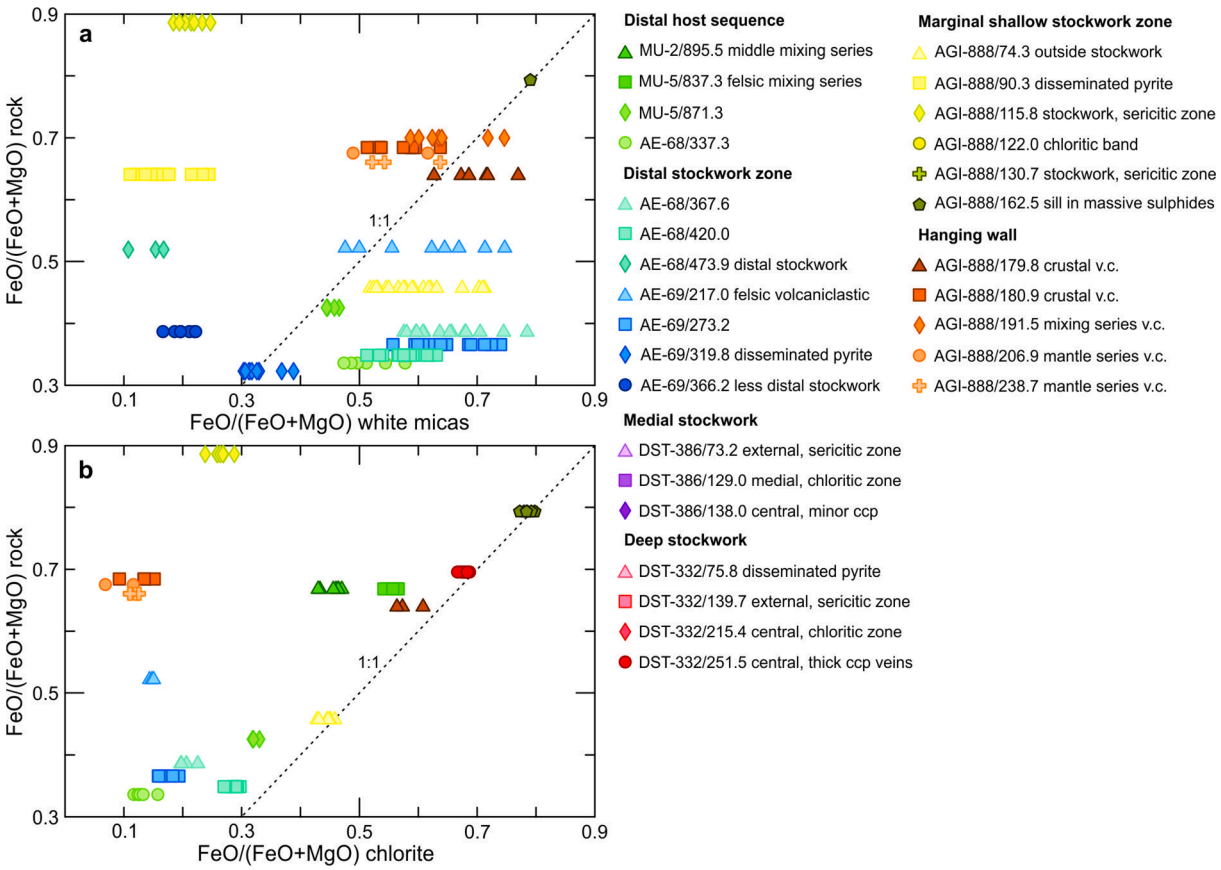

Fig. 16. Comparison between FeO/(FeO + MgO) ratios in whole rock and in white micas and chlorite. (a) FeO/(FeO + MgO) in whole rock vs. FeO/(FeO + MgO) in white micas. (b) FeO/(FeO + MgO) in whole rock vs. FeO/(FeO + MgO) in chlorite.

for smectite similar to that in chlorite is considered, Al contents could suggest that seafloor metasomatism occurred within a narrow temperature range. On the other hand, constant Al contents suggest that protolith rock compositions (e.g. felsic vs. mafic igneous rocks), did not have a significant effect on them. The characteristics of sample AE-68/337.3 will be discussed later.

In contrast to distal rocks, chlorite in proximal rocks is an original alteration mineral, and alteration is mainly controlled by the hydrothermal fluids. In addition, typically higher fluid/rock ratios result in a stronger control of hydrothermal fluid composition and associated thermal regime on final chlorite compositions. Three main groups will be discussed separately in this section based on the observation of the Al vs. Fe/(Fe + Mg) diagram (Fig. 11c): 1) regular proximal footwall rocks (all samples except for AGI-888/115.8 and AGI-888/122.0); 2) anomalous footwall rocks (samples AGI-888/115.8 and AGI-888/122.0); and 3) hanging wall rocks (only data from AGI-888/238.7 are available).

5.2.1. *Regular proximal footwall rocks*

At the centre of the hydrothermal system, chlorite equilibration at high fluid/rock ratios, with high FeO/(FeO + MgO) fluids, and at higher temperatures, should theoretically result in high FeO/(FeO + MgO), high Al^{IV} compositions with lower vacancies in octahedral positions (Bourdelle et al., 2013; Lanari et al., 2014; Bourdelle and Cathelineau, 2015; Vidal et al., 2016); progressive decrease of these parameters towards the outer region of the system should produce systematic trends towards lower Fe/(Fe + Mg) and Al^{IV} contents. This expected trend is depicted by the regular footwall chlorites in the Al^{IV} vs. Fe/(Fe + Mg) diagram in Fig. 15a. Estimated temperatures are also consistent with this model.

This trend is also present in the Al vs. Fe/(Fe + Mg) diagram (Fig. 11c), although in this case sample DST-332/215.4, and to a lower degree sample DST-332/251.5, deviate from the main trend. These deviations may reflect a higher complexity of the system, which may be caused by the variable interplay between controlling factors and result in an increase in Al^{IV} and total Al being not necessarily coupled. For instance, significantly different physicochemical conditions in the innermost part of the deep hydrothermal system where these samples were collected (e.g. higher temperature, lower $a(Al^{3+})$) could result in lower Al incorporation into chlorite, but with Al^{IV} still controlled by temperature.

Another deviation from the main trend is that of chlorite in sample AGI-888/162.5. Chlorite in this sample should have formed at lower temperatures compared to samples from the centre of the deep stockwork, but even so presents the highest measured Fe/(Fe + Mg), and a trend towards higher Al and Fe/(Fe + Mg) compositions away from the main trend. These compositions could indicate maximum influence of Fe-rich hydrothermal fluids at very high fluid/rock ratios (the sill where the sample was collected is located within the replacive massive sulphides). In this part of the system, coexisting pyrite does not seem to have a significant effect on the Fe/(Fe + Mg) in chlorite (e.g. decreased Fe/(Fe + Mg) due to Fe^{2+} partition into pyrite), which may be due to the high hydrothermal fluid supply.

Finally, sample AE-68/337.3 was classified as distal based on its muscovite characteristics. However, chlorite in this sample collected close to the first rocks with hydrothermally influenced muscovite (e.g. AE-68/367.6) presents slightly higher Al contents, as well as the lowest Fe/(Fe + Mg) amongst those rocks interpreted as distal. If the inferred correlation between Fe/(Fe + Mg) and the alteration degree in distal rocks is correct, the characteristics of this sample potentially indicate the presence, immediately beyond the area with evident chemical signs of hydrothermal alteration (e.g. high $Na_2O/(Na_2O + K_2O)$ in muscovite), of an envelope of rocks with protolith characteristics but higher

alteration degrees, possibly caused by the influence of the hydrothermal system (e.g. thermal influence, enhanced fluid circulation). The higher Al content in its chlorite may be the result of a thermal influence, and could indicate the first occurrence of "primary" chlorite, in contrast with chlorite formed from earlier smectite in more distal locations. Based on these observations, chlorite in distal rocks could be expected to approach compositions like those of sample AE-68/337.3 close to hydrothermal system, and the observed decrease in Fe/(Fe + Mg) and slight increase in Al could be the first recognizable evidence of its presence. In this scenario, chlorites could potentially record the presence of the hydrothermal system at a larger distance than muscovite (which still presents no modification from distal characteristics in sample AE-68/337.3). Additional data are needed to further confirm this hypothesis. Nevertheless, the fact that the two trends here described for chlorite compositions (proximal and distal) meet at their low Fe/(Fe + Mg) ends is indeed evidence of a progressive transition from background to hydrothermally altered rocks, and from a seawater-dominated to hydrothermal fluid dominated fluid.

5.2.2. Anomalous footwall rocks

A main deviation from the proposed model occurs in samples AGI-888/115.8 and AGI-888/122.0 (Fig. 11c, Fig. 15a). This deviation is due to the later origin (Gisbert et al., 2021) of the chlorite-rich band within the sericitic stockwork in which sample AGI-888/122.0 was collected. A detailed discussion on the characteristics of these samples and the origin of this structure is provided in Supplementary material 1.9. Nevertheless, the existence of this deviation stresses the importance of identifying and characterizing processes and structures occurred and formed at different stages within the area of the ore deposit when using vectors to ore.

5.2.3. Hanging wall rocks

In the hanging wall, a transition in chlorite compositions from signatures similar to that in sample AGI-888/162.5 to those in regional protoliths (likely along a trend similar to that depicted by footwall rocks) would be expected. Unfortunately, reliable data from hanging wall chlorites have only been obtained for one sample (AGI-888/238.7). In addition, in our discussion on muscovite compositions we argue that hanging wall samples reequilibrated under oxidizing conditions after the initial hydrothermal alteration. During this later alteration, preferential partition of Fe^{3+} into muscovite, and the appearance of Fe oxides in the mineral assemblage, likely caused a shift in chlorite composition towards lower Fe/(Fe + Mg). Thus, the current chlorite compositions in this part of the system cannot be used to extract information on its original configuration. The very low Fe/(Fe + Mg) in chlorite from sample AGI-888/238.7 suggests that the oxidation event was likely controlled by a Mg-rich fluid. Tornos (2006) describes rocks within this oxidized zone as showing evidence of *syn*-deformational oxidation, which is interpreted as suggesting that the oxidized fluids percolated along these structures during the Variscan orogeny and, thus, that at least part of this hanging wall oxidation was tectonically related. In such a case, Mg-rich fluids would be metamorphic fluids. As in sample AGI-888/122.0, the occurrence of chlorite in sample AGI-888/238.7 away from the correlation trend between F and Fe/(Fe + Mg) (Fig. 11f) also supports the different controls of the composition of this chlorite compared to initial background and hydrothermal one. However, although chlorite in samples AGI-888/122.0 and AGI-888/238.7 departs from the main F and Fe/(Fe + Mg) trend in a similar fashion, fluids involved in their formation were clearly different: reducing for AGI-888/122.0, and oxidizing for AGI-888/238.7.

5.3. Major elements in carbonate

The chemical compositions of carbonates in the Aguas Teñidas deposit are equivalent to those seen in other VMS districts (e.g. Large et al., 2001a and references therein), with an increase in Fe content towards the centre of the hydrothermal system. The low Fe content in dolomite from sample AGI-888/122.0 is consistent with other whole-rock (Gisbert et al. 2021) and mineral chemistry data for this sample, further supporting a separate origin for this chlorite band within the sericitic stockwork.

5.4. Simplified model for controls of white mica and chlorite compositions

Based on the previous discussions, a simplified model is proposed which explains the trends observed in white micas and chlorite major element chemistry (Fig. 17). Upwelling hot, reducing, Fe-rich, hydrothermal fluids react with host rocks producing a series of progressive mineralogical and mineral chemistry changes in response to variations in physicochemical conditions. Increasing hydrothermal fluid/rock ratios towards the centre of the feeding system result in an increase in T and fluid Fe/(Fe + Mg), and a decrease in fO_2.

In distal regional protoliths (zone 1 in Fig. 17), muscovite and chlorite compositions are controlled (through their mineral precursors) by initial whole rock compositions and the degree of seafloor metasomatism. In this oxidizing environment with high Fe^{3+}/Fe^{2+}, preferential partition of Fe^{3+} into muscovite results in higher Fe/(Fe + Mg) ratios in this phase compared to chlorite. The observed ratios may be inherited from illite and smectite, or produced during transformation into muscovite and chlorite.

We suggest that the first observable effect of the hydrothermal system when approaching it is an increase in T, and maybe also in fluid circulation, which results in an aureole of enhanced seafloor-like alteration (zone 2 in Fig. 17). Whereas no change in muscovite composition is detected in this zone, chlorite presents lower Fe/(Fe + Mg) produced by the increased effect of seawater into its composition, as well as slightly higher Al. The increased Al content could be due to the higher temperature and/or to direct formation of chlorite instead of through smectite transformation, and spatially represents the first detectable mineral chemistry change associated to the influence of the hydrothermal system.

Increasing fluid/rock ratios produce then the first detectable change in muscovite composition, with an increase in its Na content that marks the beginning of a Na-rich zone around the system (3). This is followed by the appearance of paragonite in the mineral assemblage in combined muscovite-paragonite crystals. The appearance of paragonite is due to the increased Na content in precursory minerals (illite or illite–smectite mixed-layer clays) surpassing the paragonite solubility in muscovite (4).

Decreasing fO_2 produces, within the paragonite-bearing zone, the destabilization of Fe- and Fe-Ti oxides (5); Fe migrates into silicate phases, whereas Ti crystallizes as rutile. Whether rutile forms directly or is preceded by an earlier phase such as anatase (e.g. Post and Burnham, 1986; Giorgetti et al., 2006), requires further investigation. Fe/(Fe + Mg) ratios in white micas are still high after the disappearance of Fe oxides likely due to sufficient Fe^{3+}/Fe^{2+} ratios, although paragonite presents lower Fe/(Fe + Mg) ratios compared to that in the Fe oxide-bearing zone (6). Only after an additional reduction of the system, lower Fe^{3+}/Fe^{2+} ratios result in lower Fe/(Fe + Mg) muscovite, whose appearance seems to be coupled with the stabilization of pyrite (8). The decrease in Fe/(Fe + Mg) in muscovite seems to be also coupled with the disappearance of paragonite from the mineral assemblage, indicating lower Na contents in the original illite and illite–smectite (7).

Around the zone of Fe oxide destabilization, chlorite presents a significant change in its composition. $Aluminum^{IV}$ and Fe/(Fe + Mg) begin to increase controlled by the rising T and fluid Fe/(Fe + Mg). Once Al^{IV} and Fe/(Fe + Mg) in chlorite start to increase, they do so consistently towards the centre of the feeder system.

With higher fluid/rock ratios, disseminated pyrite transitions into a stockwork system (10). Within it, partitioning of Na into illite is reduced, producing the formation of low-Na muscovite. The decrease in Na/(Na + K) in muscovite seems to be coupled with the growth of ore sulphides (e.g. sphalerite, galena) in stockwork veins, and marks the end of the

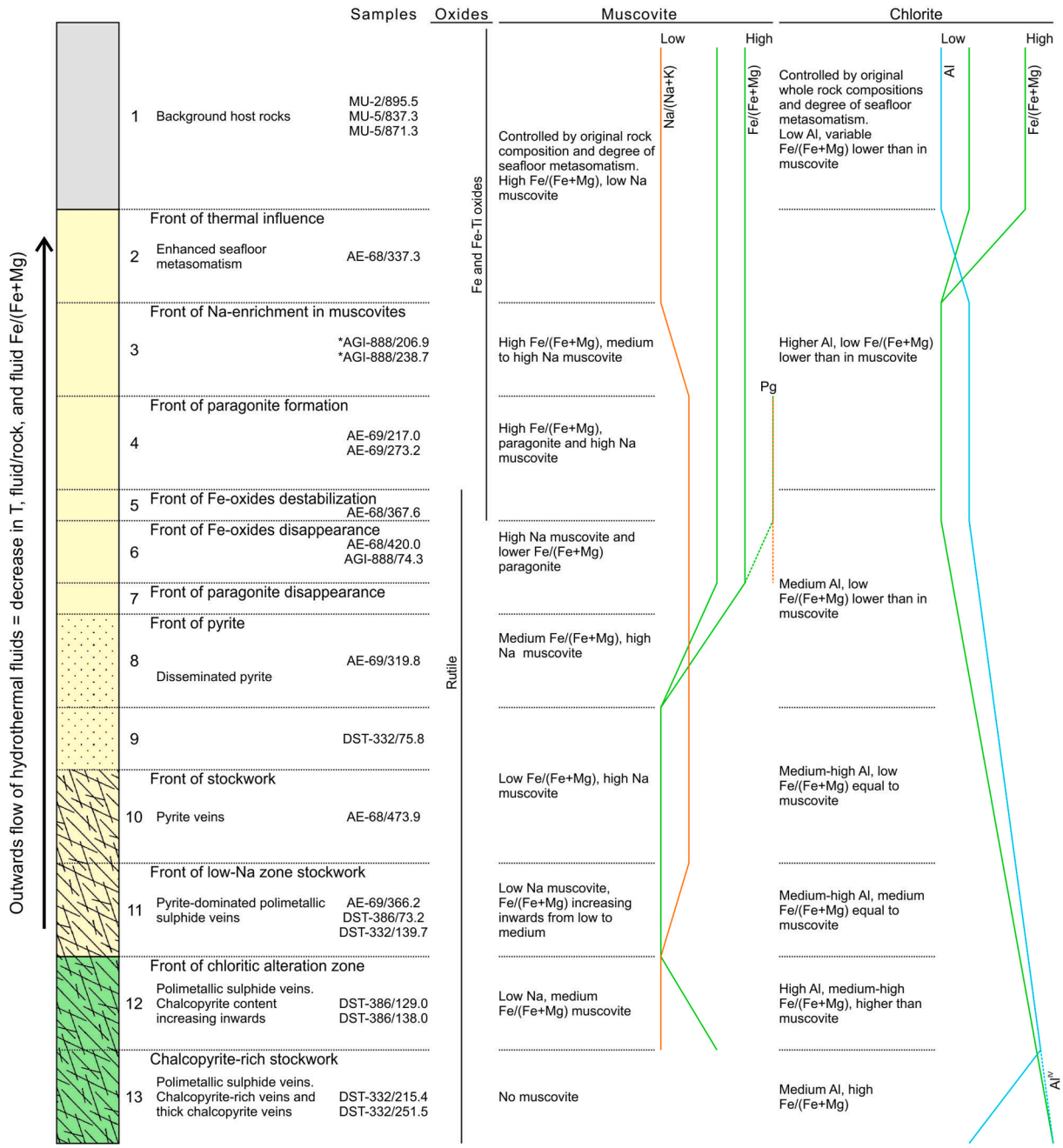

Fig. 17. Schematic diagram of the proposed model on the evolution and controls of major element vectors to ore in white micas and chlorite. Not to scale.

high-Na muscovite halo around the hydrothermal system (11). At this point a difference exists in muscovite between the shallow stockwork and the rest of the system. In all areas, Fe/(Fe + Mg) ratios increase towards the centre of the system. However, in the shallow stockwork, Na/(Na + K) increases towards the massive sulphides associated with a decrease in Tschermak substitution, whereas the opposite is observed in other parts of the system when approaching its centre. This may be due to minor changes in the evolution of physicochemical conditions at different zones of the hydrothermal system. In the sericitic stockwork, Fe/(Fe + Mg) ratios in muscovite and chlorite are similar.

Towards more internal areas of the stockwork, chlorite replaces muscovite as the dominant alteration mineral (12). This is likely due to increasing T as well as Fe and Mg activities, and/or to decreasing a_{H}^{+} (Saccocia and Seyfried, 1994; Lentz et al., 1997). Coupled with the transition from sericitic to chloritic stockwork, there is a marked increase in Fe/(Fe + Mg) ratios in muscovite, as well as in the sulphide content in the rock. Regarding chlorite, its Fe/(Fe + Mg) ratios increase above those of muscovite. Finally, in the innermost part of the system, which is characterized by large amounts of chalcopyrite in the stockwork veins, muscovite is not present in the mineral assemblage and chlorite presents high Fe/(Fe + Mg) ratios, with coupled high Al^{IV} contents but lower total Al compared to more external areas.

Variations in the order of phase and chemistry changes described here may occur. Indeed, further work is needed to investigate the exact genetic and distance relationship between the destabilization of Fe oxides, the disappearance of paragonite, the transition to lower Fe/(Fe + Mg) in muscovite, and the stabilization of pyrite. For example, whereas the decrease in Fe/(Fe + Mg) in muscovite is mainly controlled by redox conditions, the reduction of Na contents in original alteration minerals leading to the disappearance of paragonite from the mineral assemblage is likely also controlled by other factors. Therefore, these two main changes in white mica compositions could be spatially decoupled. As a

consequence, at different locations (e.g. deep vs. shallow areas) minor changes in the evolution of physicochemical conditions along the hydrothermal system could result in these transitions being located at different distances, and maybe in different order. Also, redox conditions seem to be the main control of the destabilization of Fe oxides, the transition from high to low Fe/(Fe + Mg) muscovite, and the formation of pyrite, whereas Fe/(Fe + Mg) (and Al content) in chlorite seems to be predominantly controlled by temperature, fluid Fe/(Fe + Mg) and fluid/rock ratio. Therefore, the formation of pyrite and the transition from high to low Fe/(Fe + Mg) muscovite on one hand, and the increase in Fe/(Fe + Mg) and Al in chlorite on the other, although likely close in space, may not be necessarily coupled. For instance, in sample AGI-888/74.3, which was collected outside the shallow stockwork in the zone presenting high Fe/(Fe + Mg) muscovite and decreased Fe/(Fe + Mg) paragonite, Fe/(Fe + Mg) in chlorite is higher than in sample DST-332/139.7, which was collected within the external part of the deep stockwork and bears low Fe/(Fe + Mg) muscovite, but reached a lower temperature according to the geothermometric models used in this study.

The model presented herein is based on the circulation of hydrothermal fluids through a host rock of homogeneous initial composition (URD), and on the assumption that temperature, fO_2 and Fe/(Fe + Mg) are coupled with fluid/rock ratios. However, changes in the location and order of the described fronts could occur related to shifts from these conditions. For example, the described decoupling between Fe/(Fe + Mg) changes in muscovite and chlorite due to different temperature gradients in the shallow and deep stockwork. Lithological changes could also potentially introduce significant modifications (e.g. in the fO_2 upon crossing a black shale layer, which would strongly change the relationship between T and fO_2 described at the Aguas Teñidas deposit). Finally, this model is not applicable to the hanging wall to the Aguas Teñidas deposit, which was modified after the main hydrothermal event.

5.5. Trace elements

Among trace elements that can be hosted in white micas and chlorite, fluid-mobile elements (Ag, Cd, Au, Hg, Ga, In, Sn, Tl, Bi, Pb, Ge, As, Sb, Te, Se) are particularly important as they are usually carried by hydrothermal fluids responsible for the formation of Fe-, Cu-, Zn-, and Pb-sulphides and sulphosalts in VMS deposits. Trends in the concentrations of these elements thus represent important exploration tools. However, several factors may control the contents of these elements other than distance to ore and associated changes in physicochemical conditions, which need to be considered. These are, among others: 1) diversity of allocation within the studied mineral phases; 2) differential partition into coexisting mineral phases; or 3) recrystallization and reequilibration during subsequent diagenesis and metamorphism.

5.5.1. Element allocation

Trace elements can occur as structural element substitutions, interlayer occupancy, or micro- to nano-inclusions (e.g. Soltani Dehnavi et al., 2018a; Soltani Dehnavi et al., 2018b; Soltani Dehnavi et al., 2019). Element correlations and time-resolved LA-ICP-MS profiles can be used to investigate the allocation of each element (e.g. Soltani Dehnavi et al., 2018a; Wilkinson et al., 2015). This diversity of possible locations has important analytical implications. For instance, the occurrence of micro-inclusions may produce variable data bias depending on the degree of resulting analytical mixture. On the other hand, substitution relationships may also have a strong impact. In white micas, variations in Na/(Na + K) affect Rb and Sr contents as these elements substitute K and Na, respectively. Location of trace elements in the studied white micas and chlorite is discussed in Supplementary Material 1.10.

5.5.2. Differential partition

In the Bathurst Mining Camp, white micas bear higher concentrations of Tl, Sn, Hg, In, and Ba, whereas sulphide minerals are the primary host for Bi, As, Sb, Se, Cd, Pb, Ni, Cu, and Co; chlorite, and to a lesser degree white micas, are enriched in Zn relative to pyrite and pyrrhotite in the host rocks (Soltani Dehnavi et al., 2018a; Soltani Dehnavi et al., 2019). At the Aguas Teñidas deposit, white micas are the main host of Sb in silicates, and present larger concentrations of Cs, Sn and Tl compared to coexisting chlorite. On the other hand, chlorite presents higher concentrations in As, Co, Li and Zn compared to coexisting white micas. A preliminary analysis of pyrite and chalcopyrite at the Aguas Teñidas deposit has revealed partitioning of As, Pb and Sb into pyrite, and of In, Bi, Hg, Sb, Se, Sn and Zn (lower than in chlorite) into chalcopyrite, which is consistent with observations in the Bathurst Mining Camp. Thallium contents in sulphides could not be quantified; however pyrite characterization by LA-ICP-MS analysis in ancient (e.g. Bracemac-McLeod Deposits, Abitibi, Canada, Genna and Gaboury, 2015) and active (e.g. TAG mounds, Mid-Atlantic Ridge, Grant et al., 2018) deposits shows that this mineral can host significant amounts of Tl (up to >200 ppm). Even within a single group like white micas differential partition may have a strong impact; for instance, Tl, V, Li and Pb preferentially partition into either muscovite or paragonite and, therefore, the presence or absence of paragonite in the mineral assemblage may have a strong impact on the measured contents. In addition, measured contents may show significant variability within a single sample depending on the degree of analytical mixture obtained during the analysis of finely interleaved muscovite-paragonite. Therefore, element concentrations in a given mineral phase may be controlled by coexisting phases, which may disturb the observed chemical trends by seizing certain trace elements.

5.5.3. Diagenesis and metamorphism

Trace element concentrations can be affected by diagenesis and metamorphism due to 1) different partition of trace elements into white micas and chlorites during smectite transformation; 2) mineral re-equilibration at different P-T conditions; 3) recrystallization, which may refine the mineral chemistry, expelling trace elements from the structure into exsolved inclusions or even out of the crystal (Large et al., 2014; Soltani Dehnavi et al., 2018b). The preservation of chemical trends consistent with a hydrothermal origin around the Aguas Teñidas deposit indicates that diagenesis and low grade metamorphism in the prehnite-pumpellyite facies did not induce any significant modification into the trace element contents in white micas and chlorites. Metamorphism at higher grade greenschist facies conditions endured in the Bathurst Mining Camp neither produced major effect (Soltani Dehnavi et al., 2018a). Therefore, we conclude that the original chemical trends produced during the hydrothermal event that formed the Aguas Teñidas deposit are mostly preserved and are those that have been characterized here.

Several different trends have been observed for trace elements at the Aguas Teñidas deposit. Tin and Co present the highest concentrations at the centre of feeder system, which indicates supply by the hydrothermal fluids and their preferential partition into the solid phases upon changing conditions. On the other hand, elements such as Cs, Li and Tl show low concentrations (below those of regional protoliths) at the core of the stockwork system, an increase towards its margin, and a subsequent outwards decrease towards background concentrations. These trends mimic those of whole rock compositions (Gisbert et al., 2021), and indicate high solubilities in the zones of high fluid/rock ratios and temperature. This results in leaching of these elements towards external areas of the system, where fluid/rock reaction and/or a change in temperature produce their partition into the solid phases generating a halo/shoulder of high concentrations. The shoulder occurs at different distances along the system depending on the element. This type of concentration pattern has been described in VMS and other hydrothermal deposits (e.g. Cu–Au porphyries, Wilkinson et al. 2015). Zn likely has a similar behaviour, although its partition into sphalerite may obscure its trends.

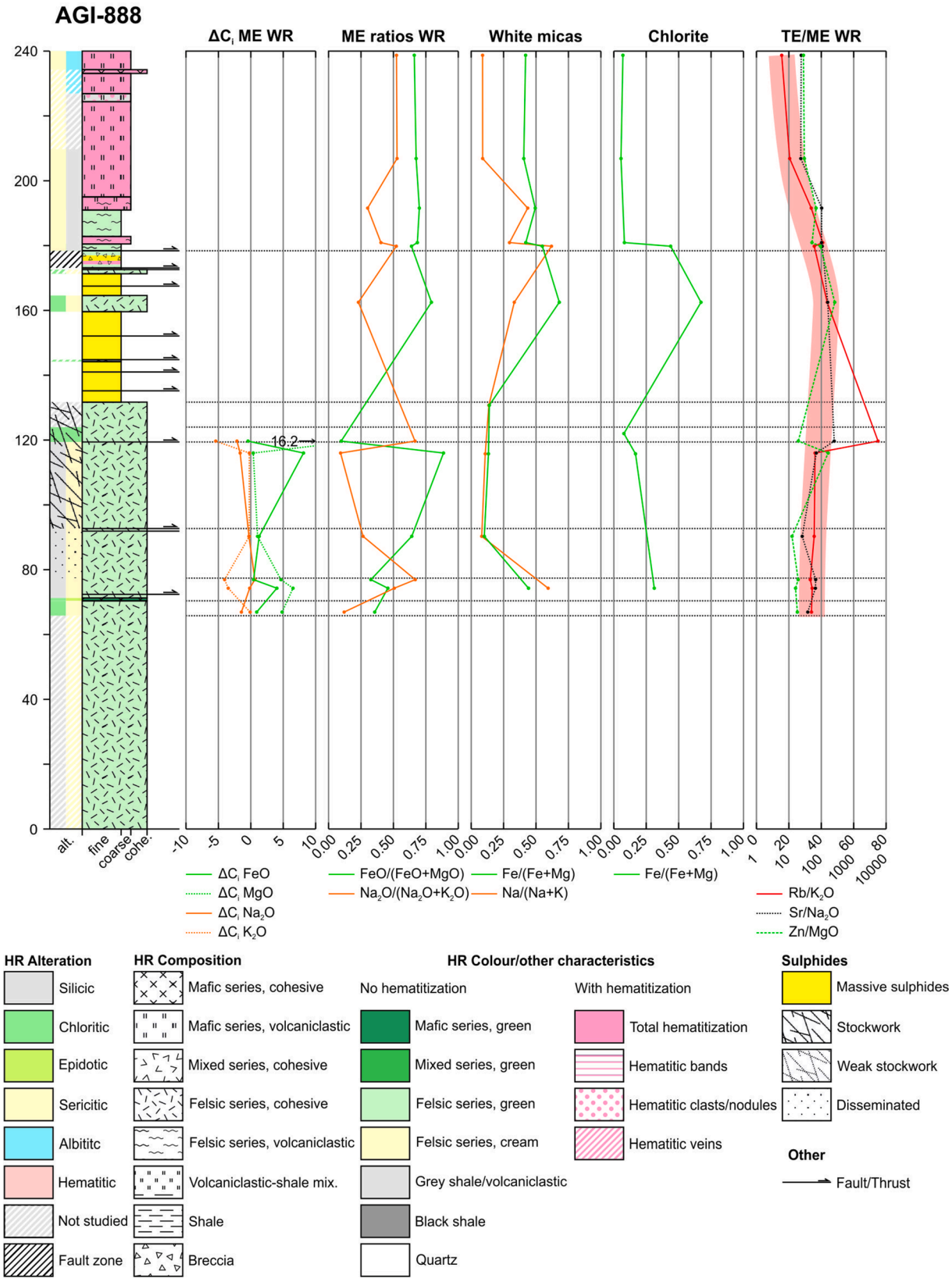

Fig. 18. Chemical profiles along selected cores (AGI-888, AE-69 and AE-68). Whole rock geochemistry data from Gisbert et al. (2021). For major element data units are wt. % for major elements and $\mu g g^{-1}$ for trace elements. Depth along the core in meters. ΔC_i values represent the absolute difference between the actual concentration of a given element in a rock, and the concentration it would have had if it had behaved as immobile; they were calculated through the isocon method. Major element ratios in white micas and chlorite are derived from EMP data. In the TE/ME WR profile, lineal units in the x-axis are for Rb/K_2O, and logarithmic ones are for Sr/Na_2O and Zn/MgO; the broad red band represents the smoothed trend of the Rb/K_2O ratio. HR: host rock; ME: major elements; TE: trace elements; WR: whole rock. (For interpretation of the references to colour in this figure legend, the reader is referred to the web version of this article.)

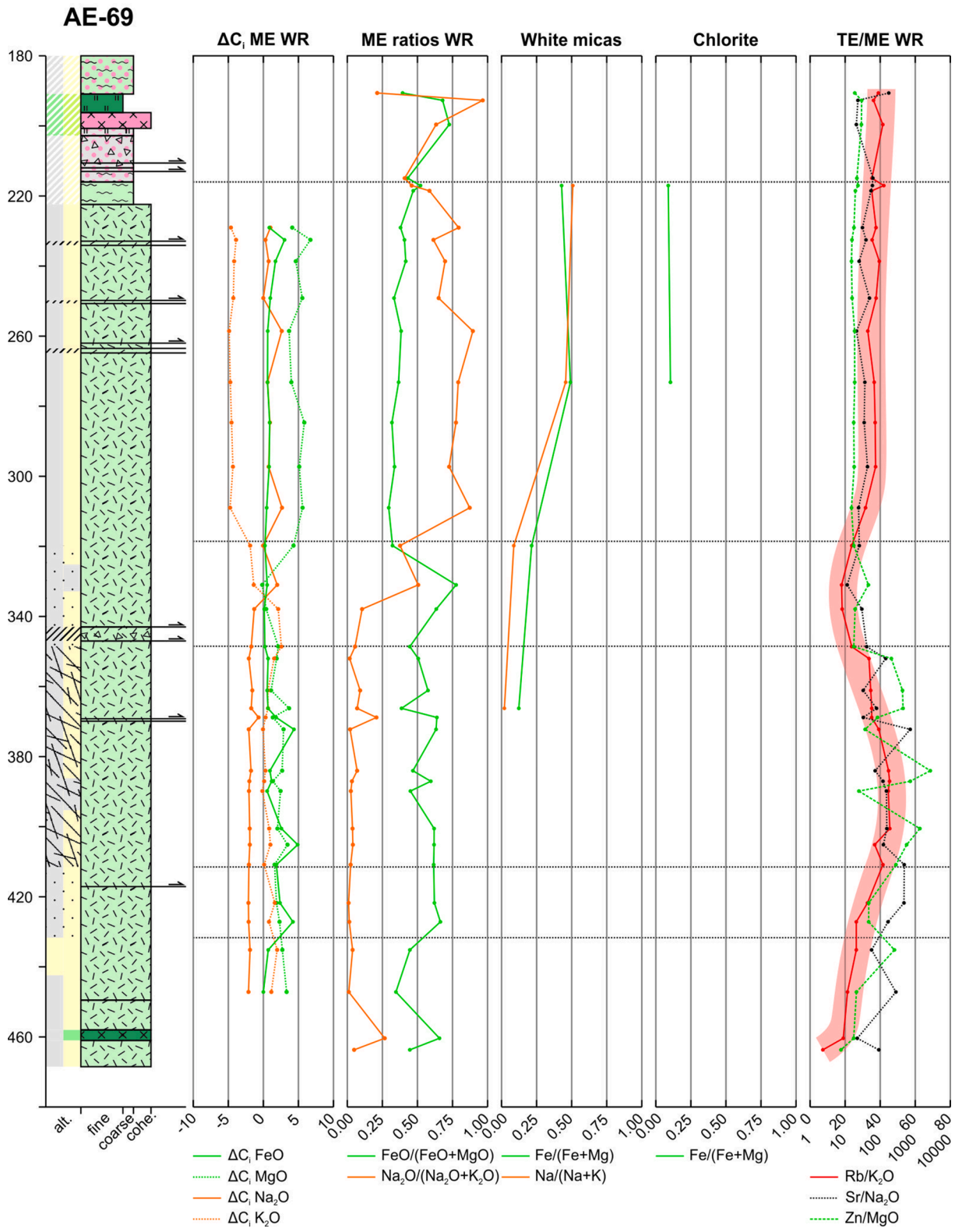

Fig. 18. (*continued*).

Pb is a common trace element in footwall white micas around the Aguas Teñidas deposit, although usually at low concentrations (<10 ppm) even in stockwork rocks. Slightly higher concentrations only occur in the paragonite-bearing zone in core AE-69. In contrast, white micas in the hanging wall present higher Pb contents up to >50 ppm. We envisage two main possible scenarios: 1) upwelling hydrothermal fluids transported Pb into the hanging wall, which became fixed in illite due to favourable physicochemical conditions including low H_2S in fluids due to prior precipitation of sulphides; and 2) upwelling of Pb-bearing hydrothermal fluids produced minor galena mineralization in the immediate hanging wall and, when subsequent oxidizing alteration occurred, Pb released from the dissolved galena became hosted in muscovite. In

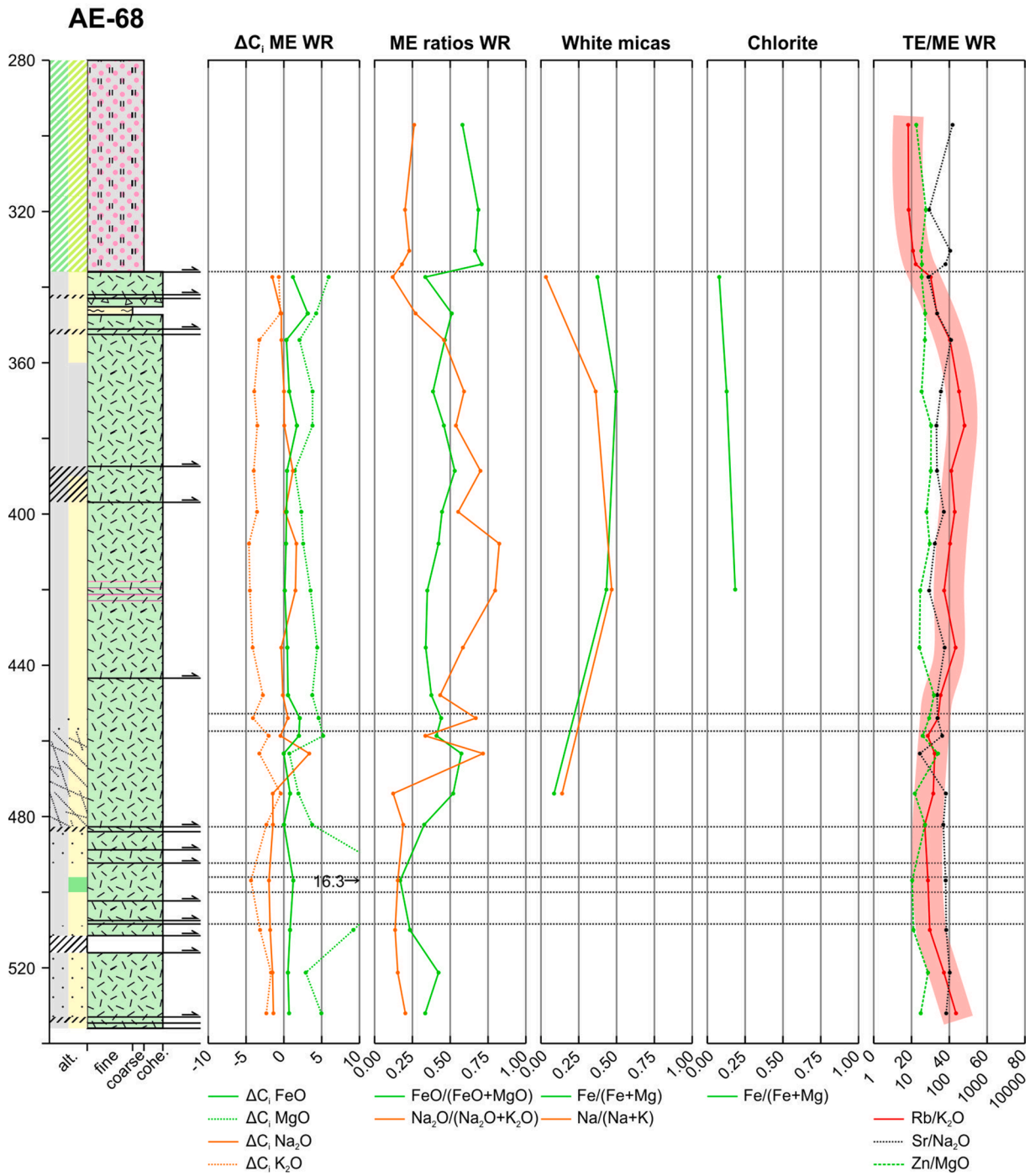

Fig. 18. (*continued*).

either case, Pb represents a powerful vector for the detection of the hanging wall of the massive sulphides, although in this particular deposit only for a short distance (<30 m). A similar mechanism can be envisaged for Zn, especially to explain higher Zn/MgO ratios in the hanging wall.

5.6. Comparison between mineral and whole rock chemistry vectors to ore at the Aguas Teñidas deposit

Rocks hosting the Aguas Teñidas deposit present systematic whole rock geochemistry trends with distance from the centre of the hydrothermal system similar to those in other VMS systems (e.g. Large et al., 2001b; Barrett et al., 2005) (Gisbert et al., 2021). There is a general whole rock Fe enrichment and alkali depletion towards the centre of the hydrothermal system, with Mg showing less systematic trends. Potassium leached from the inner portions of the system accumulated in marginal to distal locations of the stockwork producing a K-rich band. Regarding Na, even in the most distal analysed samples from the stockwork Na was still leached from the host rock and, instead, accumulated outside it. In addition, geochemically anomalous halos of base metals (Zn, Pb, Cu), volatile elements (Tl, Sb) and Ba were recognized around the Aguas Teñidas deposit. Whole rock geochemistry profiles along the studied drill cores produced in Gisbert et al. (2021) are provided in Supplementary Material 1.11 for reference. The main whole rock and mineral chemistry trends around the Aguas Teñidas deposit are compared in three cores (AGI-888, AE-69 and AE-68) in Fig. 18.

5.6.1. $Na_2O/(Na_2O + K_2O)$

A correlation is observed between Na/(Na + K) in white micas and $Na_2O/(Na_2O + K_2O)$ in whole rock in the albite-poor proximal rocks under the influence of the hydrothermal system (Fig. 18). This is due to Na and K being predominantly hosted in white micas and, thus, Na/(Na + K) ratios in white micas controlling that in the whole rock. This control results in trends of the $Na_2O/(Na_2O + K_2O)$ ratio in whole rock that were not detected in Gisbert et al. (2021) and which represent a powerful vector to ore. Indeed, in Gisbert et al. (2021), where mainly the contents of individual elements were investigated, the area beyond disseminated pyrite in cores AE-68 and AE-69 was considered to present a composition controlled by homogeneous seafloor metasomatism based on nearly constant ΔC_i values for FeO, MgO, Na_2O and K_2O (ΔC_i represents the absolute difference between the actual concentration of a given element in a rock, and the concentration it would have had if it had behaved as immobile, in wt % in this case).

Whole rock $Na_2O/(Na_2O + K_2O)$ data show a broad high $Na_2O/(Na_2O + K_2O)$ halo beyond the area with disseminated pyrite, indicating that in this zone whole rock geochemistry is still controlled by the hydrothermal system. In this high $Na_2O/(Na_2O + K_2O)$ shoulder, whole rock Na_2O shows no depletion or enrichment relative to the URD reference rock. Instead, the higher $Na_2O/(Na_2O + K_2O)$ is produced by a depletion in K_2O controlled by the composition of illite and illite-smectite equilibrated during hydrothermal alteration (Fig. 18). In core AE-68, sample AE-68/347.0 shows the transition from high $Na_2O/(Na_2O + K_2O)$ values in the halo to background ones; this transition is mainly due to an end in K_2O depletion. In AE-69, this transition occurs beyond rocks of the URD and is thus masked by rock compositional changes. Indeed, lithological changes always need to be considered, especially in the low fluid/rock ratio distal areas. From the high $Na_2O/(Na_2O + K_2O)$ shoulder along the margin of the hydrothermal system, this ratio decreases towards its centre as a result of a shift from K_2O to Na_2O depletion. This high whole rock $Na_2O/(Na_2O + K_2O)$ halo around the hydrothermal system, bearing high $Na_2O/(Na_2O + K_2O)$ muscovite and coexisting paragonite in its central area, is likely equivalent to the ultraperipheral alteration zone described by Relvas et al. (1990) in the Gaviao orebody also in the IPB.

5.6.2. $FeO/(FeO + MgO)$

FeO/(FeO + MgO) ratios in whole rock are controlled by Fe/(Fe + Mg) in muscovite and chlorite, as well as by the presence of other Fe-bearing minerals such as Fe oxides or sulphides.

In Fe-oxide bearing footwall rocks, low oxide contents result in a predominant silicate control on whole rock FeO/(FeO + MgO). In these rocks, muscovite presents higher FeO/(FeO + MgO) than whole rock due to Fe^{3+} partition (Fig. 16). Towards the centre of the system, a progressive decrease in whole rock FeO/(FeO + MgO) occurs which can be related to reduced fixation of Fe relative to Mg due to 1) the progressive disappearance of Fe oxides from the mineral assemblage under the influence of reducing hydrothermal fluids, and 2) the coupled decrease in FeO/(FeO + MgO) in muscovite. In this chlorite-poor area, FeO/(FeO + MgO) in muscovite progressively approximates that in whole rock due to decreasing Fe^{3+}/Fe^{2+}. In more internal locations, the crystallization of pyrite produces additional fixation of Fe in the rock, and therefore higher FeO/(FeO + MgO) ratios decoupled from silicates compositions; in sulphide-bearing areas, whole rock FeO/(FeO + MgO) is consistently higher than in muscovite or chlorite. Therefore, the whole rock FeO/(FeO + MgO) ratio, which was not investigated in Gisbert et al. (2021), shows consistent trends and can thus be used for vectoring purposes; from regional protoliths, this ratio shows a steady decrease towards the stockwork system, followed by a sharp increase upon appearance of sulphides.

On the other hand, in the hematitic hanging wall in core AGI-888, the high content in Fe-oxides results in higher FeO/(FeO + MgO) in whole rock than in muscovite or chlorite. Since Fe^{3+} is less mobile than Fe^{2+}, the high Fe content (and associated high FeO/(FeO + MgO)) in the proximal hanging wall ratio could be argued to be unrelated to the fluid producing the oxidizing alteration. Instead, we suggest that the Fe likely has its origin in the previous mineralizing hydrothermal event. Under the original reducing conditions, pyrite (and probably other sulphides, like galena as suggested in previous sections) could be expected to have precipitated in significant amounts in the proximal hanging wall. Upon oxidation, Fe released by the destruction of pyrite would have been then fixed in muscovite and chlorite, with excess Fe forming the observed Fe oxides.

Rb/K_2O, Sr/Na_2O and Zn/MgO in whole rock geochemistry have also been explored for vectoring properties after the observation of the equivalence of $Na_2O/(Na_2O + K_2O)$ ratios in muscovite and whole rock (Fig. 18). Whole rock Rb/K_2O and Sr/Na_2O should be controlled mainly by white micas in proximal rocks, with increasing influence of albite towards distal rocks. On the other hand, chlorite and sphalerite may also control Zn/MgO, especially in the innermost part of the hydrothermal system.

5.6.3. Rb/K_2O

In the footwall, Rb/K_2O in white micas has been seen to 1) increase from regional protoliths to the paragonite-bearing rocks surrounding the hydrothermal system, where ratios are nearly constant; 2) decrease in the disseminated pyrite zone and external parts of the stockwork; 3) increase towards the innermost parts of the sericitic stockwork; and finally 4) decrease again towards the centre of the chloritic stockwork (Fig. 10). In the hanging wall, this ratio decreases away from the massive sulphides. Equivalent trends are depicted by whole rock geochemistry (Fig. 18), which therefore can be used for vectoring purposes. In addition, this similarity in behaviour with whole rock data can also provide information on the likely evolution of the Rb/K_2O ratio in white micas in parts of the system which were not analysed by LA-ICP-MS (e.g. core AE-68).

The transition to from hydrothermally influenced to protolith whole rock Rb/K_2O compositions is seen in the uppermost URD in core AE-68, which was not studied by LA-ICP-MS (Fig. 18). A decrease from high Rb/K_2O values in paragonite-bearing samples to lower ones in the regional protolith is evident, which can be expected to also occur in muscovite mineral chemistry. Towards more internal locations, rocks in core AE-68 show a steady mild decrease in Rb/K_2O from the paragonite-bearing zone to the disseminated pyrite and stockwork, with a minimum within the stockwork. In AE-69 a similar behaviour is seen, with nearly constant to slightly decreasing Rb/K_2O within the paragonite-bearing area, a marked decrease in this ratio starting at AE-69/309.0, likely close to the last occurrence of paragonite and high-Fe/(Fe + Mg) muscovite, a minimum in Rb/K_2O within the disseminated pyrite zone around the stockwork, and a subsequent increase towards its centre (up to 45.5 ppm/wt. %). The location of the minimum in Rb/K_2O within the stockwork in AE-68, compared to within the zone of disseminated pyrite in AE-69, is consistent with the more distal location of core AE-68, as also indicated by other whole rock indicators (Gisbert et al., 2021) and mineral chemistry data (e.g. absence of low Na/(Na + K) muscovite). In core AGI-888, whole rock geochemistry shows increasing Rb/K_2O values towards the massive sulphides both in the footwall and hanging wall. No whole rock geochemistry data are available for the external parts of the chlorite stockwork; nevertheless, as expected, Rb/K_2O in DST-332/251.5 (muscovite-free) presents lower values (35). In the studied cores, the transition from the URD felsic dome to the overlying intermediate to mafic rocks does not produce a significant shift in Rb/K_2O. However, such a situation may change at other lithological contacts, which need to be considered.

5.6.4. Sr/Na_2O

Whole rock Sr/Na_2O ratio broadly follows that of white micas, except for significant differences in the hanging wall (Fig. 18). In core AGI-888, footwall rocks present constant to slightly increasing Sr/Na_2O values towards the massive sulphides, which is similar to white micas

data. In contrast, whereas hanging wall white micas also present nearly constant to only slightly decreasing Sr/Na_2O away from the massive sulphides, whole rock data show a clear decrease. We suggest that this difference in the trends depicted by white micas and whole rock may be related to the increasing abundance of albite towards the albitic alteration zone and a slightly different behaviour of Sr and Na in white micas and albite. In core AE-69, whole rock Sr/Na_2O approximates the trend observed in white micas, with nearly constant values outside the stockwork system, followed by an increase towards its centre. However, there seems to be a minor mismatch between the whole rock geochemistry trend and the location of the stockwork, as maximum Sr/Na_2O values occur near the lower sections of the stockwork and within the most proximal disseminated pyrite zone. In AE-68 no variations are evident in whole rock Sr/Na_2O, which are nearly constant across the entire studied zone. Considering the close behaviour of Sr/Na_2O in white micas and whole rock in most parts of the system, white micas may be expected to present nearly constant Sr/Na_2O values in rocks from core AE-68.

5.6.5. Zn/MgO

Whole rock Zn/MgO is strongly influenced by the presence of Zn-bearing sulphides in mineralized areas. In the footwall this results in higher values in internal parts of the stockwork system (e.g. in core AE-69), and lower more constant values in more distal positions (e.g. in core AE-69 outside the stockwork zone, and along the whole AE-68, where whole rock Zn contents are indistinguishable from regional protoliths (Gisbert et al., 2021)). In the sulphide-free hanging wall, comparatively high Zn/MgO values occur in proximal locations, with a decreasing trend away from the massive sulphides. These observations could be explained by 1) increased transport and fixation of Zn in the precursors of white micas and chlorite; and/or 2) formation of sphalerite and subsequent remobilization of Zn into phyllosilicates during the oxidizing alteration event as suggested for Pb and galena in the previous section. A slight increase in Zn/MgO is seen at the transition from the URD to the overlying more mafic rocks, stressing the possible lithological control on this ratio.

In this work, the investigation of mineral chemistry data has contributed to improve the characterization of whole rock geochemistry vectors to ore by identifying a new pathfinder and stressing the likely higher usefulness of trends of element ratios compared to those of individual elements.

5.7. Distance at which the influence of the hydrothermal system can be detected using whole rock geochemistry and mineral chemistry vectors to ore

5.7.1. Major elements

In white micas, Na/(Na + K) is an ideal vector that can detect the hydrothermal system at the greatest distances from the stockwork. In the studied footwall rocks, the transition from background to hydrothermally-controlled muscovite has been observed between samples AE-68/337.3 and AE-68/367.6. This transition can also be detected using whole rock $Na_2O/(Na_2O + K_2O)$, which further constrains its occurrence between samples AE-68/347.0 and AE-68/367.6. On the other hand, if the interpretation of the higher Al in chlorite in sample AE-68/337.3 as related to the thermal influence of the hydrothermal system is correct, chlorite in this sample already records the presence of the hydrothermal system. This implies that Al in chlorite can potentially detect its presence at greater distances than vectors related to muscovite or whole rock geochemistry. Unfortunately, available samples (no samples farther than AE-68/337.3 other than those collected in the much more distal MU-2 and MU-5) preclude establishing at what distance the transition to background chlorite compositions occurs. As a reference, sample AE-68/337.3 is located 120 m away along the core from the distal stockwork, and at 316 m from the closest massive sulphides. In the hanging wall, available samples are also insufficient to establish the location of the transition to background characteristics in both mineral and whole rock chemistry, although it likely occurs close above sample AGI-888/238.7, which currently is 66 m along core away from the top of the massive sulphides.

5.7.2. Trace elements

Trace element trends in white micas can be detected in the most distal URD sample in core AE-69, within the paragonite-bearing rocks (e.g. Li, Rb/K_2O). No trace element data are available for muscovite in core AE-68, where the transition to major elements background compositions has been observed. Nevertheless, as previously discussed, whole rock geochemistry data indicate that, at least for the Rb/K_2O ratio, the hydrothermal influence should be detected in muscovite to a distance similar to that of the Na/(Na + K) vector. We tentatively suggest that the transition to background values for other trace elements like Li probably occurs either at the transition from paragonite-bearing to high-Na muscovite zones, or at the transition from Na-rich to Na-poor muscovite, likely depending on the element. On the other hand, few available chlorite data from distal locations hamper their proper discussion. Small spot sizes and counting times were used in this study for the analysis of trace elements in minerals to avoid contamination effects due to nearby crystals or inclusions. In other study areas, if textural characteristics allow for larger spot sizes or counting times, lower detection limits and higher precisions may allow extending the distance to which highly mobile trace elements related to the hydrothermal system may be identified.

When considering single element concentrations, the distance at which the influence of the hydrothermal system can be detected in trace elements in white micas is far larger than for whole rock geochemistry. However, as shown for the Rb/K_2O ratio, using an appropriate vector, whole rock geochemistry can match mineral chemistry. Regarding the studied major/trace elements vectors, Rb/K_2O is the most useful, with Sr/Na_2O and Zn/MgO only showing a shift from background compositions at much shorter distances. Despite the lower distance at which single trace elements in whole rock geochemistry can detect the hydrothermal system compared to major elements (this work, Gisbert et al., 2021), in host sequences constituted by multiple lithologies, individual major element concentrations or elemental ratios as those described here can be strongly influenced by whole rock compositions (e.g. felsic vs. mafic rocks), and thus chemical trends related to the hydrothermal system may become obscured. In contrast, some trace elements such as Tl occur in host rocks of any composition at such low concentrations that trends induced by hydrothermal fluids can be clearly distinguished, thus becoming more powerful in lithologically complex sequences.

6. Summary and conclusions

Vectors to ore related to major and trace element mineral chemistry of white micas, chlorite and carbonates have been characterized around the Aguas Teñidas VMS deposit in the IPB. Observed major element trends in white micas and chlorite have been interpreted as controlled by the upwards and outwards flow of hot reducing Fe-rich hydrothermal fluids. Increasing hydrothermal fluid/rock ratios towards the centre of the feeder system produce a coupled increase in T and fluid Fe/(Fe + Mg), and a decrease in fO_2. Observations are summarized in Fig. 19.

White micas are dominated by muscovite compositions, with coexisting paragonite in an aureole beyond the first disseminated pyrite. Systematic variations have been observed in FeO/(FeO + MgO) and $Na_2O/(Na_2O + K_2O)$. As a general trend, from distal rocks towards the centre of the hydrothermal system in the footwall, white micas show:

- High FeO/(FeO + MgO) (>0.42) and low $Na_2O/(Na_2O + K_2O)$ (<0.05) in regional protoliths.

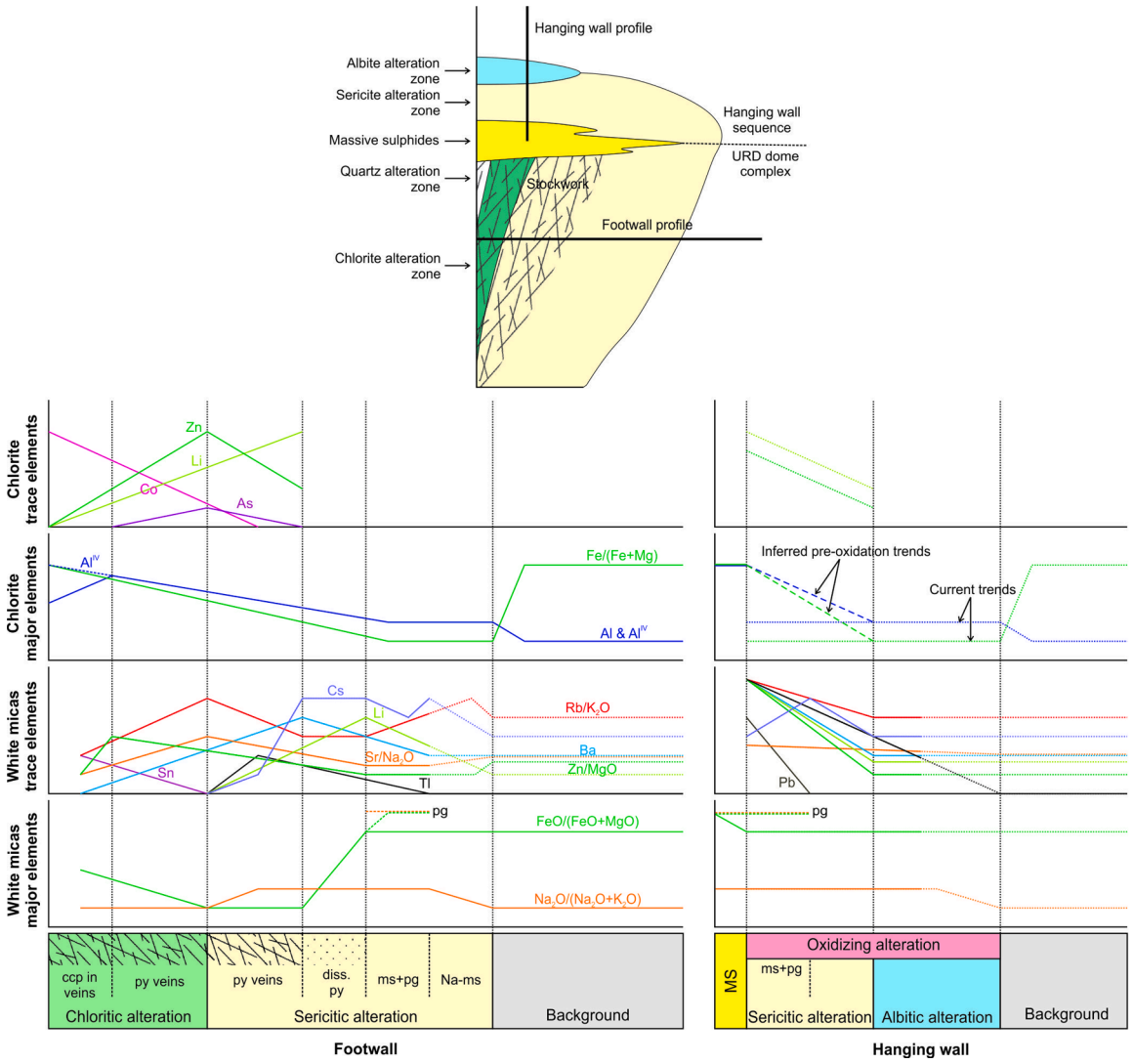

Fig. 19. Schematic summary of the main vectors to ore characterized in this study. Not to scale. Dotted trends are inferred as no data are available. Different partition of Ca, Li and Pb into muscovite and paragonite may produce disruptions of the trends depending on the proportion or both minerals analysed during LA-ICP-MS analysis. ccp: chalcopyrite; dis.: disseminated; MS: massive sulphides; ms: muscovite; pg: paragonite. The oxidizing alteration in the hanging wall was subsequent to the mineralizing event and may have modified the original composition of white micas and chlorite as described in the main text; trends depicted are the currently observable.

- A transition to higher $Na_2O/(Na_2O + K_2O)$ <0.2 at high FeO/(FeO + MgO) as the first (spatially) detectable signature from the hydrothermal system.
- Coexisting paragonite and high $Na_2O/(Na_2O + K_2O)$ muscovite.
- A decrease in FeO/(FeO + MgO) in paragonite (still >0.42) upon destabilization and disappearance of Fe oxides from the mineral assemblage.
- The disappearance of paragonite, and a transition to high $Na_2O/(Na_2O + K_2O)$ (<0.2) low FeO/(FeO + MgO) (<0.42) muscovite around the first appearance of disseminated pyrite.
- A further decrease in FeO/(FeO + MgO) (<0.2) within the sericitic stockwork, with a decrease in $Na_2O/(Na_2O + K_2O)$ (<0.05) in its internal part.
- Within the chloritic stockwork, an increase in FeO/(FeO + MgO) (up to <0.42) towards the centre of the feeder system at low $Na_2O/(Na_2O + K_2O)$ (<0.05).

In the hanging wall, white micas present high FeO/(FeO + MgO) (>0.42), with coexisting high $Na_2O/(Na_2O + K_2O)$ (>0.05) muscovite and paragonite immediately above the massive sulphides, transitioning to high $Na_2O/(Na_2O + K_2O)$ (>0.05) muscovite and finally low $Na_2O/(Na_2O + K_2O)$ (<0.05) muscovite in regional protoliths.

Chlorite presents predominantly clinochlore compositions, with chamosite restricted to the centre of the hydrothermal system. Systematic variations have been observed in Al, Al^{IV}, and Fe/(Fe + Mg) in chlorite. From distal rocks towards the centre of the hydrothermal system in the footwall, chlorite shows:

- A constantly low Al and Al^{IV} at variable Fe/(Fe + Mg) in regional protoliths, the latter being controlled by original whole rock composition and the degree of seafloor metasomatism.
- A decrease in Fe/(Fe + Mg) related to increased seafloor alteration, and a slight increase in Al and Al^{IV} likely due to the thermal influence of hydrothermal fluids. Increased Al and Al^{IV} is the first sign of hydrothermal activity recorded in chlorite.
- Progressively increasing Al^{IV}, Al and Fe/(Fe + Mg) towards the centre of the hydrothermal system.

Discrimination between background and hydrothermally controlled chlorite is important because Fe/(Fe + Mg) in both populations overlap.

Background carbonates consist of calcite, with additional dolomite forming in proximal rocks. Dolomite shows an increase in Fe contents towards the centre of the hydrothermal system, reaching ankeritic compositions.

Systematic variations have been observed in the contents of Ba, Cs, Li, Pb, Rb, Sn, Sr, Tl and Zn in white micas. Barium, Cs, Rb, Tl, V and Zn partition preferentially into muscovite, whereas Li, Pb and Sr partition into paragonite. Rubidium substitutes K, showing equivalent trends across the system, although systematic variations in the Rb/K_2O ratio occur which can be used for vectoring purposes. The same applies to Sr and Na, and Zn and Mg. These ratios present the advantage of not being influenced by analytical mixtures between muscovite and paragonite. High Sn contents occur at the centre of the feeder system, whereas other elements like Cs, Li and Tl present low values at the centre, maximum compositions along a shoulder located at various distances within the hydrothermal system (dependent on the element), but mostly beyond the outer limit of the stockwork, and a final decrease towards background values. This distribution indicates leaching of these elements from the centre of the system and accumulation at its margin. Thalium also presents peak contents around the massive sulphides. Finally, Pb presents high concentrations in the proximal hanging wall. These have been associated with possible destabilization of minor galena in the hanging wall during the oxidizing alteration event and fixation of Pb into white micas.

Trends of trace element contents in chlorite have been less characterized due to analytical limitations. Systematic variations have been observed in the contents of As, Co, Li and Zn. Arsenic, Li and Zn present shoulder distributions peaking in the external chloritic alteration zone within the stockwork for Zn, in medial parts of the stockwork system for As, and outside it for Li. Cobalt presents values above detection limits at the centre of the deep stockwork, with concentrations increasing towards its centre. Higher Sn concentrations have also been detected at the centre of the deep stockwork.

Mineral chemistry vectors to ore have been compared to whole rock geochemistry composition, which has resulted in the recognition of new whole rock geochemistry vectors which had not been detected in Gisbert et al. (2021). These include 1) $Na_2O/(Na_2O + K_2O)$, which is mainly controlled by white micas in proximal rocks; 2) $FeO/(FeO + MgO)$, controlled by both white micas and chlorite, as well as by the presence of other Fe-bearing phases such as Fe oxides and pyrite; and 3) Rb/K_2O. These vectors allow detection of the influence of the hydrothermal system to distances equivalent to mineral chemistry, although they can be strongly influenced by lithological changes.

In footwall rocks, Al content in chlorite is the vector detecting the influence of the hydrothermal system at the greatest distance, at least 120 m along core from the distal stockwork and 316 m away from the nearest massive sulphides. In the hanging wall, the hydrothermal system has been detected at 66 m along core from the massive sulphides in the most distal sample analysed in the area and, therefore, vectors likely reach a larger distance.

In this study, the detailed characterization of vectors to ore associated with mineral chemistry has been facilitated by the originally homogeneous composition of rocks hosting the hydrothermal system. The vectors presented in this work, and the proposed model on their controls, have contributed to our understanding of vectors to ore in replacive VMS deposits in the IPB, potentially improving our exploration capacity in this district. Nevertheless, further characterization of the studied vectors, especially trace elements in white micas and chlorite, is needed at the district scale, as this represents a first contribution constrained to a single deposit, and in other districts inter-deposit variability has been described (e.g. Soltani Dehnavi et al., 2018a; Soltani Dehnavi et al., 2019). Further investigation is also needed on the controls of the composition of precursory phases such as smectite, smectite-illite mixed-layer clays, and illite, as well as the relationship between illite and brammallite. Finally, on a broader scale, our data also adds to the general understanding of vectors to ore in in replacive-type VMS deposits in particular and VMS deposits in general.

Declaration of Competing Interest

The authors declare that they have no known competing financial interests or personal relationships that could have appeared to influence the work reported in this paper.

Acknowledgements

The authors want to thank: MATSA for granting access to Aguas Teñidas deposit drill cores, information supplied, and assistance during core investigation and sampling; technicians in the Laboratorio de Petrología y Geoquímica of the Universidad Complutense de Madrid for assistance in sample processing; Jesús Montes (Universidad de Granada) for thin section preparation; Alfredo Fernández (Centro Nacional de Microscopía Electrónica) and Xavier Llovet (Centres Científics i Tecnològics of the Universitat de Barcelona, CCiT-UB) for assistance in EMP analysis; and an anonymous reviewer for their comments, which have contributed to improve the original manuscript.

Funding

This research has been conducted within the NEXT (New Exploration Technologies) project and has received funding by the European Union's Horizon 2020 research and innovation programme under Grant Agreement No. 776804.

Appendix A. Supplementary data

Supplementary data to this article can be found online at https://doi.org/10.1016/j.oregeorev.2022.104963.

References

Almodóvar, G.R., Sáez, R., Pons, J.M., Maestre, A., Toscano, M., Pascual, E., 1998. Geology and genesis of the Aznalcóllar massive sulphide deposits, Iberian Pyrite Belt. Spain. Miner Depos. 33, 111–136.

Alva-Jimenez, T., Tosdal, R.M., Dilles, J.H., Dipple, G., Kent, A.J.R., Halley, S., 2020. Chemical variations in hydrothermal white mica across the Highland Valley Porphyry Cu-Mo District, British Columbia. Canada. Economic Geology. 115, 903–926.

Alt, J.C., 1999. Very low-grade hydrothermal metamorphism of basic igneous rocks. In: Frey, M., Robinson, D. (Eds.), Low-grade metamorphism. Blackwell Science, Oxford, UK, pp. 169–201.

Ames, D.E., Galley, A.G., Kjarsgaard, I.M., Tardif, N., Taylor, B.T., 2016. Hanging-wall vectoring for buried volcanogenic massive sulfide deposits, Paleoproterozoic Flin Flon mining camp, Manitoba. Canada. Economic Geology. 111, 963–1000.

Baker, M.J., Wilkinson, J.J., Wilkinson, C.C., Cooke, D.R., Ireland, T., 2020. Epidote trace element chemistry as an exploration tool in the Collahuasi District. Northern Chile. Economic Geology. 115, 749–770.

Baldelli, C., Franceschelli, M., Leoni, L., Memmi, I., 1989. Ferrimuscovite and celadonite substitutions in muscovite from Fe3+-rich low-grade psammitic rocks (Northern Apennines, Italy). Lithos. 23, 201–208.

Ballantyne, G.H., 1981. Chemical and mineralogical variations in propylitic zones surrounding porphyry copper deposits. University of Utah, Salt Lake City, Utah.

Barrett, T.J., MacLean, W.H., Årebäck, H., 2005. The Palaeoproterozoic Kristineberg VMS deposit, Skellefte district, northern Sweden. Part II: chemostratigraphy and alteration. Miner Depos. 40, 368–395.

Barriga, F.J.A.S., 1990. Metallogenesis in the Iberian Pyrite Belt. In: Dallmeyer, R.D., Martinez Garcia, E. (Eds.), Pre-Mesozoic Geology of Iberia. Springer-Verlag, Berlin Heidelberg, Berlin, pp. 369–379.

Bayliss, P., 1975. Nomenclature of the trioctahedral chlorites. The Canadian Mineralogist. 13, 178–180.

Bobrowicz, G.L., 1995. Mineralogy, geochemistry and alteration as exploration guides at Aguas Teñidas Este, Pyrite Belt. University of Birmingham, Spain.

Bourdelle, F., Cathelineau, M., 2015. Low-temperature chlorite geothermometry: a graphical representation based on a T-R2+–Si diagram. Eur J Mineral. 27, 617–626.

Bourdelle, F., Parra, T., Chopin, C., Beyssac, O., 2013. A new chlorite geothermometer for diagenetic to low-grade metamorphic conditions. Contrib Mineral Petrol. 165, 723–735.

Carvalho, D., Barriga, F.J.A.S., Munhá, J., 1999. Bimodal siliciclastic systems – The case of the Iberian Pyrite Belt. In: Barrie, C.T., Hannington, M.D. (Eds.), Volcanic-associated massive sulfide deposits: processes and examples in modern and ancient settings. Society of Economic Geologists, pp. 375–408.

Cathelineau, M., 1988. Cation site occupancy in chlorites and illites as a function of temperature. Clay Min. 23, 471–485.
Conde Rivas C. Geology and hydrothermal evolution of massive sulphides of the Iberian Pyrite Belt, Spain: Universidad de Salamanca. 2016.
Conde, C., Tornos, F., 2020. Geochemistry and architecture of the host sequence of the massive sulfides in the northern Iberian Pyrite Belt. Ore Geol Rev. 127, 103042.
Cooke, D.R., Baker, M., Hollings, P., Sweet, G., Chang, Z., Danyushevsky, L., et al., 2014. New advances in detecting the distal geochemical footprints of porphyry systems – Epidote mineral chemistry as a tool for vectoring and fertility assessments. In: Kelley, K.D., Golden, H.C. (Eds.), Building exploration capability for the 21st century: Society of Economic Geologists, Inc, pp. 127–152.
Cooke D, Wilkinson J, Baker M, Agnew P, Martin H, Chang Z, et al. Using mineral chemistry to detect the location of concealed porphyry deposits – an example from Resolution, Arizona. 27th International Applied Geochemistry Symposium 2015. Arizona, USA2015. p. 1-6.
Cooke DR, Agnew P, Hollings P, Baker M, Chang Z, Wilkinson JJ, et al. Porphyry indicator minerals (PIMS) and porphyry vectoring and fertility tools (PVFTS) – Indicators of mineralization styles and recorders of hypogene geochemical dispersion halos. In: Tschirhart V, Thomas MD, editors. Exploration 17: Sixth Decennial International Conference on Mineral Exploration. Toronto, Canada 2017.
Cooke, D.R., Wilkinson, J.J., Baker, M., Agnew, P., Phillips, J., Chang, Z., et al., 2020. Using mineral chemistry to aid exploration: a case atudy from the Resolution Porphyry Cu-Mo Deposit. Arizona. Economic Geology. 115, 813–840.
Costa, I.M.S.R., 1996. Efeitos mineralogicos e geochimicos de alteraço mineralizante en rochas vulcanicas felsicas de Rio Tinto (Faixa Piritosa Iberica. Universidade de Lisboa, Espanha).
Doyle, M.G., Allen, R.L., 2003. Subsea-floor replacement in volcanic-hosted massive sulfide deposits. Ore Geol Rev. 23, 183–222.
Feenstra, A., 1996. An EMP and TEM—AEM Study of Margarite, Muscovite and Paragonite in Polymetamorphic Metabauxites of Naxos Cyclades, Greece) and the Implications of Fine-scale Mica Interlayering and Multiple Mica Generations. J Petrol. 37, 201–233.
Franklin, J.M., Kasarda, J., Poulsen, K.H., 1975. Petrology and chemistry of the alteration zone of the Mattabi massive sulfide deposit. Economic Geology. 70, 63–79.
Franklin, J.M., Gibson, H.L., Jonasson, I.R., Galley, A.G., Hedenquist, J.W., Thompson, J. F.H., et al., 2005. Volcanogenic massive sulfide deposits. 100th Anniversary Volume: Society of Economic Geologists 525–560.
Frey, M., 1978. Progressive low-grade metamorphism of a black shale formation, central Swiss Alps, with special reference to pyrophyllite and margarite bearing assemblages. J Petrol. 19, 95–135.
Gaillard, N., Williams-Jones, A.E., Clark, J.R., Lypaczewski, P., Salvi, S., Perrouty, S., et al., 2018. Mica composition as a vector to gold mineralization: Deciphering hydrothermal and metamorphic effects in the Malartic district. Quebec. Ore Geol Rev. 95, 789–820.
Gemmell, J.B., Fulton, R., 2001. Geology, genesis, and exploration implications of the footwall and hanging-wall alteration associated with the Hellyer Volcanic-Hosted massive sulfide deposit, Tasmania. Australia. Economic Geology. 96, 1003–1035.
Genna, D., Gaboury, D., 2015. Deciphering the hydrothermal evolution of a VMS system by LA-ICP-MS using trace elements in pyrite: an example from the Bracemac-McLeod deposits, Abitibi, Canada, and implications for exploration. Economic Geology. 110, 2087–2108.
Gibson, H.L., Allen, R.L., Riverin, G., Lane, T.E., 2007. The VMS model: advances and application to exploration targeting. In: Milkereit, B. (Ed.), Proceedings of Exploration 07: Fifth Decennial International Conference on Mineral Exploration, pp. 713–730.
Giorgetti, G., Monecke, T., Kleeberg, R., Hannington, M.D., 2006. Low-Temperature Hydrothermal Alteration of Silicic Glass at the PACMANUS Hydrothermal Vent Field, Manus Basin: An XRD, SEM and AEM-TEM study. Clay Clay Min. 54, 240–251.
Gisbert, G., Tornos, F., Losantos, E., Pons, J.M., Videira, J.C., 2021. Vectors to ore in replacive volcanogenic massive sulfide (VMS) deposits of the northern Iberian Pyrite Belt: mineral zoning, whole rock geochemistry, and application of portable X-ray fluorescence. Solid Earth. 12, 1931–1966.
Grant, H.L.J., Hannington, M.D., Petersen, S., Frische, M., Fuchs, S.H., 2018. Constraints on the behavior of trace elements in the actively-forming TAG deposit, Mid-Atlantic Ridge, based on LA-ICP-MS analyses of pyrite. Chem Geol. 498, 45–71.
Guidotti C. Micas in metamorphic rocks. In: Bailey SW, editor. Micas 1984. p. 357-467.
Guidotti, C.V., Sassi, F.P., 1998. Petrogenetic significance of Na-K white mica mineralogy: Recent advances for metamorphic rocks. Eur J Mineral. 10, 815–854.
Guidotti CV, Sassi FP. 9. Constraints on studies of metamorphic K-Na white micas. In: Annibale M, Francesco Paolo S, James BT, Stephen G, editors. Micas: Crystal Chemistry & Metamorphic Petrology. Berlin, Boston: De Gruyter; 2002. p. 413-448.
Guidotti, C.V., Sassi, F.P., Blencoe, J.G., Selverstone, J., 1994a. The paragonite-muscovite solvus: I. P-T-X limits derived from the Na-K compositions of natural, quasibinary paragonite-muscovite pairs. Geochim Cosmochim Acta. 58, 2269–2275.
Guidotti, C.V., Yates, M.G., Dyar, M.D., Taylor, M.E., 1994b. Petrogenetic implications of the Fe3+ content of muscovite in pelitic schists. Am Miner. 79, 793–795.
Hannington, M.D., 2014. 13.18 – Volcanogenic massive sulfide deposits. In: Holland, H. D., Turekian, K.K. (Eds.), Treatise on Geochemistry (Second Edition). Elsevier, Oxford, pp. 463–488.
Herrmann, W., Blake, M., Doyle, M., Huston, D., Kamprad, J., Merry, N., et al., 2001. Short Wavelength Infrared (SWIR) spectral analysis of hydrothermal alteration zones associated with base metal sulfide deposits at Rosebery and Western Tharsis, Tasmania, and Highway-Reward. Queensland. Economic Geology. 96, 939–955.
Hidalgo, R., Guerrero, V., Pons, J.M., Anderson, I.K., 2000. The Aguas Teñidas Este mine. Huelva Province, SW Spain.
IGME. Síntesis Geológica de la Faja Pirítica del SO de España. Madrid: Instituto Geológico y Minero de España. 1982.
Inoue, A., Kohyama, N., Kitagawa, R., Watanabe, T., 1987. Chemical and morphological evidence for the conversion of smectite to illite. Clay Clay Min. 35, 111–120.
Inoue, A., Meunier, A., Patrier-Mas, P., Rigault, C., Beaufort, D., Vieillard, P., 2009. Application of chemical geothermometry to low-temperature trioctahedral chlorites. Clay Clay Min. 57, 371–382.
Keller, L.M., De Capitani, C., Abart, R., 2005. A quaternary solution model for white micas based on natural coexisting phengite–paragonite pairs. J Petrol. 46, 2129–2144.
Lackschewitz, K.S., Devey, C.W., Stoffers, P., Botz, R., Eisenhauer, A., Kummetz, M., et al., 2004. Mineralogical, geochemical and isotopic characteristics of hydrothermal alteration processes in the active, submarine, felsic-hosted PACMANUS field, Manus Basin. Papua New Guinea. Geochim Cosmochim Acta. 68, 4405–4427.
Lanari, P., Wagner, T., Vidal, O., 2014. A thermodynamic model for di-trioctahedral chlorite from experimental and natural data in the system MgO–FeO–Al2O3–SiO2–H2O: applications to P-T sections and geothermometry. Contrib Mineral Petrol. 167, 968.
Large, R.R., McPhie, J., Gemmell, B., Herrmann, W., Davidson, G.J., 2001a. The spectrum of ore deposit types, volcanic environments, alteration halos, and related exploration vectors in submarine volcanic successions: some examples from Australia. Economic Geology. 96, 913–938.
Large, R.R., Allen, R.L., Blake, M.D., Herrmann, W., 2001b. Hydrothermal Alteration and Volatile Element Halos for the Rosebery K Lens Volcanic-Hosted Massive Sulfide Deposit. Western Tasmania. Economic Geology. 96, 1055–1072.
Large, R.R., Gemmell, J.B., Paulick, H., Huston, D.L., 2001c. The alteration box plot: a simple approach to understanding the relationship between alteration mineralogy and lithogeochemistry associated with volcanic-hosted massive sulfide deposits. Economic Geology. 96, 957–971.
Large, R.R., Halpin, J.A., Danyushevsky, L.V., Maslennikov, V.V., Bull, S.W., Long, J.A., et al., 2014. Trace element content of sedimentary pyrite as a new proxy for deep-time ocean–atmosphere evolution. Earth Planet Sci Lett. 389, 209–220.
Laznicka, P., 1999. Quantitative relationships among giant deposits of metals. Economic Geology. 94, 455–473.
Leistel JM, Bonijoly D, Braux C, Freyssenet P, Kosakevitch A, Leca X, et al. The massive sulphide deposits of the South Iberian Pyrite Province: geological setting and exploration criteria. In: Leistel JM, Leca X, editors. Substances Minérales et Énergiques Documents du BRGM 234: Ed. BRGM; 1994.
Leistel, J.M., Marcoux, E., Thieblemont, D., Quesada, C., Sanchez, A., Almodovar, G.R., et al., 1998. The volcanic-hosted massive sulphide deposits of the Iberian Pyrite Belt – Review and preface to the Thematic Issue. Miner Depos. 33, 2–30.
Lentz, D.R., Hall, D.C., Hoy, L.D., 1997. Chemostratigraphic, alteration, and oxygen isotopic trends in a profile through the stratigraphic sequence hosting the Health Steele B zone massive sulfide deposit. New Brunswick. The Canadian Mineralogist. 35, 841–874.
Li, G., Peacor, D.R., Merriman, R.J., Roberts, B., 1994. The diagenetic to low-grade metamorphic evolution of matrix white micas in the system muscovite-paragonite in a mudrock from central Wales. United Kingdom. Clay Clay Min. 42, 369–381.
Livi, K.J.T., Veblen, D.R., Ferry, J.M., Frey, M., 1997. Evolution of 2:1 layered silicates in low-grade metamorphosed Liassic shales of Central Switzerland. Journal of Metamorphic Geology. 15, 323–344.
Livi, K.J.T., Christidis, G.E., Pt, Á., Veblen, D.R., 2008. White mica domain formation: A model for paragonite, margarite, and muscovite formation during prograde metamorphism. Am Miner. 93, 520–527.
Luz, F., Mateus, A., Figueiras, J., Tassinari, C.C.G., Ferreira, E., Gonçalves, L., 2019. Recognizing metasedimentary sequences potentially hosting concealed massive sulfide accumulations in the Iberian Pyrite Belt using geochemical fingerprints. Ore Geol Rev. 107, 973–998.
Lydon, J.W., 1988. Ore Deposit Models #14. Volcanogenic Massive Sulphide Deposits Part 2: Genetic Models. Geoscience Canada. 15.
Madeisky, H.E., Stanley, C.R., 1993. Lithogeochemical exploration of metasomatic zones associated with volcanic-hosted massive sulfide deposits using Pearce element ratio analysis. Int Geol Rev. 35, 1121–1148.
Mantero, E.M., Alonso-Chaves, F.M., García-Navarro, E., Azor, A., 2011. Tectonic style and structural analysis of the Puebla de Guzmán Antiform (Iberian Pyrite Belt, South Portuguese Zone, SW Spain). Geological Society, London, Special Publications. 349, 203–222.
Martin-Izard, A., Arias, D., Arias, M., Gumiel, P., Sanderson, D.J., Castañon, C., et al., 2016. Ore deposit types and tectonic evolution of the Iberian Pyrite Belt: From transtensional basins and magmatism to transpression and inversion tectonics. Ore Geol Rev. 79, 254–267.
Maydagán, L., Franchini, M., Impiccini, A., Lentz, D., Patrier, P., Beaufort, D., 2018. Chlorite, white mica and clay minerals as proximity indicators to ore in the shallow porphyry environment of Quebrada de la Mina deposit. Argentina. Ore Geol Rev. 92, 297–317.
McKee, G.S., 2003. Genesis and deformation of the Aguas Teñidas Este massive sulphide deposit and implications for the formation, structural evolution and exploration of the Iberian Pyrite. University of Birmingham, Belt.
McKee, G.S., Hidalgo, R., Ixer, R.A., Boyce, A., Guerrero, V., Pons, J.M., 2001. Deposit formation and structural evolution at Aguas Teñidas Este. In: Tornos, F., Pascual, E., Sáez, R., Hidalgo, R. (Eds.), GEODE Workshop: Massive sulphide deposits in the Iberian Pyrite Belt: New advances and comparison with equivalent systems, pp. 38–89.
Mukherjee, I., Large, R., 2017. Application of pyrite trace element chemistry to exploration for SEDEX style Zn-Pb deposits: McArthur Basin, Northern Territory. Australia. Ore Geol Rev. 81, 1249–1270.

Munhá, J., 1983. Hercynian magmatism in the Iberian Pyrite Belt. Memórias dos Serviços Geológicos de Portugal. 29, 39–81.
Munhá, J., Kerrich, R., 1980. Sea water basalt interaction in spilites from the Iberian Pyrite Belt. Contrib Mineral Petrol. 73, 191–200.
Nieto, F., Ortega-Huertas, M., Peacor, D.R., Arostegui, J., 1996. Evolution of Illite/Smectite from Early Diagenesis Through Incipient Metamorphism in Sediments of the Basque-Cantabrian Basin. Clay Clay Min. 44, 304–323.
Oliveira JT. South Portuguese Zone: introduction. Stratigraphy and synsedimentary tectonism. In: Dallmeyer RD, Martínez García E, editors. PreMesozoic Geology of Iberia: Springer Verlag; 1990. p. 333-47.
Onuk, P., Melcher, F., Mertz-Kraus, R., Gäbler, H.-E., Goldmann, S., 2017. Development of a matrix-matched aphalerite reference material (MUL-ZnS-1) for calibration of in situ trace element measurements by laser ablation-inductively coupled plasma-mass spectrometry. Geostandards and Geoanalytical Research. 41, 263–272.
Post, J.E., Burnham, C.W., 1986. Ionic modeling of mineral structures and energies in the electron gas approximation; TiO2 polymorphs, quartz, forsterite, diopside. Am Miner. 71, 142–150.
Relvas, J.R.M.S., Massano, C.M.R., Barriga, F.J.A.S., 1990. Ore zone hydrothermal alteration around the Gaviäo orebodies: implications for exploration in the Iberian Pyrite Belt. VIII Semana de Geoquimica. Lisboa 3.
Relvas, J.M.R.S., Barriga, F.J.A.S., Ferreira, A., Noiva, P.C., Pacheco, N., Ga, B., 2006. Hydrothermal alteration and mineralization in the Neves-Corvo volcanic-hosted massive sulfide deposit, Portugal. I. Geology, mineralogy, and geochemistry. Economic Geology. 101, 753–790.
Rieder, M., Cavazzini, G., D'Yakonov, Y.S., Frank-Kamenetskii, V.A., Gottardi, G., Guggenheim, S., et al., 1998. Nomenclature of the micas. Can Mineral. 36, 905–912.
Saccocia, P.J., Seyfried, W.E., 1994. The solubility of chlorite solid solutions in 3.2 wt% NaCl fluids from 300–400°C, 500 bars. Geochim Cosmochim Acta. 58, 567–585.
Sáez, R., Moreno, C., González, F., Almodóvar, G.R., 2011. Black shales and massive sulfide deposits: causal or casual relationships? Insights from Rammelsberg, Tharsis, and Draa Sfar. Miner Depos. 46, 585–614.
Sánchez-España, J., Velasco, F., Yusta, I., 2000. Hydrothermal alteration of felsic volcanic rocks associated with massive sulphide deposition in the northern Iberian Pyrite Belt (SW Spain). Appl Geochem. 15, 1265–1290.
Sánchez-España, J., Velasco, F., Boyce, A.J., Fallick, A.E., 2003. Source and evolution of ore-forming hydrothermal fluids in the northern Iberian Pyrite Belt massive sulphide deposits (SW Spain): evidence from fluid inclusions and stable isotopes. Miner Depos. 38, 519–537.
Schardt, C., Cooke, D.R., Gemmell, J.B., Large, R.R., 2001. Geochemical modeling of the zoned footwall alteration pipe, Hellyer volcanic-hosted massive sulfide deposit, Western Tasmania. Australia. Economic Geology. 96, 1037–1054.
Schermerhorn, L.J.G., 1971. An outline stratigraphy of the Iberian Pyrite Belt. Boletín Geológico y Minero. 82, 23–52.
Silva, J.B., Oliveira, J.T., Ribeiro, A., 1990. Structural outline. In: Dallmeyer, R.D., Garcia, E.M. (Eds.), Pre-Mesozoic Geology of Iberia. Berlin, Heidelberg, Springer, Berlin Heidelberg, pp. 348–362.
Simancas, J.F., 2004. Zona Sudportuguesa. In: Vera, J.A. (Ed.), Geología de España. SGE-IGME, Madrid, pp. 199–222.
Soltani Dehnavi, A., Lentz, D.R., McFarlane, C.R.M., Walker, J.A., 2018a. Quantification of fluid-mobile elements in white mica by LA-ICP-MS: From chemical composition to a potential micro-chemical vectoring tool in VMS exploration. J Geochem Explor. 188, 290–307.
Soltani Dehnavi, A., McFarlane, C.R.M., Lentz, D.R., Walker, J.A., 2018b. Assessment of pyrite composition by LA-ICP-MS techniques from massive sulfide deposits of the Bathurst Mining Camp, Canada: From textural and chemical evolution to its application as a vectoring tool for the exploration of VMS deposits. Ore Geol Rev. 92, 656–671.
Soltani Dehnavi, A., McFarlane, C.R.M., Lentz, D.R., McClenaghan, S.H., Walker, J.A., 2019. Chlorite-white mica pairs' composition as a micro-chemical guide to fingerprint massive sulfide deposits of the Bathurst Mining Camp. Canada. Minerals. 9, 125.
Strauss, G.K., Roger, G., Lecolle, M., Lopera, E., 1981. Geochemical and geologic study of the volcano-sedimentary sulfide orebody of La Zarza, Province of Huelva. Spain. Economic Geology. 76, 1975–2000.
Tornos, F., 2006. Environment of formation and styles of volcanogenic massive sulfides: The Iberian Pyrite Belt. Ore Geol Rev. 28, 259–307.
Tornos, F., González Clavijo, E., Spiro, B., 1998. The Filon Norte orebody (Tharsis, Iberian Pyrite Belt): a proximal low-temperature shale-hosted massive sulphide in a thin-skinned tectonic belt. Miner Depos. 33, 150–169.
Tornos, F., Solomon, M., Conde, C., Spiro, B.F., 2008. Formation of the Tharsis massive sulfide deposit, Iberian Pyrite Belt: Geological, lithogeochemical, and stable isotope evidence for deposition in a brine pool. Economic Geology. 103, 185–214.
Tornos, F., Peter, J.M., Allen, R., Conde, C., 2015. Controls on the siting and style of volcanogenic massive sulphide deposits. Ore Geol Rev. 68, 142–163.
Toscano M, Almodóvar GR, Pascual E, Sáez R. Hydrothermal alteration related to the "Masa Valverde" massive sulphide deposit, Iberian Pyrite Belt, Spain. In: Fenoll Hach-Alí PF, Torres-Ruiz J, Gervilla F, editors. Current research in geology applied to ore deposits Proceedings of the 2nd biennal SGA meeting, Granada, 9-11 September 19931993. p. 389-92.
Toscano, M., Mesa, J.M., Ruiz de Almodóvar, G., 1994a. Datos de DRX de la aureola de alteración hidrotermal asociada a "Masa Valverde". Boletín de la Sociedad Española de Mineralogía. 17, 159–160.
Toscano, M., Ruiz de Almodóvar, G., Sáez, R., 1994b. Variación composicional de las sericitas de alteración hidrotermal en sulfuros masivos: "Masa Valverde" (Huelva). Boletín de la Sociedad Española de Mineralogía. 17, 161–162.
Trincal, V., Lanari, P., 2016. Al-free di-trioctahedral substitution in chlorite and a ferri-sudoite end-member. Clay Min. 51, 675–689.
Ulrich, T., Kamber, B.S., Jugo, P.J., Tinkham, D.K., 2009. Imaging element-distribution patterns in minerals by laser ablation – inductively coupled plasma – mass spectrometry (LA – ICP – MS). The Canadian Mineralogist. 47, 1001–1012.
Ulrich, T., Long, D.G.F., Kamber, B.S., Whitehouse, M.J., 2011. In situ trace element and sulfur isotope analysis of pyrite in a Paleoproterozoic gold placer deposit, Pardo and Clement townships, Ontario. Canada. Economic Geology. 106, 667–686.
Urabe, T., Scott, S.D., Hattori, K., Ohmoto, H., Skinner, B.J., 1983. A comparison of footwall-rock alteration and geothermal systems beneath some Japanese and Canadian volcanogenic massive sulfide deposits. Society of Economic Geologists, The Kuroko and Related Volcanogenic Massive Sulfide Deposits, pp. 345–364.
Uribe-Mogollon, C., Maher, K., 2018. White mica geochemistry of the Copper Cliff porphyry Cu deposit: insights from a vectoring tool applied to exploration. Economic Geology. 113, 1269–1295.
Velasco-Acebes, J., Tornos, F., Kidane, A.T., Wiedenbeck, M., Velasco, F., Delgado, A., 2019. Isotope geochemistry tracks the maturation of submarine massive sulfide mounds (Iberian Pyrite Belt). Miner Depos. 54, 913–934.
Vidal, O., Lanari, P., Munoz, M., Bourdelle, F., De Andrade, V., 2016. Deciphering temperature, pressure and oxygen-activity conditions of chlorite formation. Clay Min. 51, 615–633.
Walshe, J.L., 1986. A six-component chlorite solid solution model and the conditions of chlorite formation in hydrothermal and geothermal systems. Economic Geology. 81, 681–703.
Walshe, J.L., Solomon, M., 1981. An investigation into the environment of formation of the volcanic-hosted Mt. Lyell copper deposits using geology, mineralogy, stable isotopes, and a six-component chlorite solid solution model. Economic Geology. 76, 246–284.
Wang, R., Cudahy, T., Laukamp, C., Walshe, J.L., Bath, A., Mei, Y., et al., 2017. White mica as a hyperspectral tool in exploration for the Sunrise Dam and Kanowna Belle Gold Deposits. Western Australia. Economic Geology. 112, 1153–1176.
Wiewióra, A., Weiss, Z., 1990. Crystallochemical classifications of phyllosilicates based on the unified system of projection of chemical composition: II. The chlorite group. Clay Min. 25, 83–92.
Wilkinson, J.J., Chang, Z., Cooke, D.R., Baker, M.J., Wilkinson, C.C., Inglis, S., et al., 2015. The chlorite proximitor: A new tool for detecting porphyry ore deposits. J Geochem Explor. 152, 10–26.
Wilkinson, J.J., Baker, M.J., Cooke, D.R., Wilkinson, C.C., 2020. Exploration targeting in porphyry Cu systems using propylitic mineral chemistry: a case study of the El Teniente deposit. Chile. Economic Geology. 115, 771–791.
Wilson, S.A., Ridley, W.I., Koenig, A.E., 2002. Development of sulfide calibration standards for the laser ablation inductively-coupled plasma mass spectrometry technique. Journal of Analytical Atomic Spectrometry. 17, 406–409.
Woodhead, J.D., Hellstrom, J., Hergt, J.M., Greig, A., Maas, R., 2007. Isotopic and elemental imaging of geological materials by laser ablation inductively coupled plasma-mass spectrometry. Geostandards and Geoanalytical Research. 31, 331–343.
Xiao, B., Chen, H., Wang, Y., Han, J., Xu, C., Yang, J., 2018. Chlorite and epidote chemistry of the Yandong Cu deposit, NW China: Metallogenic and exploration implications for Paleozoic porphyry Cu systems in the Eastern Tianshan. Ore Geol Rev. 100, 168–182.
Yavuz, F., Kumral, M., Karakaya, N., Karakaya, M.Ç., Yıldırım, D.K., 2015. A Windows program for chlorite calculation and classification. Comput Geosci. 81, 101–113.